Anchoring FRP Composite Armor in Flexible Offshore Riser Systems

PhD Thesis

$$(EIv'')'' = q - \rho A \ddot{v}$$
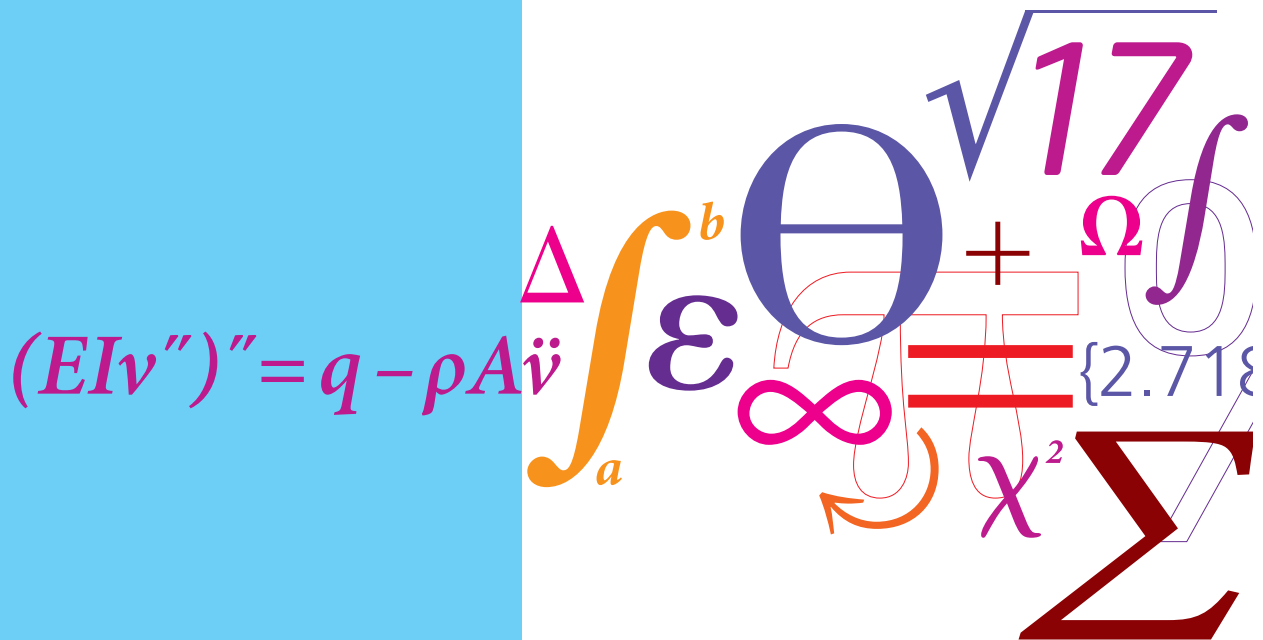
Andrei Costache
DCAMM Special Report No. S194
October 2015

DTU Mechanical Engineering
Department of Mechanical Engineering

Anchoring FRP Composite Armor in Flexible Offshore Riser Systems

Andrei Costache

Preface

This thesis is submitted in partial fulfillment the requirements for obtaining a Ph.D in mechanical engineering at the Technical University of Denmark. The Ph.D project was carried out at the Department of Mechanical Engineering, section of Solid Mechanics, starting the 15th of July 2012 until the 15th of October 2015. The project supervisors are: Associate Professor Christian Berggreen from the section of Solid Mechanics, Lead Engineer Kristian Glejbøl from National Oilwell Varco, Subsea Production Systems I/S, and Associate Professor Ion Marius Sivebæk from the section of Manufacturing Engineering.

The project is part of the Industrial Ph.D program in Denmark. Through this, the Ph.D candidate is employed by a private company, while at the same time being enrolled at the university. This project represents the collaboration between the Technical University of Denmark, and National Oilwell Varco (NOV), Subsea Production Systems I/S. The project is part of the greater effort undertaken by NOV to create the next generation of composite flexible risers.

I would like to thank Ion Marius Sivebæk for his help and supervision during the harder parts of the project, to Kristian Glejbøl for his guidance and thrust, and to Christian Berggreen for offering me this great opportunity. I acknowledge the financial support of the Danish Agency for Science, Technology and Innovation, grant number 0604-00909. A special thanks goes to my colleagues and fellow Ph.D students at the Department of Mechanical Engineering, Section for Solid Mechanics, Lightweight Structures Group, for their help, support and friendship.

Thanks to my family and friends for their support. With love to Dana and Angela, the most important persons in my life.

Thursday 15$^{\text{th}}$ October, 2015

Andrei Costache

Abstract

Anchoring FRP Composite Armor in Flexible Offshore Riser Systems

Unbonded flexible pipes find extensive use in the offshore oil industry. Although more expensive than rigid pipe, the total cost of flexible pipe installations are often less. This is because flexible pipes are easier to store and deploy, coupled with superior fatigue performance. Among other things, they serve for the transportation of hydrocarbons from the subsea facilities to the production and drilling equipment at the sea surface. Flexible risers are the prime choice for connecting floating production, storage and offloading facilities, because they are specially designed for dynamic capabilities.

The structure of flexible pipes consists of several concentric layers, each with a specific purpose. The most common used flexible pipe is the type III, which contains a central component, made from an interlocking stainless steel structure that provides collapse strength. The central component is called the carcass. A permeation polymer barrier is extruded over the carcass, followed by the pressure armor. On top, two counter-wound helical layers form the tensile armor. These carry forces in axial direction, and constitute the main focus of this thesis. In conventional flexible pipes, the tensile armor layer is made from steel. However, as oil exploitation goes to deeper and deeper waters, the strength/weight ratio of steel armor becomes unfavorable. In order to achieve higher tensile strength and to reduce the overall weight of the pipe, in the future, the tensile armor must be made of composite materials. One of the problems related to the substitution of tensile steel members is that anchoring in the metallic end fittings of the pipe is very challenging.

The purpose of this thesis is to ensure the transfer of tensile loads between a unidirectional fiber reinforced polymer and a metallic counterpart. A new double grip design with flat faces is proposed, in which the loads are transferred through friction. The behavior of such grip is studied by means of experimental testing and

finite element modeling.

Several iterations of the grip system were evaluated over the course of the project. Initial effort did concentrate on creating an experimental setup which allows to control and record force and displacement values with great accuracy. Pullout tests using several sets of materials and grips, with different geometries and surface roughness were executed.

Besides the experimental work, a finite element model was constructed for each of the experimental configurations. Initial effort is used to understand the behavior of the grip and obtain good accuracy with the finite element model. Experimental data is used as input. The model makes it possible to visualize the piece-wise onset of movement in the grip, and to measure the contact stresses distribution and evolution during pullout.

The results of the experimental and numerical analysis show that it is possible to reliably anchor composite materials using a metallic grip. The models developed during the project show how to improve the efficiency of the grip system. Analysis of the boundary conditions show that several technical solutions can be chosen, without sacrificing performance. It is possible to create grips to fit a wide variety of constructive solutions.

Resumé

Metode til Forankring af Fiberforstærket Kompositarmering til Brug i Fleksible Offshore Rørsystemer

Fleksible rør finder udbredt anvendelse i offhore olieindustrien. På trods af at fleksible rør er dyrere end stive rør er de totale driftsomkostninger ofte lavere, dels fordi de er nemmere at installere og dels fordi de har langt bedre udmattelsesegenskaber. Blandt mange anvendelser, er en af de vigtigste for at transportere udvundne hydrokarboner fra udvindingsstedet på havbunden og op til produktionsfaciliteterne på havoverfladen.

Fleksible rør er opbygget af adskillige concentriske lag, hvor hvert lag har hvert sit specifikke formål. Den mest udbredte rørtype er såkaldte type II rør. Fra centrum og udefter er et type III rør opbygget omkring en såkaldt carcass der er viklet stålstruktur der har til formål at modstå ydre trykpåvirkninger. Udenpå denne struktur ligger et trykbærende polymerlag, den såkaldte liner. For at understøtte det indre tryk ligger der udenpå lineren en trykarmering, Det yderste armeringslag er trækarmeringen der består at to modsat viklede lag af langsgående armering. Fastholdelse af denne langsgående armering er hovedfokus for dette arbejde.

I konventionelle fleksible rør er den langsgående trækarmering lavet af stål. I takt med at olieudvinding forgår på større og større dybder gør ståls høje vægt at kompositmaterialer bliver et interessant alternativ som armering. Et af de største problemer forbundet med anvendelsen af kompositmaterialer i stedet for stål er forankringen af disse materialerer er meget udfordrende.

Formålet med denne afhandling er anvise en metode til overførsel af trækspændinger imellem en unidirektional fiberkomposit og en metallisk modpart. Et nyt dobbeltkæbe design med flade anlægsflader, hvor kræfterne er overført via friktion bliver undersøgt i dette arbejde. Undersøgelsen omfatter såvel praktisk arbejde som finite element simuleringer.

Adskillige udførsler af kæbesystemet er blevet studeret igennem projektforløbet.

Det indledende arbejde fokuserede især på at lave en eksperimentel opstilling der tillader samtidig præcis kontrol og dataopsamling af både kræfter og forskydninger. Udtrækningstests med adskillige forskellige kæber, materialer og overfladeruheder blev udført igennem projektforløbet.

Både numeriske og eksperimentelle resultater bekræfter, at det er muligt at opnå en pålidelig forankring af UD komposit materialer i en metallisk modpart ved hjælp af mekanisk låsning. Undersøgelser af grænsebetingelser viser, at forskellige tekniske løsninger kan vælges uden at gå på kompromis med den med den tekniske ydelse. Det er derfor muligt at anvende kæber med varierende udformninger.

List of Publications

Journal Articles

(A) A. Costache, K. Glejbøl, I. M. Sivebæk, and C. Berggreen. "Friction Joint Between Basalt-Reinforced Composite and Aluminum". *Tribology Letters*, 2015.

(B) A. Costache, K. Glejbøl, I. M. Sivebæk, and C. Berggreen. "Numerical Investigation of Friction Joint between Basalt Reinforced Composite and Aluminum". *Submitted to Proceedings of the IMechE, Part J: Journal of Engineering Tribology*, 2015.

(C) A. Costache, K. Glejbøl, I. M. Sivebæk, and C. Berggreen. "Stress Analysis of a Friction Joint between Basalt Reinforced Composite and Aluminum". *To be submitted*, 2015.

(D) A. Costache, K. Glejbøl, I. M. Sivebæk, and C. Berggreen. "Improved friction joint with v-shaped grips". *Submitted to International Journal of Mechanical Sciences*, 2015.

Conference Poster Presentations

(E) A. Costache, K. Anyfantis, and C. Berggreen. *On the Analysis of a Contact Friction Composite-to-Metal Joint*. , 2013.

(F) A. Costache, K. Glejbøl, I. M. Sivebæk, and C. Berggreen. *Experimental Investigation of a Basalt Fiber reinforced Composite to Metal Joint*. , 2015.

Table of Contents

Chapter 1

Introduction

1.1   Market Research

According to the Houston's Offshore Technology Conference, fossil fuels will remain the dominant energy supply for the next two decades [7]. Due to the depletion of in use resources, the oil production capacity has to increase with at least 55 million barrels per day (bpd) by 2030. The worldwide consumption of liquid fuels is estimated to increase to 97 million bpd in 2020, and to reach 115 million bpd in 2040 [8]. 80% of the demand increase will be from non-OECD economies. The price in dollars per bbl is estimated to increase by 2040 to between 75 and 237, with some models stabilizing at a price of 130 [9]. The most significant increase in production will come from non-OPEC countries, with main contributions from Brazil, Canada, the United States and Kazakhstan.

In keeping up with this future demand, there is a real need to expand and diversify current resources. One of the most significant unexplored offshore reserves has recently being found off the coast of Brasil [10], in what is now called the 'pre-salt' deposits. These deposits hold an estimated 80 billion barrel of oil (bbl) and natural gas, which would allow Brasil to further increase its production. The deepwater Santos, Campos and Espírito Santo basins, which are operated by the national owned company Pertrobras, have already increased Basil's pre-salt production from 2% to 18% in 2015 [11].

According to the EMA report of 2013 [12], the current backlog consists of 72 production floaters. Brasil dominates the orders, with 23 units, which represent 32% of the total orders. There are 53 potential floater projects currently in the planning cycle, some of them including multiple floating production storage and offloading (FPSO) platforms. In terms of water depth, Brasil is also the main location

for ultra-deepwater projects, with most projects in water depths exceeding 1500 m. Out of the future projects which involve floating production or storage systems, 27 are in water depth exceeding 1500 m, 7 between 1000 and 1500 m, and 19 in less than 1000 m. The shear number of upcoming projects grantees a steady need for the production of flexible pipes.

There are many challenges which have to be addressed, due to the technically challenging environment of the reservoirs. According to the head of exploration and production of Petrobras, the oil-bearing rock of the pre-salt reservoirs is positioned under a thick layer of salt [13]. The Santos Basin is located 300 to 350 km away from the coast. Th reservoir depth is between 5000 and 6000 m below the sea level, under a thick layer of salt, sometimes in excess of 2000 m. The challenging aspect of pipe design is represented by the ultra deepwater, ranging from 1900 to 2400 m. Several systems can be applied for the transport of hydrocarbons, or water and gas injection.

Unbonded flexible pipes are one of the solutions under consideration, mainly because the technology was used and qualified for the pre-salt pilot project development [14]. For water depths in excess of 1500 m the free catenary solution is not always applicable. The presence of contaminants, such as CO_2 and H_2S, require the use of sour service armor wires, which have inferior material properties when compared to high strength steels. Furthermore, it is also difficult to use large diameter pipes, especially for gas export, due to the high water pressure [15].

1.2   Unbonded Flexible Pipes

Unbonded flexible pipes are used to connect between the underwater oil well to the production and storage facilities located at the sea surface. They can serve for both extraction and injection, and can also connect between underwater or above water structures. Lately, unbondend flexible pipes have become the go-to solution for the offshore oil industry due to the many advantages they posses when compared to steel catenary pipes. The advantages include that they do not have to be assembled from sections, which have custom lengths, and can be installed very fast. Even more important, it is their flexibility, which makes them better suited for applications where there is a significant amount of movement. This relative movement is caused by wave cycles, and is present in the case of semi-submersible platforms and FPSOs.

Decoupling the movement of the sea-surface part of the riser from the rest of the structure can be achieved by adding flotation devices, as shown in Fig. 1.1, where the riser is deployed in a steep-s configuration. It uses two fully submerged buoys toward the ship, as well as distributed buoyancy modules installed directly on the
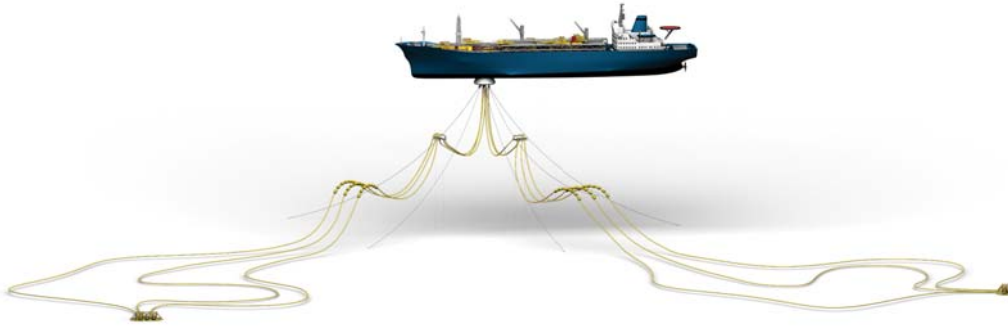
Figure 1.1: FPSO and flexible pipe connection.

pipe toward the sea bottom. This arrangement greatly reduces the dynamic loads experienced by the pipe and thus improves the lifetime of the system. It also makes possible to use dedicated pipe sections, which are assembled together. The top section is mainly subjected to cyclic tensile loads, and the bottom section experiences high compressive loads. Unfortunately, adding buoyancy is very expensive and has to be avoided if possible.

The cheapest solution is a free hanging catenary, which goes directly from the platform to the sea floor. It is very hard to make a free hanging catenary for ultra-deepwater using todays generation of unbonded flexible pipes. This is mainly because of their weight, which is the limiting factor. When subjected to dynamic loads, they will break under their own weight. Because of this, the industry is looking into increasing the tensile strength of the pipes, while at the same time making them lighter.

The standard flexible pipe In Fig. 1.2 consists of several concentric layers, which have a specific purpose to fulfill. The specifications for each layer are standardized, and can be found in the American Petroleum Institute - API Specification 17J [16].

The aspect of the layers can differ from pipe to pipe, and from producer to producer. Some extra layers can be added, according to the purpose of the pipe. An outer sheath is used to provide external fluid integrity, and several insulation layers can be used inside the pipe. But the basic configuration is the same in all cases:

1. Carcass: An interlocking metallic layer which provides collapse resistance.

2. Inner Liner: An extruded polymer layer which provides internal fluid integrity.

3. Pressure Armor: An interlocking layer which supports the internal pressure armor and system internal loads in the radial direction.

4. Tensile Armor: The tensile armor layers consists of flat, round or shaped wires, in two to four layers crosswound at an angle between $20°$ and $60°$. It
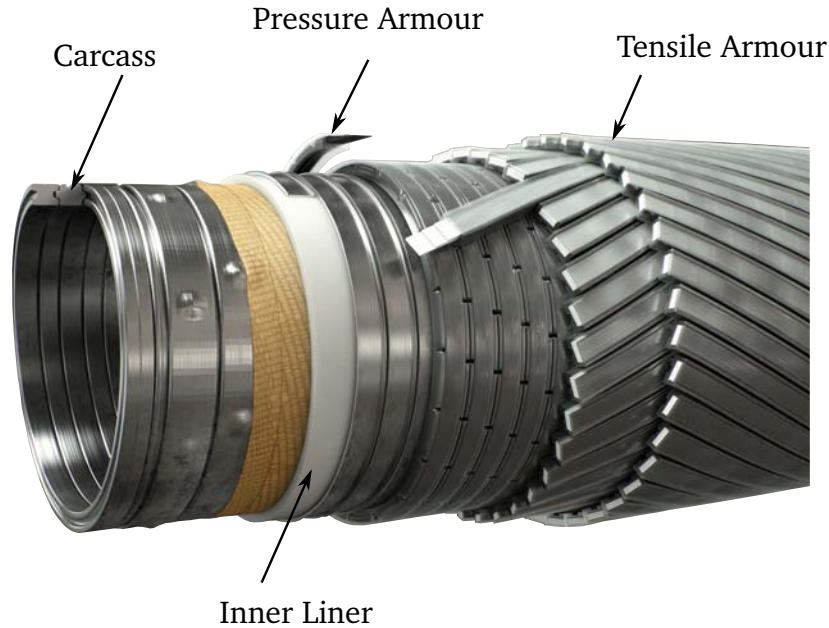
Figure 1.2: Flextreme concept [17].

supports the tensile loads in axial direction. The lower angles are used for pipe constructions which include a pressure armour layer, whereas pipes wound at a high angle may, in theory, allow for the exclusion of the pressure armoring layer.

1.3 Innovative Pipe Structure

One of the most prominent pipe projects involving fiber reinforced polymers (FRP) is the Flextreme concept [17], which intends to create a hybrid riser. The FRP composite flexible riser system is a further development of the concept. The main difference between other risers and the FRP composite flexible riser system is the material of the pressure and tensile armor. While steel was used in all load-bearing components until now, using composite materials in some layers offers many advantages. The most important is the improved strength to weight ratio.

The pipe structure of the FRP riser system in Fig. 1.2 has basically the same properties as conventional unbonded flexible pipes. The inner armor is a wound FRP structure held together in a protective cradle. Thin carbon fiber reinforced polymer strips are stacked in the cradle. Their number can be increased or decreased, based on strength requirements. The cradle can be wound with a certain spacing, to allow the pipe to bend.

The tensile armor is comprised of three or more thin rectangular tapes stacked in a PA cradle. The tapes are coated on each side with a thin thermoplastic adhesive,

which ensures good bonding between the layers. Upon production the thinner tapes are stacked together during the winding process, allowing thicker armor elements, where a thicker unibody tensile wire would be harder to deform, and would retain significant residual stresses. The minimal tensile strength of an armor element is 2/3 of total, and is caused by the need to continuously replace one of the tapes during the manufacturing process.

A flexible pipe terminates with two end-fittings, as shown in Fig. 1.3. They serve to connect the pipe to other structures and to seal all pipe layers. The flange is coupled via large bolts. The outer casing is pulled over the pipe and flange. It seals the outer sheath in cases where such layer exists. Several other components are used to seal and create a leak-proof environment with the inner liner. Steel tensile armor is anchored in the space between the flange an the outer casing, as shown in Fig. 1.3. The ends of the wires are twisted using a special tool. The cavity is filled with a mixture of epoxy resin and aluminum powder. When cured, the filler is hard enough to resist the wires pullout. The twisted wires and filler remain trapped in a v-shaped cavity.
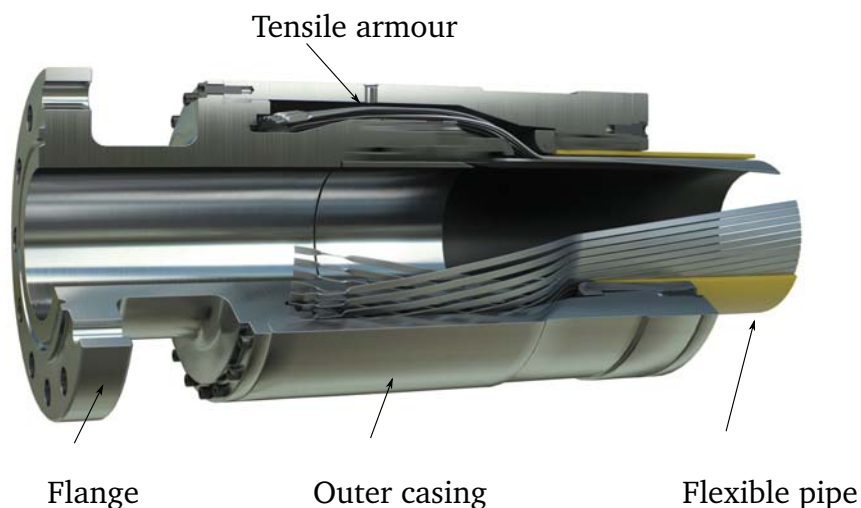

Figure 1.3: Typical end-fitting for unbonded flexible pipes. The tensile armor wires give the pipe its tensile strength. They terminate in the end-fitting, and have to be anchored in order to transfer loads from the pipe to the flange. The anchoring method is critical for the structural integrity of the pipe/end-fitting assembly.

1.4 Anchoring the Tensile Armour

The layout of the tensile armor elements have to change when the material changes from steel to composite armor. It is not possible to twist or apply any treatment that would damage the integrity of the unidirectional FRP. One of the

initial proposals is to re-create the 'twist' of the steel armor by inserting a metal wedge between two tapes [18].

Initial testing is done using a specially constructed tensile specimen. It consists of metal wedges glued between two tapes at each end. The ends of the specimen, together with the tapes, are cast into tubes using the aluminum powder epoxy normally used to cast conventional end fittings. Pullout tests have revealed several problems. There is a large scatter in the pullout force results. Specimens in the lower range had problems with improper curing of the resin. Bubbles of air and matrix material accumulated around the wedges and created small cavities, which did emphasize local creep. Resin creep has also been a problem when anchoring steel armour. In some cases one of the tapes peeled and was pulled out.

There are other aspects which have to be improved. Filling the end-fitting is a complicated process which requires special equipment. It makes very difficult to open the assembly after curing. It is not possible to inspect the wires without cutting them out, or to make any repairs. It is not clear how much of the load is transferred at the wedge area and what is taken by the rest of the cast area.

A novel method of anchoring the tensile armor is proposed. The basic idea is to use dry friction to transfer the loads to a mechanical grip. This solution offers many advantages, as opposed to adhesion:

- It is a more simple solution, with easier to control parameters.

- It gets away with curing problems.

- A mechanical grip can be disassembled, allowing inspection and repair.

- Several constructive solutions can be implemented, which can be developed in a patent.

- It is possible to transmit the entire load in a precisely defined contact area, thus eliminating the necessity to fill the end-fitting.

1.5 State of the Art

Studies into using composite materials as load-bearing components are first done for civil applications, such as pre-stressing composite cables. The anchoring has to be sufficiently strong, while at the same time minimizing stresses in the composite, as these can damage the composite materials, which are weaker in transverse direction. The type of anchoring can be divided into two main categories: bonded anchoring and mechanical solutions. While the first does not constitute the focus of this thesis, it is important to underlay their conclusions [19]. One major drawback of

bonded anchoring is the tendency to creep over time. The typical long anchoring length makes bonding ill-suited for applications which require small mounting space. Controlling the stress at the loaded end of the anchoring is also problematic.

Mechanical anchoring rely on the contact friction between the FRP tendon and the inner grip/anchor surface. Most of the studies focus on anchoring a composite circular tendon, the sort of which can be used to pre-stress bridges or concrete. Spike systems which are mounted inside a tendon composed of parafil ropes [20] press the material against a v-shaped barrel. An evolution of this system is the use of a sleeve and barrel design for gripping a CFRP tendon. A sleeve made of a soft metal is used to distribute more uniformly stresses to the tendon. The large compression force necessary to grip the tendon leads to high principal stresses at the loaded end. In order to mitigate this problem, the compressive stresses have to be transferred towards the back of the barrel. One solution is to use a very small difference between the sleeve and barrel angles [21]. Four wedges are distributed around the circular sleeve. These are cut to allow radial compression, and have rounded corners at the contact with the sleeve. Experimental and numerical analysis [22] shows that the rod slips first. After a certain load level is reached, the sleeve starts to slip, up to ultimate failure of the tendon. A further development is to allow for multiple differential angles to be created on the wedges and installed with a help of a seating steel plate [23]. The latest iteration of the barrel and wedge system makes use of a continuously changing profile, in the shape of a shallow curve [24]. This system produces good results with and without prestressing the grip. No sizing effects are reported.

The anchoring of a flat specimen is a less researched topic. There is a fair amount of research into the stress/strain state at the load transfer zone of flat specimens in uniaxial tension [25, 26], which includes analytic and finite element modeling. The studies show the importance of minimizing the stresses at the loaded end of the specimen, as well as the influence of the geometry of the tab and adhesive layer. The tabs are rectangular and are adhesively attached to the specimens. V-shaped grips made of steel and a thick epoxy sleeve are glued to CFRP strips [27]. The epoxy sleeve has a tapered profile, with the thicker part at the loaded end. Experimental results show an effective stress transfer to the rear of the grip, so that the specimens fail in the gage section, and not at the grips. All of these methods rely on adhesive bonding between the specimen and the grip. Direct load transfer using friction is used in a clamp design with two rectangular steel plates and a sleeve made of copper or aluminum [28]. The clamping pressure is applied using bolts.

1.6 Friction

The friction force appears when two bodies in contact try to move relative to each other, and it acts in a direction opposite to the direction of movement. There are three classical friction laws. The first two are described by Leonardo da Vinci in his Codex-Mardid I in 1495. The results were forgotten and rediscovered later by french physicist Guillaume Amontons (1699) [29]. Leonard Euler first used μ as the coefficient of friction, and introduced the notion that friction is caused by interlocking asperities between the contact surfaces. Charles Augustin Coulomb confirmed Amontons results and showed that sliding friction is independent of sliding velocity. With the publishing of his book, 'Theory of simple machines' in 1781, the clear difference between static and kinetic friction became established. He showed the contribution of adhesion, and established that the static force scales with the amount of time the bodies remain in contact.

According to this, the three classical sliding friction laws are summarized as follows:

1. Amontons I-st: The friction force is proportional to the normal force .

2. Amontons II-nd: The friction force is independent of the contact surface area.

3. Coulomb: The friction force is independent of sliding velocity in a first order approximation.

When two bodies are in contact, a critical force is needed to set the bodies in motion. This force is called the static friction force and is proportional to the normally applied force F_n.

$$F_s = \mu_s F_n \tag{1.1}$$

The static coefficient of friction μ_s is dependent of the materials in contact, but is independent of the apparent contact area, or surface roughness. In order to keep the bodies moving relative to each other, the dynamic friction force F_d must be overcome.

$$F_d = \mu_d F_n \tag{1.2}$$

The static and dynamic coefficients of friction are in the same range, but not equal.

$$\mu_s \neq \mu_d \tag{1.3}$$

The angle of friction is the angle at which a body lying on an inclined plane will begin to slide. The coefficient of static friction is the tangent of this angle.

$$tan(\alpha) = \mu_s \tag{1.4}$$

1.6.1 Friction mechanisms

When two bodies come in contact, the friction force which can be transmitted between them is influenced by the properties of the materials in contact and by the area of contact. The surface shape or topology of a material varies greatly between the macroscopic level and the microscopic level. It is influenced by the process through which the surface is created, and it always deviates from the ideal surface. The closer you look at a surface, the rougher it is, all the way to the atomic scale.
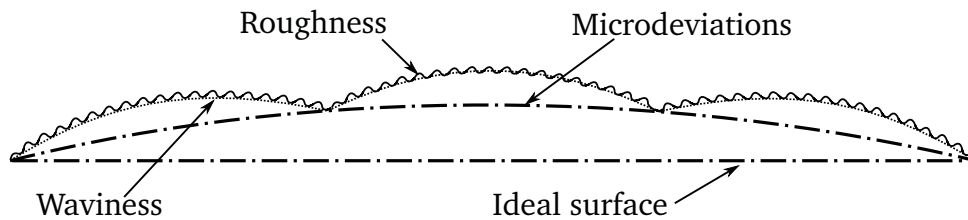

Figure 1.4: Surface deviations relative to an ideal solid surface, ASM handbook volume 18 [30] .

- Microdeviations are the largest deviation from the ideal surface, and are caused by the lack of accuracy during production.

- The waviness is a periodic, often sinusoidal, deviation. It is determined by oscillations during machining, and has wavelengths of 1 to 10 mm.

- Roughness is the deviation from the wavy surface caused by the geometry of the cutting tool and its wear.

At the microscopic level, friction is created by several mechanisms. The degree in which they influence friction is still the subject of debate, either with one dominant mechanism, or an accumulation of effects. Adhesion forces, the interaction of asperities which can either interlock or plastically deform the surface, fracture of oxide layers and plastic deformation caused by wear particles are the main contributors.

Bowden and Tabor [31] assumed that the real contact area is much smaller than the apparent area of contact,

$$A_r = \frac{N}{H} \tag{1.5}$$

where N is the normal force [N] and H is the indentation hardness [N/m2]. The friction force is produced by the shearing of the asperities in contact, making μ become:

$$\mu = \frac{F}{N} = \frac{A_r \tau}{A_r H} = \frac{\tau}{H} \qquad (1.6)$$

with τ the shear stress. For metals $H \approx 3\sigma_y$, where σ_y is the flow stress, and $\tau \approx 0.5$ to $0.6\,\sigma_y$.

1.6.2 Polymer friction

Polymers have elastic modulus values much lower than that of metals. Their low stiffness and strength makes them very compliant in comparison to metals. In order to improve rigidity, they are reinforced with fibers to form composites.

Polymers sliding against hard metal surfaces result, in some cases, in the transfer of material to the harder surface. The thin film layer which is formed and transfered influences the friction and wear properties, because it changes the contact from metal on polymer to polymer on polymer, [32] chapter 5. The sliding distance influences μ, because once the polymer film is transfered, further sliding just adds wear particles. In time, a thin strong chain of polymer molecules is formed, with the chains parallel to the sliding distance. This is what happens in the case of high density polyethylene sliding on a glass surface. When the transfer film is thick, μ is initially high. After a short distance the friction drops to a much lower value, as shown in Fig. 1.5. At this stage a thin transfer film is already formed, and it adheres perfectly to the glass substrate.
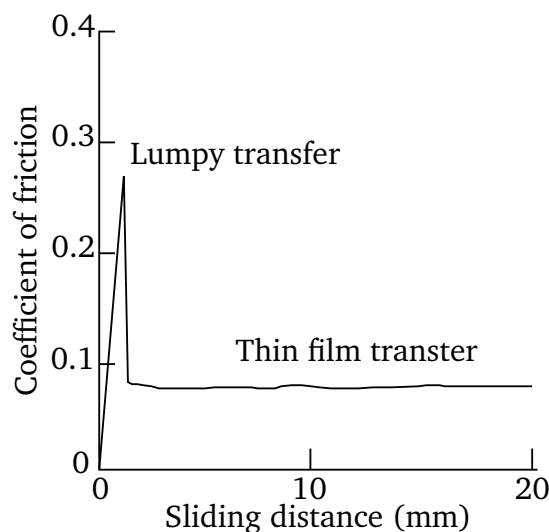

Figure 1.5: Coefficient of friction as a function of sliding distance for high density polyethylene sliding against glass [33].

The plasticity in the contact region is determined by the mechanical property ratio E/H and the surface roughness, [32] chapter 3. This is because polymer asperity deformation is elastic, which is the main difference between metal and polymer friction.

Adhesion plays an important role in the friction of polymers. The surface roughness and the normal load affect the coefficient of friction. On surfaces which are not exceedingly rough, increasing the contact pressure deforms the asperities in contact. If the load is high enough, the contact surface cannot be increased anymore. This will result in an inverse relation between μ and normal load [34].
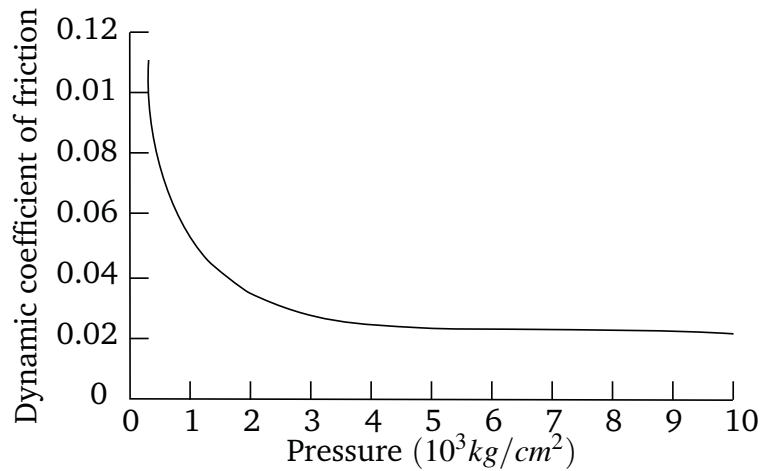

Figure 1.6: Dynamic coefficient of friction of high density polyethylene as a function of pressure [35].

The decrease of the dynamic coefficient of friction in the case of polymers is shown in Fig. 1.6. Here high density polypropylene is deposited on soda-lime glass. A steel slider traverses the films at different pressures. In this case

$$\mu = \frac{\tau_0}{p} + k \tag{1.7}$$

k is the adhesion part and τ_0 the shear strength. p is the applied pressure. At low pressures, the τ_0/p factor is dominant, resulting in higher μ_d. As p increases, τ_0/p becomes negligible. What is left is the a adhesion contribution k. For this reason, μ_d cannot drop under the k value.

Chapter 2

Summary of Results

The first part of this chapter presents details on the experimental setup and procedures, as well as the finite element models used over the course of this thesis. Having established a frame of reference, it is possible to focus solely on the results. Details on the obtained results are presented in 4 papers, denoted A-D.

Experimental results using rectangular grips are presented in Paper A. Here, the relation between the normal force applied to the contact area and the resulting pullout force is investigated. The static coefficient of friction is evaluated for the FRP material and bulk polymers. Pullout results are compares to measure the grip efficiency and material dependency. Furthermore, short investigation of wear patterns is done using scanning electron microscopy. In Paper B the finite element model of the grip used in Paper A is used for the parametric study of the influence between the coefficient of friction and pullout force. The experimental results from Paper A are used for input and benchmark purposes. Numerical and analytic solutions are used in Paper C to find the optimal grip geometry which minimizes stresses at the contact with the edges of the grips. Experimental and FE parametric analysis of an improved grip design is presented in Paper D.

2.1 Experimental Procedure

The experimental part of the project deals with the development of a test procedure for carrying out pullout tests.

Everything can be divided in two main categories: tools and procedures. The tools consist of all the equipment which is used, and includes the test rig as well as data acquisition devices. The equipment has to allow the operator to accurately control the conditions of the test, and to be flexible enough for the implementation

of several constructive solutions. The test rig itself is shown in Fig. 2.1 and consist
of two stiff steel plates which clamps the grips and the composite specimen in the
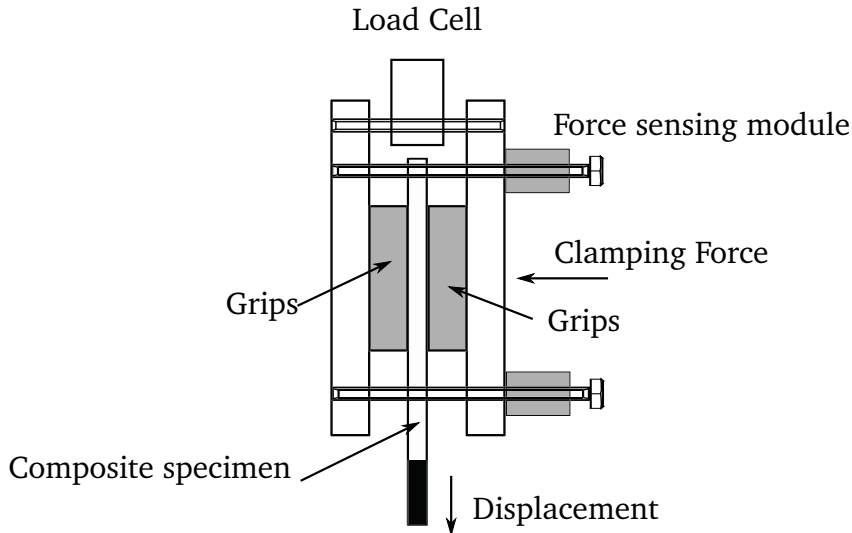middle.

Figure 2.1: Test rig for tensile tests. The specimen is placed in the middle, between the grips.
The clamping force is controlled via dedicated force sensing modules. Displacement is applied
to the lower part of the specimen. The pull-out force is sampled with the load cell on top.
Digital image correlation is used to record displacement in the clamped area of the specimen.

The grips are interchangeable, and are constrained from displacement in all direc-
tions. The clamping force is applied using four bolts, which all go through custom
built force sensing modules, shown in more detail in Chapter 4. Using this setup it is
possible to monitor the exact clamping force during the entire test. The test rig is
installed in a MTS universal tensile machine. During testing, displacement is applied
to the composite specimen, and the resulting force is measured using a load cell.

   Building an accurate custom force sensing module is achieved using a length of
pipe, to which 2 strain gages are glued on each side in the middle of the tube. The
combined strain signal is used to calculate the compression force in the tube. Before
use these modules were calibrated in compression, using a universal hydraulic tensile
machine. Five repetitions are done for each device, up to 50 % of yield. Averaging
the two strain signals results in a linear relation, as shown in Fig. 2.2. from the figure,
the slope k can be deduced. In future measurements it is used as the conversion
factor between strain and the compression force. During measurements, the strain
signal is sampled using a Spider8 module, which supports a total of 8 full bridges.
Computation channels are used in the Spider8 controller software, and calculate
the force in real time, via the conversion factor. Because strain measurement is
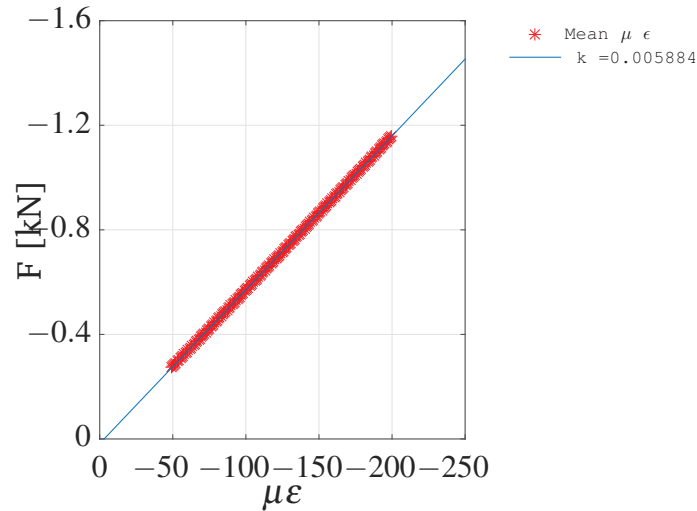supported only in full-bridge configuration, which is not a built-in feature, eight 3/4

Figure 2.2: Strain gauge calibration. Five compression tests are done up to 50 % of yield for each force sensing module. The average value of the factor k is used to convert from strain to force.

bridges are assembled, and can be seen in Chapter 4, Fig. 4.6. The pullout force and the actuator displacement are sent from the MTS controller to a second Spider8 module, that works in parallel with the one assigned for strain measurement. By doing so, the normal and pullout forces are tracked simultaneously.
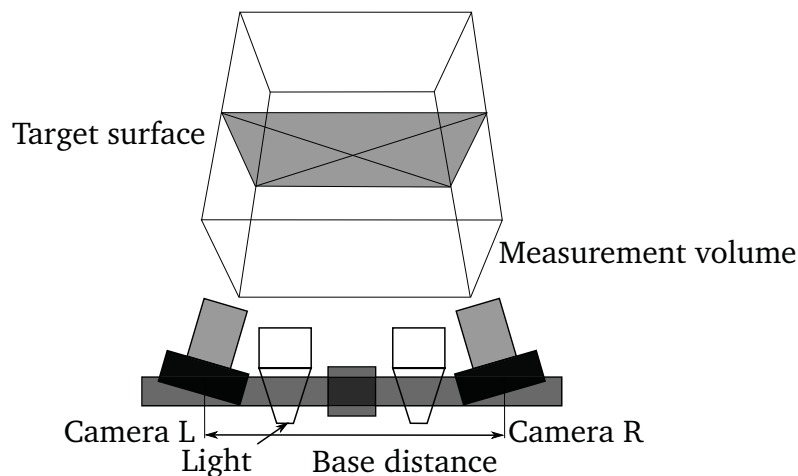

Figure 2.3:   Aramis optical 3D measurement system [36]. Two cameras are used to take images of the test rig, which is placed inside the measurement volume. The size of the measurement volume is given by the base distance between the cameras and the distance to the object. The target surface must be painted in a random black and white pattern, which allows the software to identify and track the displacement of small facets on its surface.

One of the difficult tasks of the project is the reliable tracking of displacement in the contact area between the grips and the FRP tendon. The displacement of the

hydraulic actuator cannot be used for several reasons: it is not accurate enough due to the elasticity of the load-train and the FRP specimen, it does not offer any information about the status of the contact, and it makes it impossible to identify the exact onset of displacement in the grip. To overcome this, an Aramis 3D digital image correlation system is used. The Aramis optical 3D measurement system [36] is capable of measuring strain and displacements with great accuracy. It uses two cameras to take images of the entire contact area between the grips and FRP tendon, by placing the test rig inside the measurement volume, as shown in Fig. 2.3.

Carrying out a test involves simultaneous operation of three components: the tensile machine to apply displacement, the Spider8 system to measure the normal force, and the DIC system to record displacement. All systems are synchronized via a common trigger signal. The same sampling frequency is used for both force and displacement channels.

The procedures refer to how to handle the displacement of the FRP tendon in the contact area. A total of 9 reference points are used. 3 are used for each grip, as well as the FRP tendon. As shown in Fig. 2.4, P1 is closest to displacement application, and P3 is the point at the unloaded end of the grip.
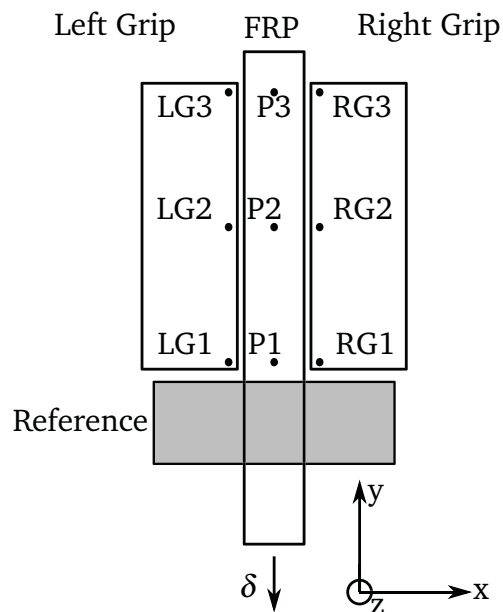

Figure 2.4: Aramis stage points. Nine references are distributed on the specimen and on the grips. The displacement of these points is tracked during the entire pullout test. It is possible see if the grips stay in contact with the FRP tendon, and when slip occurs. P3 is the farthermost from displacement application and its movement is the failure criterion for the grip. A reference surface is used to correct for rigid body movement.

The maximum load that the grip can handle is here defined as the onset of displacement of P3, relative to the grips. During pullout, at low normal forces,

slip of the FRP tendon in the contact area happens almost simultaneous. In the case of higher loads, slip happens gradually, as shown in Fig. 2.5. It is clear that P1 displaces first, followed by P2 and P3. Looking at Fig. 2.5 a, it is very hard to identify the exact moment at which pullout happens, because of the very small displacements. In the beginning, P2 and P3 move together, and is unclear exactly when they start to deviate. A logarithmic x-scale allows to zoom in ans see what is the initial displacement.
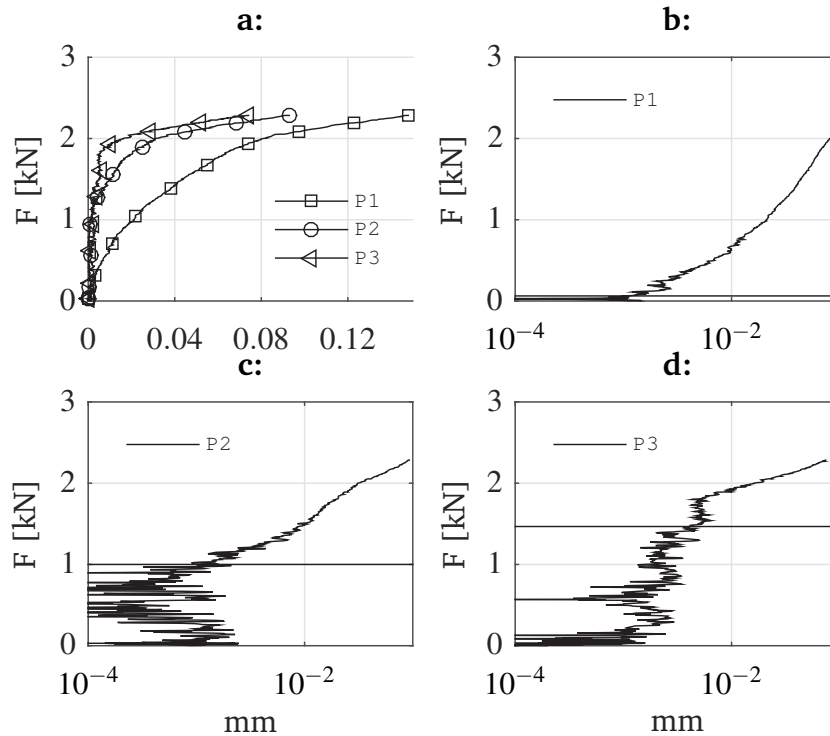

Figure 2.5: Pull-out test using 8 kN normal force. The FRP extends on both sides of the grip. In the three subplots the logarithmic scale is used to zoom in the initial displacement. P1 is the point closest to force application. P3 is the point furthest from force application. The horizontal line shows the force value at which the FRP starts to slip.

Because any elongation of the tensile armor is detrimental to the pipe, it is necessary to remove any possible slip. In the beginning there is a significant amount of noise in both Fig. 2.5 c and d. As the load increases, the displacement starts to increase, and a clear pattern emerges. A horizontal black line is used to mark the pullout load value. P2 in Fig. 2.5 c slips smoothly, but P3 in Fig. 2.5 d has a pronounced stick-slip behavior. The critical load is taken at the first clearly identifiable slip.

2.2   Finite Element Model

The numerical analysis is done using a 2D finite element model built in Ansys 15.0. The model in Fig. 2.6 consists of two aluminum grips and a unidirectional basalt fiber reinforced polymer squeezed in between. The grips are clamped against the FRP with a pressure P, and the friction force F develops when pulling out the right end of the composite. The origin of the coordinate system for the entire model is located to the left side of the assembly. The x-axis is running horizontally, and the y-axis is in vertical direction. The grips have a rectangular shape, and the length l_g and height h_g are defined parametrically. The angle between the vertical faces of the grips and the FRP is α. The composite is thin compared to the grips, with thickness $h_c = 1.5$ mm. It can either extend on both sides of the grips, or only towards the loaded and of the grip.
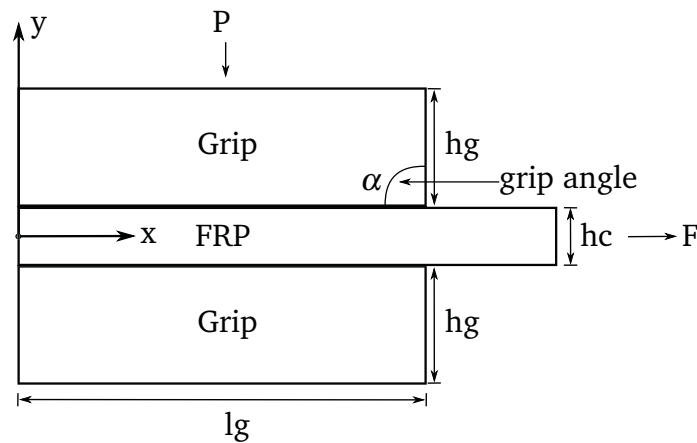

Figure 2.6: Model geometry. The system consists of two grips and a unidirectional basalt fiber reinforced polymer in between. The grips have length lg, and height hg. The FRP is extending beyond the right end on the grips, and has the thickness hc. A clamping pressure P is applied to the top grip. The friction force F is obtained by pulling the FRP in x direction.

The model is meshed with a 2D 8-node solid element. A plane stress definition is used. To keep the size of the model to a minimum, and to have good accuracy where the corners of the grips come in contact with the FRP, the finite element mesh is more dense towards the corners of the grip. The same line division ratio is used in both the grips and the FRP, and is shown in Paper A, Fig. B.4. This same line division ratio ensures that the solid element nodes are in perfect initial overlap. In this model there are two contact areas between the grips and the FRP, which are modeled with 2D 3-node surface-to-surface contact elements. The FRP, which is more deformable, is the contact surface. The target surface is defined on the grips. CONTA172 and TARGE169 contact elements are generated on top of the solid elements. The contact pair is generated automatically by the software, which

matches the nodes that are at the same position. The initial contact status is closed, and effects of initial inter-penetration are excluded. Contact detection is set at the nodes. A value of 0.1 is used for the normal penalty stiffness factor, which minimize chatter and convergence problems. The value is recommended in the user manual for contact pairs which have greatly different stiffnesses.

A specific coefficient of friction can used in each contact surface. An isotropic friction model is used, because the FRP is unidirectional. Based on experimental tests, the static coefficient of friction between aluminum and vinylester reinforced basalt fiber in longitudinal direction is 0.25 [1]. When contact status changes from stick to slip, there is a drop from the static coefficient of friction μ_s, to the dynamic coefficient of friction μ_d. This behavior can be modeled in Ansys using the ratio μ_s/μ_d between the static and dynamic coefficients of friction.

The grips are modeled as isotropic aluminum, with $E_x = 69$ GPa and $v_{xy} = 0.33$ for aluminum. The FRP is modeled as an orthotropic material. This is done using a micro-mechanics approach based on fiber volume fraction and material properties of the fibers and matrix provided by the manufacturer. The transverse elastic modulus is $E_y = 9.51$ GPa. The shear modulus in principal direction is $G_{xy} = G_{xz} = 6.23$ GPa, and the transverse shear modulus is $G_{yz} = 2.59$ GPa. The major Poisson's ratios are $v_{xy} = v_{xz} = 0.29$ and the minor Poisson's ratio is $v_{yz} = 0.32$. Five longitudinal tensile tests have resulted in a longitudinal elastic modulus $E_x = 41.88$ GPa.

Two load steps are used to model the behavior of the grip. In the first load step, a uniformly distributed pressure is applied to the top grip. The boundary conditions for the first load step imply constraining the top line of the top grip against movement in x direction. The grip is allowed to slide vertically, and pressure is applied uniformly at the top line. The lower grip is constrained in all directions at the bottom line. The nodes at the right end of the FRP have a coupled degree of freedom. In the second load step, displacement is applied to the master mode of the coupled degrees of freedom. Because contact is nonlinear, a nonlinear solver which includes large geometrical effects is used.

2.3 Paper A: Experimental Pullout using Flat Grips

The main results from Paper A are summarized in the following section. Experimental pullout tests are done using the test rig and procedures described in Section 2.1. The purpose of these tests is to determine what is the relation between the normal force and the pullout force for this type of grips, and to make it possible to understand the processes which take place in the contact area. Benchmarking with clean bulk polymers is done to check the influence of fiber reinforcement.

The basalt fiber reinforced specimens are made by Vello Nordic AS, using a proprietary vinylester matrix. Because no information about the coefficient of friction is provided, it is necessary to measure it experimentally. The static coefficient of friction μ_s is measured using grips with an arithmetic mean surface roughness $Ra = 0.316\,\mu m$ and a standard deviation of 14.5%. The maximum height of the roughness profile is $Rz = 2.076\,\mu m$.
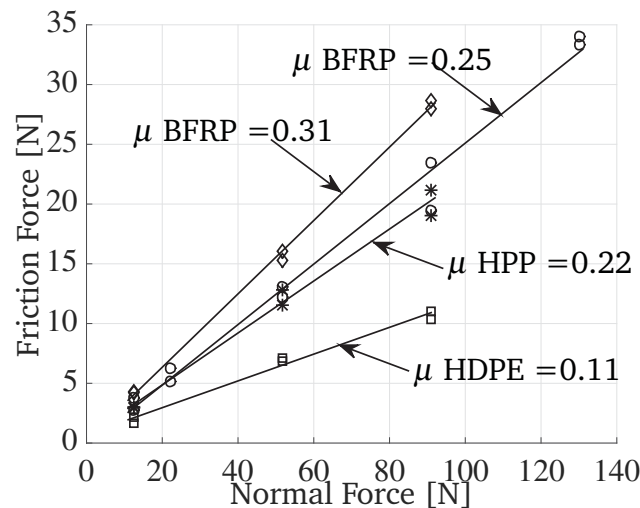

Figure 2.7: Static coefficient of friction. Basalt fiber reinforced polymer (BFRP), polypropylene (HPP) and high density polyethylene(HDPE).

One grip is dragged over the FRP, and the normal force is provided by dead weights. μ_{BFRP} in Fig. 2.7 is between 0.25 and 0.31. The result difference is caused by the different technique used to cut the samples. Bulk polymer samples are used as benchmark. In the case of polypropylene, $\mu_{PP} = 0.22$ For high density polyethylene $\mu_{HDPE} = 0.11$. These results are in range with Bowers [35]. The results for BFRP and PP are very close, and the difference can be caused by the interaction with the fibers of the composite.

Pullout tests are done with the FRP tendon gripped between the rectangular grips. The contact area is 50x15 mm^2. Five normal force (F_n) values are used, and five tests are done at each level. The specimen and the grips are cleaned before each

test. The results in Fig. 2.9 a are obtained using two configurations. In configuration a the FRP extends just on the loaded side of the grips, while in configuration b the FRP extends on both sides of the grips. This arrangement is detailed in Fig. 2.8.
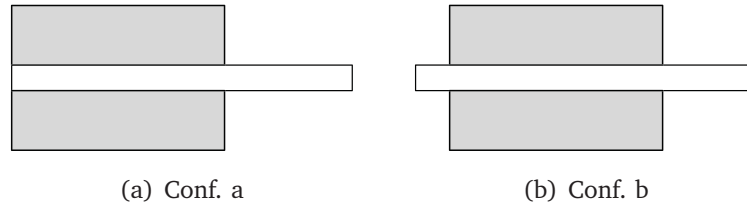

(a) Conf. a   (b) Conf. b

Figure 2.8: Test configurations showing the FRP specimen and clamp configuration. In 2.8(a) the specimen does not extend outside of the grips. In 2.8(b) the specimen extends on both sides of the grip.

The pullout force is linear for both arrangements up to a clamping force of 8 kN. After this value the configuration b results deviate from linearity. Because the material is the same in both cases, the drop in pullout force can be caused by small changes of the contact angle between the grips and the FRP at the unloaded end of the FRP [37]. Inspection of the specimens did reveal small deformations of the FRP at the contact with the corner of the grips. All results are characterized by large scatter, but it is much more obvious for configuration b results. It also scales up with increasing clamping force. It can be concluded that it is optimal to install the FRP so it extends outside of the grips only on one side, towards load application.

Pullout tests with bulk high density polyethylene (HDPE) and high density polypropylene (HDPP) are compared with previous results in Fig. 2.9 b. Only the polynomial fits are used, to make the comparison more obvious. For all cases the specimens did extend on both sides of the grips. Although not presented here, there is almost no scatter in these results, as can be seen in Paper A, Fig. A.8. HDPE results are clearly much lower than the rest. It is the HPP which gives the same behavior as the FRP, up to 8 kN clamping force, although μ is la little lower. After that value, it starts to decrease. These results show that the grip system is not extremely sensitive to the coefficient of friction, and that it can not be used to measure it. Metal to matrix contact is dominant, with no visible influence from the fibers. The ratio of the pullout force to the clamping force (F_x/F_n) will be called from here on the grip coefficient.

While there is no direct influence between the surface roughness and μ, the grip coefficient can be increased using sandblasted grips. The second set of grips has a mean surface roughness $Ra = 3.969\,\mu m$ and a standard deviation of 7.9%. The maximum height of the roughness profile is $Rz = 24.175\,\mu m$. For all tests, the FRP did extend on both sides of the grip.
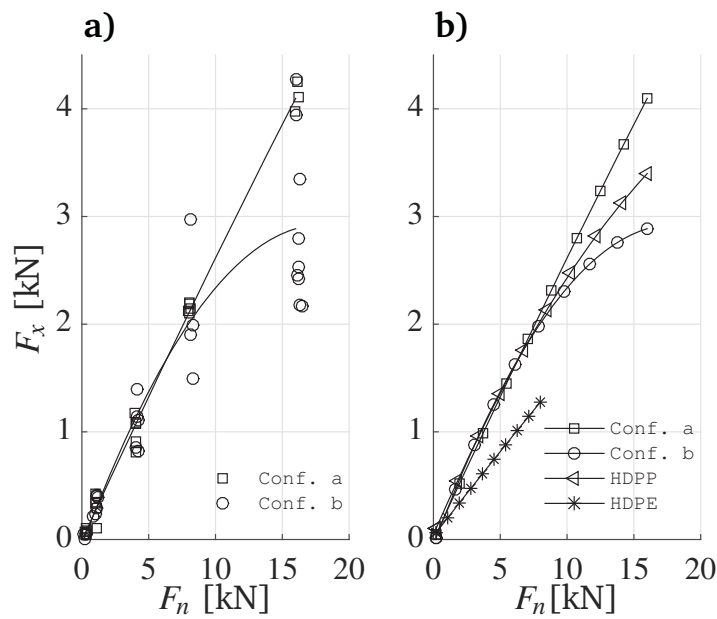
Figure 2.9: The required pull-out force (F_x) to move the furthest point from force application (P3) from the grips. (F_n) is the normal force. In conf. a the specimen did not extend on both sides of the grip. For conf. b the specimen did extend on both sides of the grip. The lines are a polynomial fit. FRP pullout tests are presented in a. These are benchmarked against high density polyethylene (HDPE) and high density polypropylene (HPP) in b.
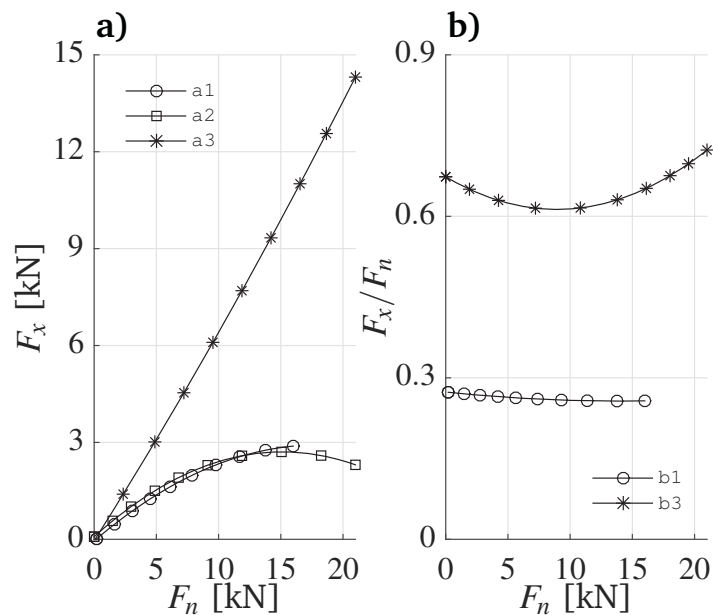

Figure 2.10: In a, line a1 represents are obtained with smooth grips. Line a2 results are obtained with sandblasted grips. Line a3 is the absolute maximum pullout with sandblasted grips. For all configurations the FRP did extend on both sides of the grips. The grip coefficient F_x/F_n in b is obtained with smooth (b1) and max sandblasted grips (b3).

Looking in Fig. 2.10 a, at the F_x value necessary to obtain displacement in the entire contact area, there is almost no difference between using smooth (a1) and sandblasted grips (a2). This means that the real contact area is similar in both cases. F_x reaches a plateau with increasing F_n, showing that the pressure is not sufficient to increase the contact. Once the FRP tendon starts to slide, the larger asperities dig themselves in the matrix, and the pullout force increases dramatically. The absolute maximum F_x value is given in line a3. A comparison of the grip coefficient F_x/F_n is given in b. For smooth grips, line b1, the value is around 0.25. Line b2 represents the normalized results of a3. The increase of line b2 is caused by the contact with the FRP fibers.
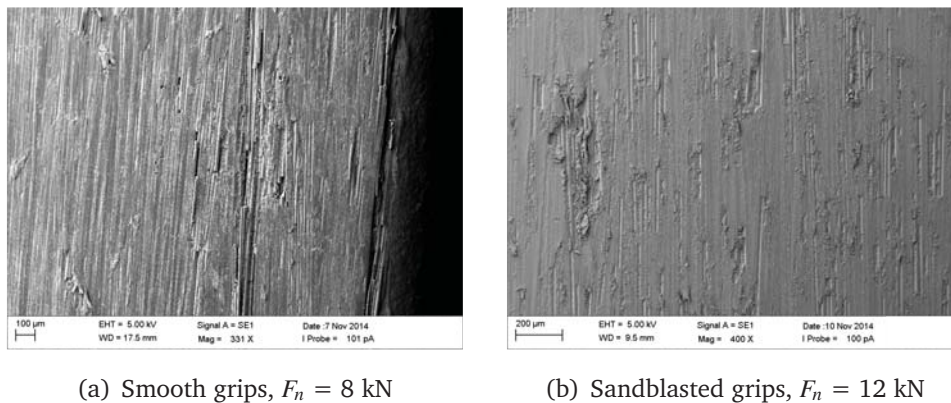

(a) Smooth grips, $F_n = 8$ kN   (b) Sandblasted grips, $F_n = 12$ kN

Figure 2.11: Wear pattern comparison. Pullout tests using a smooth surface, see (a), result in a large, but localized scar. The damage from sandblasted grips, as shown in (b), is more uniformly distributed over the contact area. The scars are smaller and not very deep, with the matrix being plastically deformed from on top of the first fiber layer.

Wear patterns in Fig. 2.11 show that in the case of smooth grips, the contact is mainly matrix to metal. Because there is no evidence of plastic deformation in Fig. 2.11 a, where most of the contact surface is intact. Damage is localized in the shape of a big hole in the matrix and broken fibers. The sandblasted grips produce a more uniform wear pattern in Fig. 2.11 b. The matrix is plastically deformed over a larger area with visible drag marks. In addition to providing a higher grip coefficient, the contact with sandblasted grips did not produce fiber breakage. The less serious damage results in improved lifetime of the system.

2.4   Paper B: Numerical Contact Modeling

Paper B contains the results of finite element analysis of the grip system that is experimentally investigated in Paper A. The analysis is necessary to understand the processes that take place at the contact between the grips and the FRP tendon. A detailed parametric analysis involving the coefficient of friction is done. The model consists of the two rectangular grips which compress the FRP tendon in between. Details of the geometry and mesh of the model are given in Paper B, Fig. B.3 and B.4. All information about material properties and contact definition can be found in Section B.2.
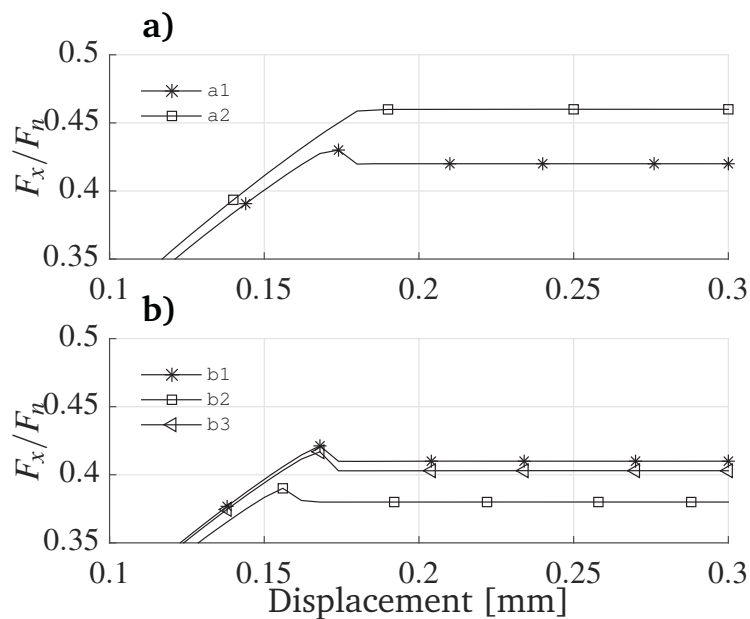

Figure 2.12: Effect of friction on the grip coefficient F_x/F_n. A normal clamping force $F_n = 8$ kN is applied to the top grip. The displacement applied to the right end of the FRP is 0.3 mm. In a, results are compared between: a1) $\mu_d = 0.21$, $\mu_s/\mu_d = 1.2$ in both contact areas; a2) different coefficients of friction between contact areas $\mu_{d1} = 0.25$, $\mu_s/\mu_d = 1$ and $\mu_{d2} = 0.21$, $\mu_s/\mu_d = 1$. In b, results are compared between: b1) $\mu_{d1} = 0.21$, $\mu_{d2} = 0.2$, with $\mu_s/\mu_d = 1.2$; b2) $\mu_{d1} = 0.21$, $\mu_s/\mu_d = 1.2$ with $\mu_{d2} = 0.17$, $\mu_s/\mu_d = 1.2$ and b3) $\mu_{d1} = 0.21$, $\mu_s/\mu_d = 1.2$ with $\mu_{d2} = 0.19$, $\mu_s/\mu_d = 1.3$.

Initial FE analysis shows that the pullout force F_x is greatly over-estimated, unless special consideration is used in handling the contact friction. Since previous experimental results focus on the static coefficient of friction μ_s, additional tests are done using a tribotester. These show that the dynamic coefficient of friction μ_d is about 20 % lower than μ_s. The analysis in Paper B, Fig. B.8, shows that the maximum grip coefficient F_x/F_n decrease is directly kinked to the ratio μ_s/μ_d. The maximum F_x/F_n value is achieved at the moment where the entire contact area starts to slide.

The larger μ_s/μ_d is, the lower F_x/F_n max is, coupled with a lower value for fully dinamic friction. Based on tests with the tribotester, μ_s/μ_d cannot be chosen arbitrary to fit the model, and the value of 1.2 is physically representative. Measurements of the static coefficient of friction in Fig. 2.7 show that μ_s is influenced by the surface preparation. It is possible that there are some small variations between the two contact surfaces of the FRP tendon with the grips.

Two cases are considered in Fig. 2.12. In a, line a1 shows that if the same coefficient is used in both contact areas, F_x/F_n decreases more when μ_d is 20% lower than μ_s. If the static friction in one of the contact areas is 20% lower than in the second contact area, and there is no change between the static and dynamic regime, F_x/F_n in line a2 is higher than a1. The added effect of different friction between the contact areas together with transition from μ_s to μ_d is given in Fig. 2.12 b. For line b1, the values of μ_s in the two contact areas are very close, and for both the same ratio $\mu_s/\mu_d = 1.2$ is applied. For line b3, the static friction is the same as for line b1, but the dynamic difference is slightly increased. The drop in F_x/F_n is visible, but small. Line b2 shows that the strongest effect is obtained when both μ_s and μ_d are significantly different between the two contact areas.
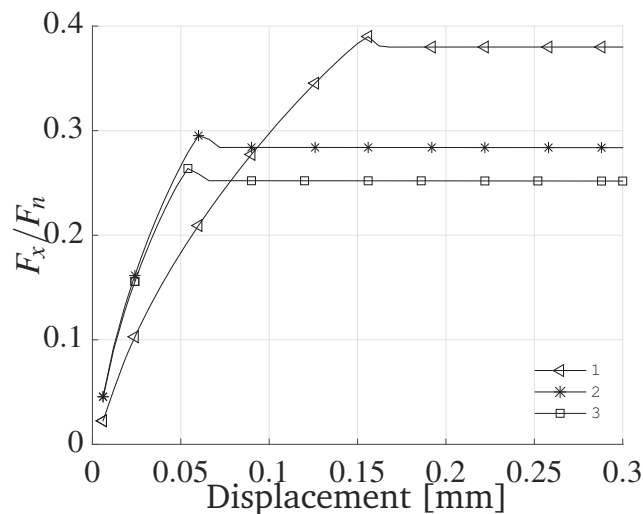

Figure 2.13: Model calibration. Different coefficients of friction are used in the two contact areas between the grips and the FRP. In one contact area $\mu_{d1} = 0.21$ and $cof_s/cof_d = 1.2$. In the second contact area $\mu_{d2} = 0.17$ and $\mu_s/\mu_d = 1.2$. Perfect contact is used for the results in line 1. A normal clamping force $F_n = 8$ kN is applied to the top grip. In line 2 only 75% of the area remains in contact. This value is decreased to 67% for the result in line 3.

With these parameters, the contact status changes from stick to slip in a zipper-like fashion in the two contact areas. When load is applied to the FRP tendon, the contact shear stress increases toward the unloaded end, as shown in Paper B, Fig. B.6. Experimental results show that when the FRP tendon extends just on one side

of the grips, the grip and friction coefficients are close. So, doubling the apparent contact area did not double F_x/F_n. An algorithm that cancels the contribution of some contact elements is used, as shown in Paper B, Fig. B.10. The procedure is to choose contact and target pairs with the same location and to change both μ_s and μ_d to zero. As the number of disabled contact elements increases, the F_x/F_n decreases. Legend b shows that numeric results are linearly dependent on the contact area.

This algorithm is incorporated and used for the results in Fig. 2.13. The same friction parameters are used in all of the compared cases. Line 1 is the benchmark, with the entire area in contact. Line 2 is obtained when the contact area is reduced with 25 %. F_x/F_n and the displacement required to achieve pullout are greatly reduced. For line 3, the contact is reduced with 33 %, and the numeric and experimental F_x/F_n values match. This shows that, under certain conditions, the FE model of the grip is accurate. In Paper B, Fig. B.12, the FE displacement of the FRP tendon in the contact area is shown to be in range with experimentally obtained data.

2.5 Paper C: Contact Stress Optimization

The parametric study of the stress concentration at the contact between the corners of the grip and the FRP tendon is presented in Paper C. Analytic and finite element results are combined to find a grip solution which minimizes peak stresses. The same basic geometry and material properties are used, as in Paper B, with the difference that the grip angle α can be parametrically defined with values lower than 90°. A thorough investigation is done, with regard to the relation between the coefficient of friction and the stresses in the grip and FRP material.
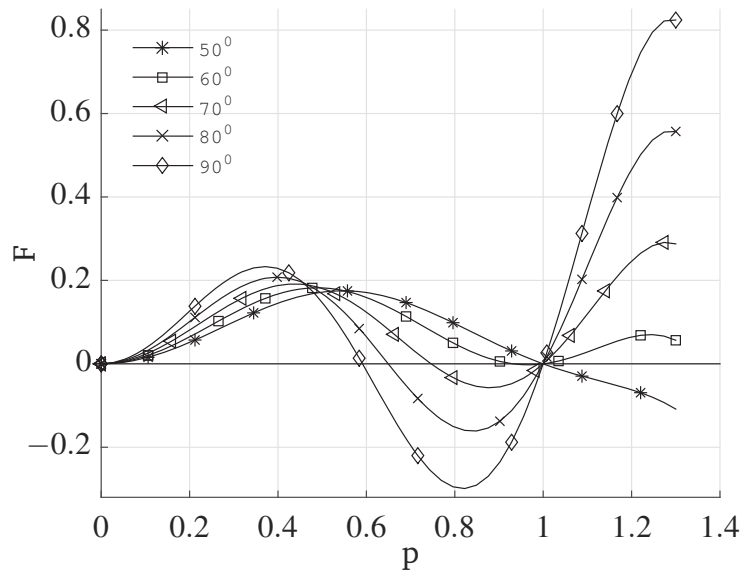

Figure 2.14: p is the non-trivial solution of the function F developed by Comninou [38]. The grip angle takes values between 50° and 90°. The coefficient of friction between both surfaces is $\mu = 0.25$.

The function in Fig. 2.14, developed by Comninou [38], is a further development of the work done by Dundurs and Lee [39] with the inclusion of friction. The function F changes sign for p in the interval $0 < p < 1$. The shape of F is dependent of the grip angle α. If real root of p is obtained, it means that a stress singularity exists for the given parameters. Knowing this, F is used to estimate the value of α at which a stress singularity develops. For the aluminum to FRP contact, with $\mu = 0.25$, the first clear root of F develops at $\alpha = 70°$. Decreasing μ results in a decrease of the minimal grip angle. For the same calculation with $\mu = 0.15$, a solution is obtained when $\alpha = 60°$.

The maximum stress at a corner grows asymptotically no faster than $r^{(p-1)}$, where Aij is the uniformly distributed stress and r is the distance to the corner. The way in which the analytic solution is used to calibrate FE results can be seen in Paper C, Fig.

C.7.

$$\sigma_{ij} = Aij * r^{(p-1)} \tag{2.1}$$

The results in Fig. 2.15 are obtained when the FRP is compressed by the grips. A grip angle $\alpha = 90°$ is used. It is found that the maximum normal and longitudinal stresses decrease when μ increases. This happens simultaneously with an increase in shear, and shows that more load is transferred through contact shear stresses between the grips and the FRP. Because the normalized shear stress is much lower than the normal stress, an increase in friction proves doubly beneficial. First, it improves the grip efficiency, and secondly it helps in lowering normal and longitudinal peak stresses. From Fig. 2.15 there is a minimal difference between the case when the FRP extends on both sides of the grip, or just towards the loaded end.
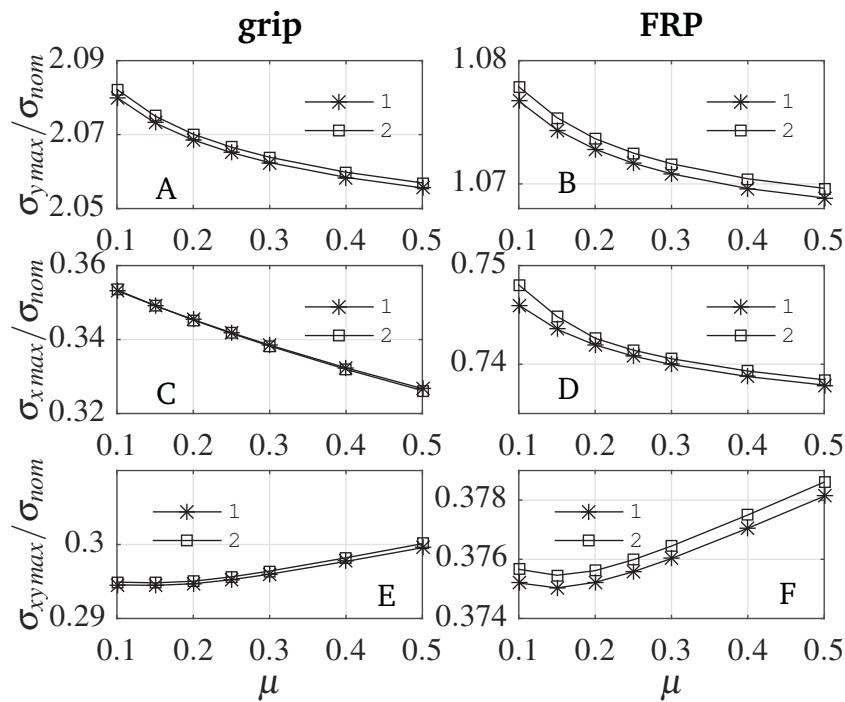

Figure 2.15: FEA results for the maximum normal stress σ_{ymax}, longitudinal stress, σ_{xmax}, and the shear stress τ_{xymax}. The results are normalized with the nominally applied stress $\sigma_{nom} = 5.33$ MPa. For line 1 the FRP did not extend beyond the unloaded side of the grip. For line 2 the FRP did extent on both sides of the grip. Wedge angle $\alpha = 90°$. The grip length is 50 mm.

Because in the FE model the grip and FRP are not bound together, a limited amount of slip between the surfaces takes place. The strain and the stress is different in the two materials. The normal stress in the grip and FRP tendon are presented in Fig. 2.16. Al results are normalized with σ_{nom}. The largest peak stresses develop for $\alpha = 90°$. In the case of the grip, in Fig. 2.16 a, when $\alpha = 70°$, the stress increase at

the corners is much lower than the average distributed stress. An even better result is obtained for the FRP, Fig. 2.16 b. Because it is more elastic, the peak stresses are very low. Even for 90°, the value barely exceeds the value of one. For static conditions, no significant difference is found between the case when the composite extends on both sides of the grip or not.
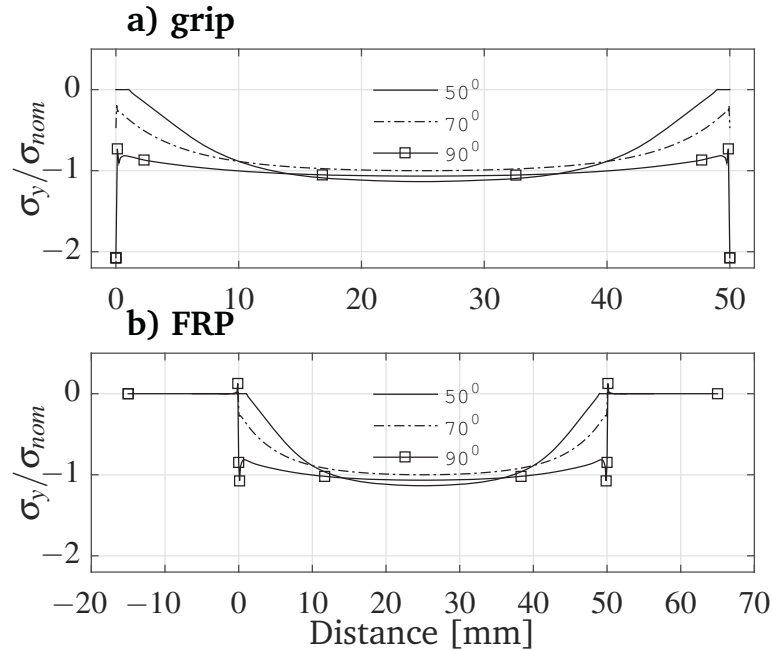

Figure 2.16: Stress distribution in the grip and FRP tendon, when the grip angle is $\alpha = 50°$, 70° and 90°. σ_y is the normal stress. The FRP did extend on both sides of the grip. The coefficient of friction is $\mu = 0.15$. The results are normalized with the nominally applied stress $\sigma_{nom} = 5.33$ MPa.

The performance of the grip system during pullout is mostly influenced by the μ value, and then by the geometry of the grips. The results in Fig. 2.17 are obtained by applying displacement to the FRP, after the tendon is clamped in the grips, and a uniformly distributed stress σ_{nom} is applied to the top grip. When α s constant, the pullout force is always lower when using different coefficients of friction between the two contact areas, and when the static coefficient μ_s is larger than the dynamic coefficient μ_d. Lines 2, 3, and 6 in Fig. 2.17 show that there is a noticeable drop in F_x as the grip angle α is reduced from 90° to 50°.

The optimal combination is attained for $\alpha = 70°$, a grip angle that does not completely remove corner effects, but their value is insignificant. A stick-slip effect is obtained for lines 4 and 5. It indicates that the unloaded end of the grip performs a cyclic elastic deformation of the FRP tendon.
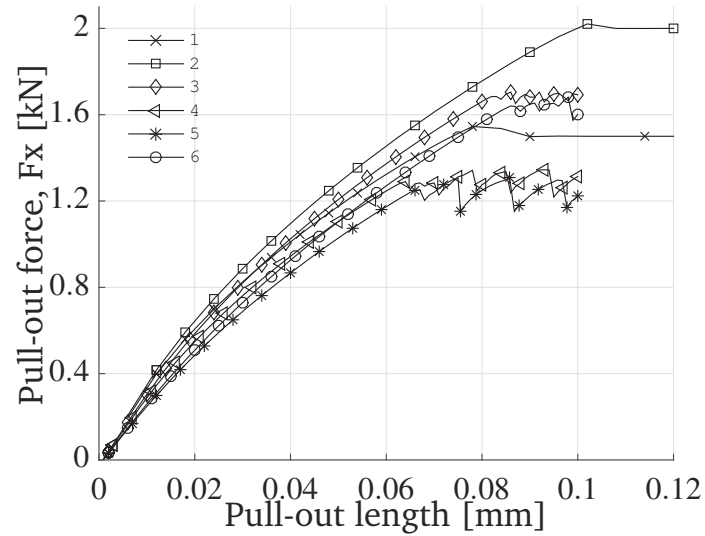
Figure 2.17: Pullout force vs. pullout length. A nominal stress $\sigma_{nom} = 5.33$ MPa is applied to the grips. The pullout length is the displacement applied to the right end of the FRP. The composite did extend on both sides of the grip. μ_{d1} and μ_{d2} were the dynamic coefficients of friction for the two interfaces. The static to dynamic ratio was defined as μ_s/μ_d. 1 - $[\alpha = 90°, \mu_{d1} = 0.20, \mu_{d2} = 0.16, \mu_s/\mu_d = 1.2]$; 2 - $[\alpha = 90°, \mu_d = 0.25, \mu_s/\mu_d = 1]$; 3 - $[\alpha = 70°, \mu_d = 0.25, \mu_s/\mu_d = 1]$; 4 - $[\alpha = 70°, \mu_{d1} = 0.20, \mu_{d2} = 0.16, \mu_s/\mu_d = 1.2]$; 5 - $[\alpha = 50°, \mu_{d1} = 0.20, \mu_{d2} = 0.16, \mu_s/\mu_d = 1.2]$; 6 - $[\alpha = 50°, \mu_d = 0.25, \mu_s/\mu_d = 1]$;

2.6   Paper D: Improved Friction Joint

Paper D contains experimental and finite element analysis results for an improved friction joint. Details of the new setup are shown in Fig. 2.18.
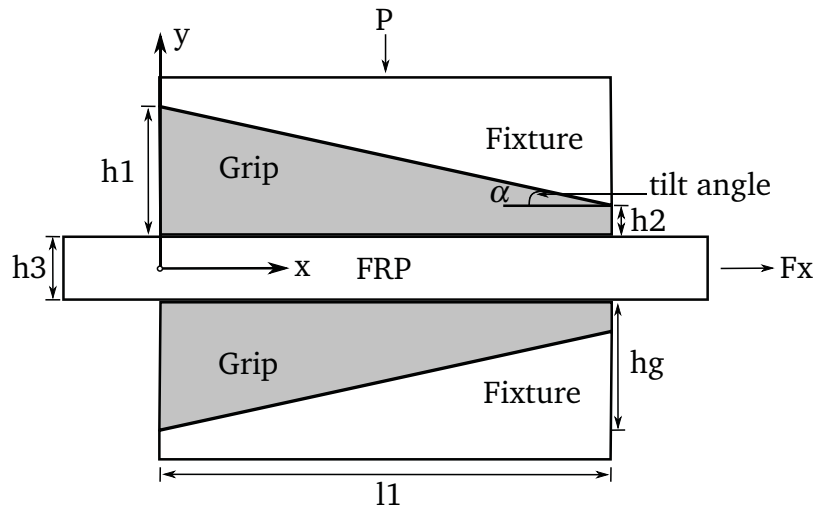

Figure 2.18: Model geometry. The system consists of two v-shaped grips and a unidirectional basalt fiber reinforced polymer in between. The grips are held in a fixture to which pressure is applied. The wide end of the grip has height h1. The narrow end has height h2. Total grip length is l1. The FRP can extend to both sides of the grip. The force Fx is obtained by pulling the FRP in x direction.

The rectangular grips are replaced with a pairs of v-shaped grips. The horizontal surface of the inner grips comes in contact with the FRP tendon. The opposite surface is tilted at an angle $\alpha = 15°$ and comes in contact the second pair of grips. These are housed in between the compression plates of the test rig, and are referred to as the fixture. The system is intended to function in the following way: once the FRP is pulled out, it will engage and pull the grips with it. By being pushed against the fixture, the normal force acting on the composite increases, and keeps the tendon from slipping out. Experimental pullout tests are done using the same procedure as described in Section 2.1. For all results in Fig. 2.19, the FRP extends on both sides of the grip. Two sets of grips are used, one with a smoother surface, and one sandblasted. Lines a1 and b1 show that while all results are pretty linear, it is clear that both F_x and F_x/F_n is higher when using sandblasted grips. Just at low F_n values the grip coefficient is higher in the case of the smoother pair. Line b2 remains almost constant, irrespective of the normal force. In the case of the sandblasted grips, increasing the normal force brings more of the asperities in contact, and F_x/F_n increases. The maximum value of 0.43 corresponds to $F_n = 16$ kN, and is with 26% higher than the result of 0.32, obtained with smooth grips.
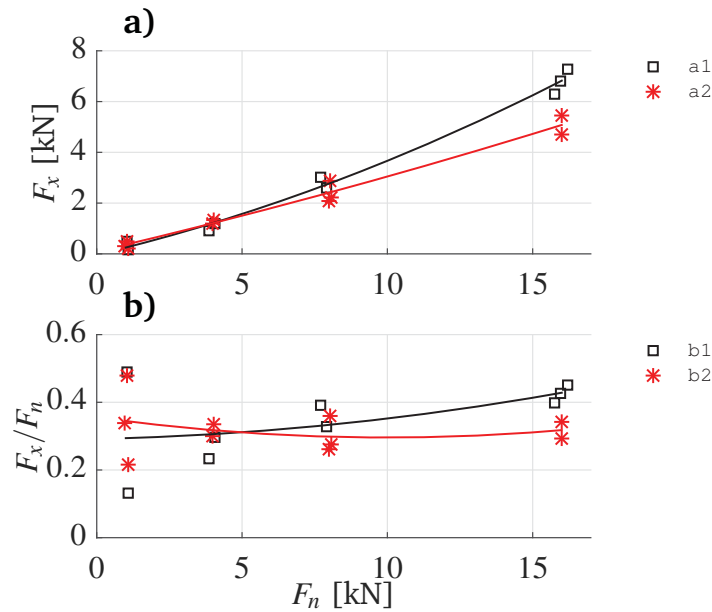
Figure 2.19: Pullout force F_x and grip coefficient F_x/F_n for a normal force $F_n = 1, 4, 8$ and 16 kN. Results using the sandblasted grips are marked with lines a1 and b1. Results using the smooth grips are marked with lines a2 and b2.

Looking at line b2, F_x/F_n is not influenced by F_n because the coefficient of friction at the contact between the grips and the FRP is not high enough to drag the wedges, before pullout occurs. Paper D, Fig. D.4, shows an example in which the grip system works as intended. If the initial value of F_n is high enough, the FRP and grips move together. This results in a small increase of the normal force, which is enough to keep the FRP from slipping. F_x/F_n increases from 0.2 to 0.45. Results in Paper D Fig. D.8 show what happens if the grip system is clamped for longer periods of time. The matrix material does not creep, and the grip efficiency has a value in range with previous results. The main observable difference is the lower result scatter.

A 2D finite element model and analytic results are used for the parametric analysis of the grip system. Taking the force equilibrium in the contact between the grips and FRP, as well as that between the grips and the fixture, it is possible to obtain the maximum tilt angle where the grips retain their intended function. Friction between the grips and the fixture is very important. If the coefficient of friction between the grips and the fixture is low, the reaction force pushes the grips out from the fixture. To counteract this effect, the grip angle α must be reduced. This means that for a certain combination of the coefficients of friction, there is a maximum α value which can be used, so that the grips do not slide backwards.

The FE model presented in Paper B and C is adapted to the new geometry, while using the same material properties. The solution involves two load steps. In the
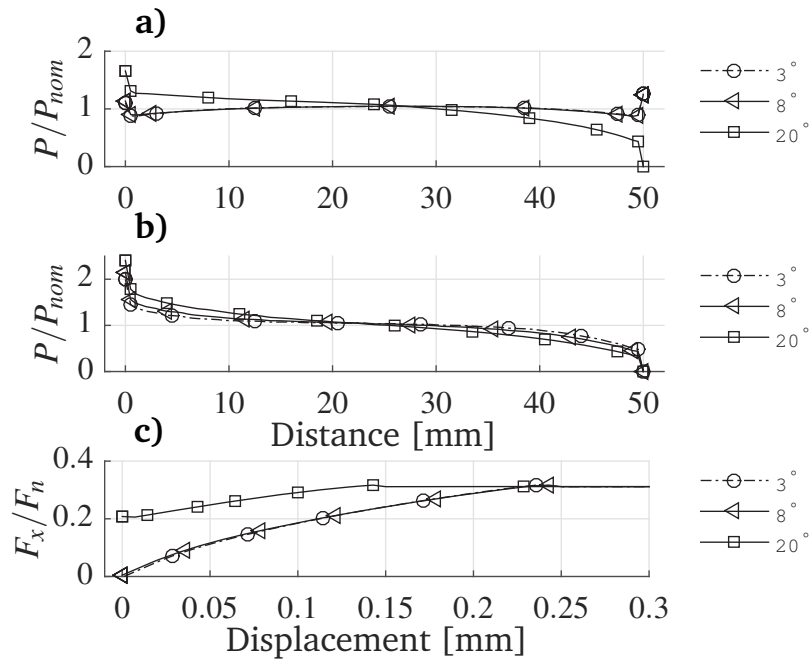
Figure 2.20: Grip angle α effect. Three α values are compared, namely 3°, 8° and 20°. The pressure contact P and the pullout force F_x are normalized with the nominal pressure P_{nom}, and normal force F_n. Two load steps are used. In the first pressure is applied to the fixture, and the contact pressure distribution is given in a. In the second load step, displacement is applied to the right end of the FRP. The pressure distribution just before pullout is given in b. The grip coefficient F_x/F_n is given in c. $\mu_{s1} = 0.25$ and $\mu_{s2} = 0.22$ are used between the grips and the FRP. $\mu_{s3} = 0.3$ is used for the grips sliding against the fixture. The contact area reduction is 20 %. The contact length is 50 mm. $F_n = 16$ kN.

first, a uniformly distributed force is applied to the fixture, to compresses the grips and the FRP. In the second load step, F_x is obtained by applying displacement to the unloaded end of the FRP tendon. A detailed discussion about model calibration using experimental results is presented in Paper D, section D.6.1 and D.6.2. FE results are used in Fig. 2.20 to examine how the contact pressure and pullout force are influenced by α. The normalized contact pressure P/P_{nom} before pullout is shown in Fig. 2.20 a, over the entire contact length. The loaded end of the grip is at the 50 mm mark. At this stage, small values of α do not influence P/P_{nom}. Using a higher value, with $\alpha = 20°$, the P/P_{nom} profile rotation is caused by the backward slide of the grips. During pullout in Fig. 2.20 b, the contact pressure attains the maximum at the 0 mm mark, opposite to load application. With increasing grip angle, more pressure is transferred towards the unloaded end of the grip. During pullout, the maximum force F_x depends on just the friction between the grips and the FRP. For this reason, the maximum value of F_x/F_n in Fig. 2.20 c is constant. When $\alpha = 20°$, the pre-tension of the FRP is caused by the grips sliding out of the fixture. If the

geometry is defined beforehand, the FE model and the analytic solution are used to find the critical values of the friction coefficient , so that the system functions correctly.

Further analysis shows that P/P_{nom} increases towards the unloaded end of the grip, as shown in Fig. 2.20 b, due to a small rotation of the wedges. The boundary conditions used until now intend to replicate what happens in the experimental test rig. Still, it can be possible that a different configuration will be used for an industrial application. Additional stiffening the model is investigated in Paper D. It is obtained by applying boundary conditions on all sides of the fixture, and results in a reduction of the contact pressure, which is shown in Fig. D.16. When the entire test rig is fixed, the maximum F_x/F_n value is half of what is initially obtained.
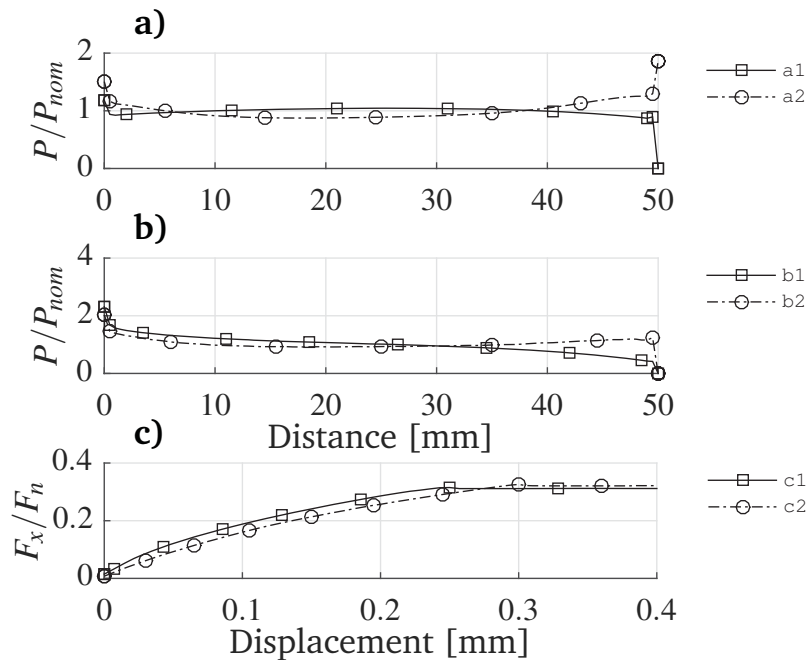

Figure 2.21: Wedge pull. Legend a) After P_{nom} application. Legend b) Before pullout. Boundary conditions line 1: top fixture constrained with $ux = 0$ and $F_n = 4$ kN; line 2: top and bottom fixture constrained in all directions, while displacement is applied to the grips in positive x-direction. For the aluminum to FRP contact $\mu_{s1} = 0.25$, $\mu_{s2} = 0.22$, and contact area reduction is $a = 20\%$. At the grip to fixture contact $\mu_{s2} = 0.3$. The contact length is 50 mm. The grip angle is $\alpha = 15°$.

In the case that the fixture is completely rigid, the contact pressure is generated by displacing the grips in positive x direction. The displacement is controlled so that the same pressure is applied for the two cases in Fig. 2.21. Line number 1 is for the case where pressure is applied to the top grip. Line number 2 is for the completely stiff case. Looking at line a2, P/P_{nom} is higher toward the loaded end of the grip. During pullout, line b2, the pressure profile shifts less when compared with

line a1. It also remains pretty constant over the entire contact area. The maximum grip coefficient F_x/F_n in Fig. 2.21 c is not affected by the loading and boundary case. The displacement necessary to achieve pullout is larger for line c2. This shows that it is possible to use the v-shape grips in different configurations, and retain the same efficiency. Parametric analysis involving α can be used to shift P/P_{nom} from the loaded end towards the back of the grip.

Chapter 3

Conclusions

The goal of this thesis is to develop a simple and reliable method for anchoring flat FRP tendons in metal counterparts. A friction clamp with flat faces is chosen as the preferred solution, and is investigated using a combination of experimental techniques and finite element analysis. The main results of the thesis are summarized in this chapter.
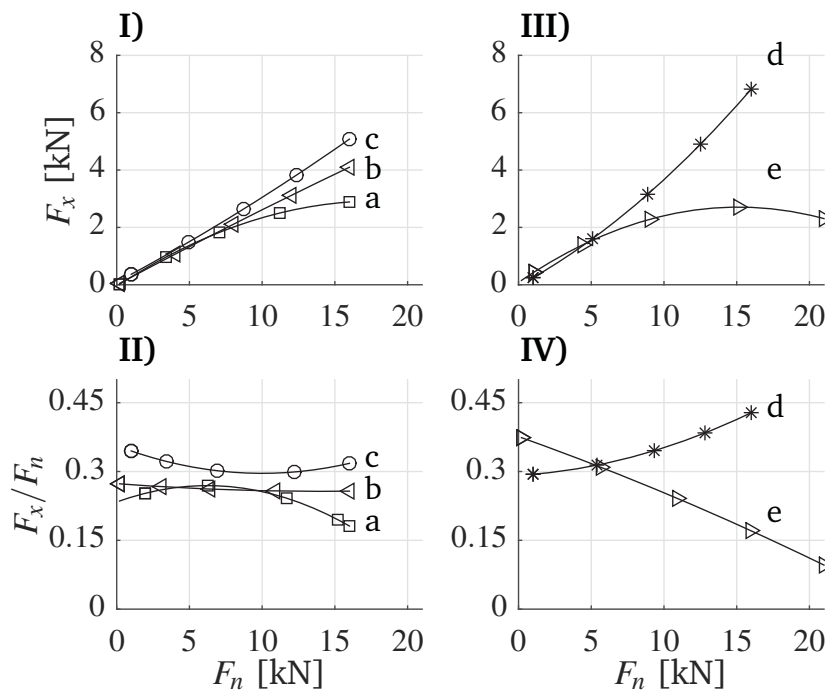

Figure 3.1: Summary of experimental pullout results. Rectangular grips are used for results in lines a,b and e. Lines c and d represent results with the wedge shaped self locking grips. F_x is the pullout force, F_x is the normal force, and F_x/F_n is the grip coefficient.

An important part of the project was to establish a method for making detailed

pullout tests. The major experimental pullout results, as reported in Papers A and D are condensed in Fig. 3.1. Here, it is possible to see the correlation between the pullout force, the normal force and the grip coefficient, which is the ratio between the pullout force and the normal force. Results in Fig. 3.1 I and II, are obtained with smooth grips. The highest pullout force result for smooth grips is obtained with wedge shaped self locking grips, see line c. This solution stands out from the other results, and is more evident with increasing normal force. Results using rectangular grips show a great dependency on the position of the FRP tendon within the grips. If the FRP is extending only on the loaded end of the grip, line b, both pullout force and the grip coefficient are pretty linear . When the FRP extends on both sides of the grips, line a, the pullout force does not increase linearly with the normal force. The grip coefficient in Fig. 3.1 II line a, starts to decrease for high values of the normal force. This shows that the maximum contact area between the grips and the FRP surface is achieved early on, and further increase of the normal force does not result in more contact area. The pullout force can be improved either by increasing the normal force or the contact surface.

Results in Fig. 3.1 III and IV are obtained using sandblasted grips. Looking at line e, the values of the pullout force are similar with results shown by line a. By comparing the grip coefficient for lines a and e, it is shown that the sandblasted grips do create better contact. The grip coefficient at low pullout force values is higher in line e than in line a. This is because the higher asperities can bridge over the micro-roughness of the FRP surface, and achieve better contact. Because large displacements in the contact area are unwanted, the best grip coefficient result is obtained with sandblasted wedge shaped self locking grips, see line d. Two mechanisms contribute to this result. The first is that a better contact is obtained using a rougher grip surface. The second cause is that the grips will slide together with the FRP tendon, which causes an increase in the normal force during pullout, sufficient to improve the grip coefficient.

FE results from Papers B, C and D are presented in Fig. 3.2. These show the contact pressure for the main grip configurations investigated during this thesis. Fig. 3.2 I and III show the normalized contact pressure before pullout, and Fig. 3.2 II and IV show the normalized contact pressure during pullout. In Fig. 3.2 I, there are no major differences between the results obtained using rectangular grips (line a) and those from using wedge shaped self locking grips (line b). But, during pullout in Fig. 3.2 II, there is a larger build-up of pressure for the wedge shaped self locking grips towards the unloaded end. This shows that the superior efficiency of the wedge shaped self locking grips is caused by build-up of pressure in the back of the grip. Tapering the edges of the rectangular grips at an angle is a good way to counteract
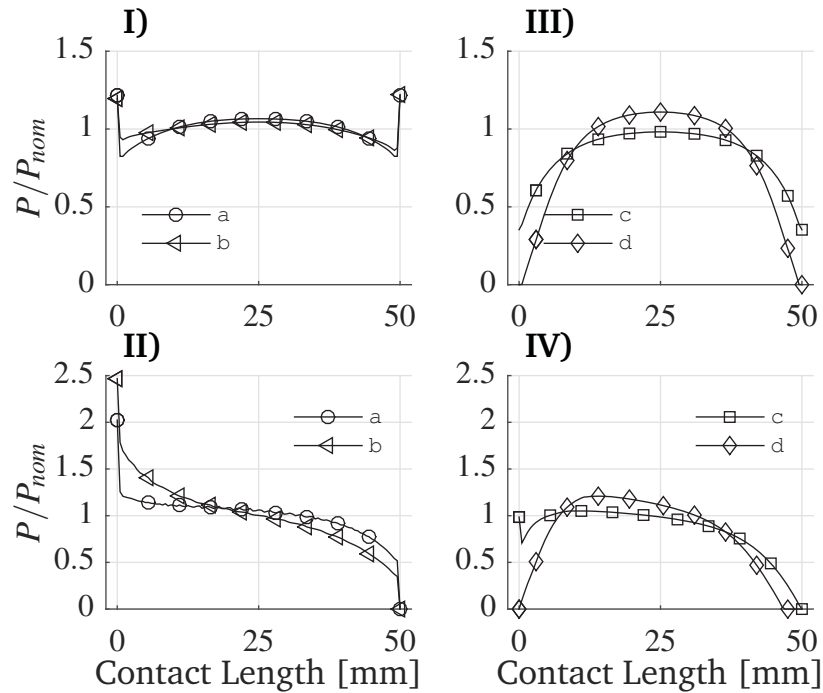
Figure 3.2: Summary of FE pullout results. The contact pressure before pullout is shown in sub-figures I and III. The contact pressure at pullout is shown in sub-figures II and IV. Rectangular grips are used with the following grip angles: 90° (line a), 70° (line c) and 50° (line d). The wedge shaped self locking grips (line b) have a 15° angle. The contact pressure P is normalized with the nominal applied pressure P_{nom}.

edge effects. Results at line c are obtained using a 70° taper angle, and show that the normalized contact pressure does not exceed the value of one in Fig. 3.2 III and IV. This directly relates to their inferior performance, with even lower pullout force obtained for a 70° taper angle.
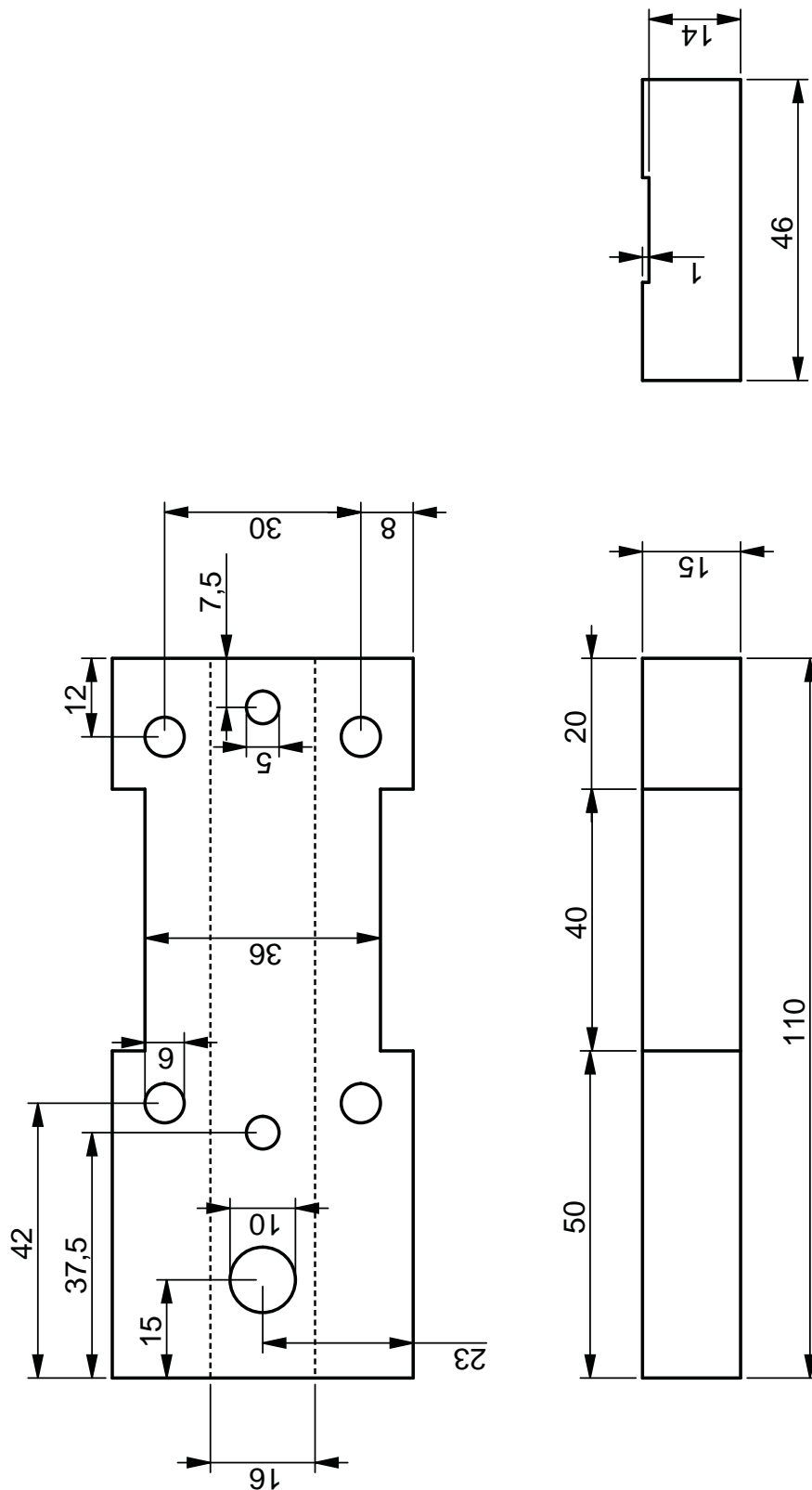
Chapter 4

Supplementary Material

Figure 4.1: Compression steel plates. Two are used to house the grips and to make possible to apply compression to the FRP specimen. A channel is cut in the middle, and it serves to align the grips. Two square washers are installed on each side of the grips to prevent them from displacing. Dimensions in [mm].
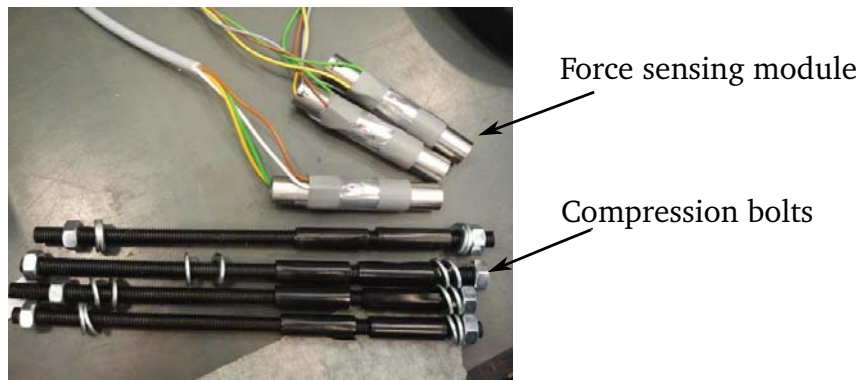
Figure 4.2: Force sensing module. Two strain gages are glued back to back on a steel pipe and calibrated in compression. These are used to apply force to the compression steel plates.
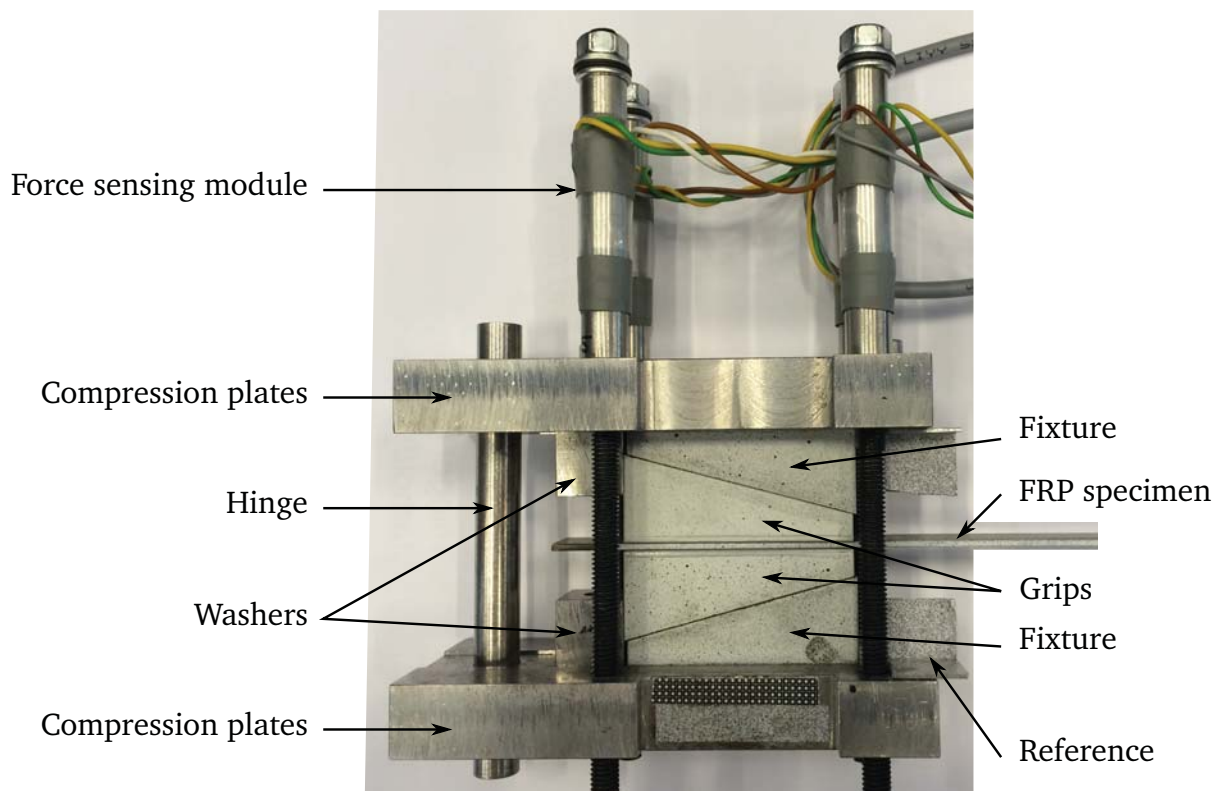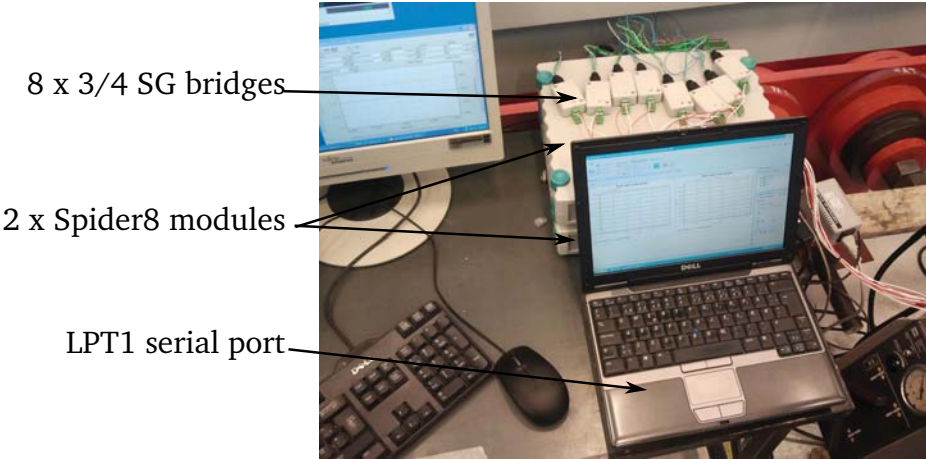

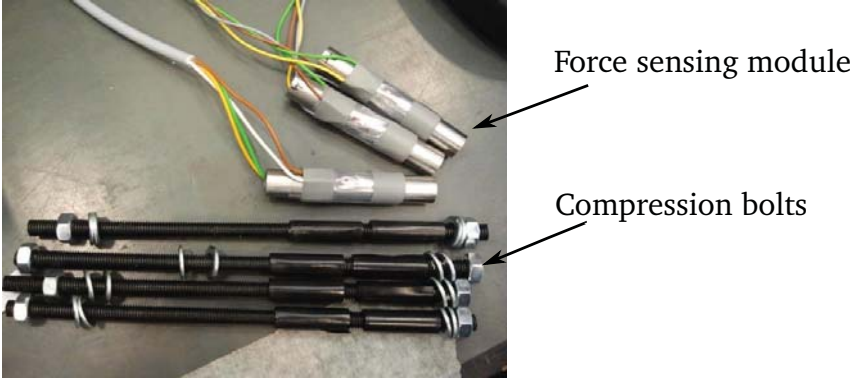**Figure 4.3:** Test-rig featuring all components.

Figure 4.4: Spider 8 setup.
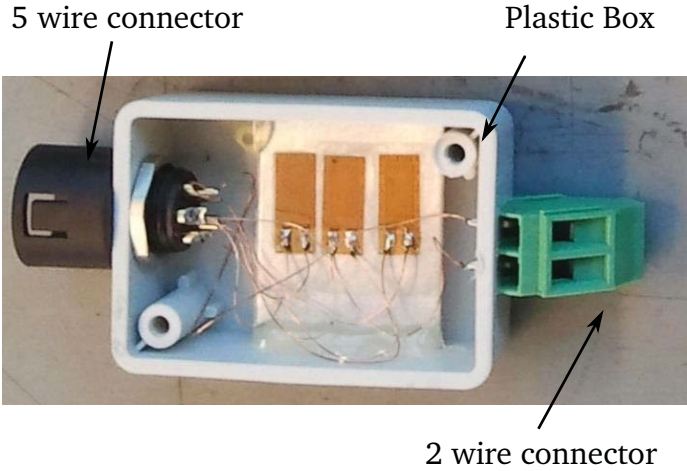

Figure 4.5: Force sensing module.

Figure 4.6: SG tube

Paper A

Friction Joint between Basalt Reinforced Composite and Aluminum

Andrei Costache[1][*], Kristian Glejbøl[2], Ion Marius Sivebæk[1], Christian Berggreen[1]

[1]Department of Mechanical Engineering, Lightweight Structures Group, Technical University of Denmark, Nils Koppels Allé, Building 403, 2800, Kgs. Lyngby, Denmark

[2]National Oilwell Varco, Subsea Production Systems, Priorparken 480, 2605, Brøndby, Denmark

Abstract:
The purpose of this study is to anchor basalt reinforced polymers in an aluminum grip using dry friction. Dry friction clamping is considered the optimal solution for post mounting of load bearing terminations on composite structures. A new test method is presented for characterizing the frictional load transfer behavior of the grip. To carry out the study, a custom built test rig was used to examine the relation between pull-out force and clamping force. The anchoring method was found to be successful. The paper presents details on the custom built test rig, along with the use of digital image correlation for displacement monitoring. Pul-out results and validation tests are presented. In the discussion, the results and the importance of surface finish of the grips for pull-out force is discussed. The discussion was backed by investigations on wear patterns using SEM.

Keywords: Friction Joint; Clamping Force; Basalt Fiber Reinforced Polymer; Coefficient of Friction; Pull-out Force

[*]Principal corresponding author. Tel.: +45 45251391; E-mail: ancos@mek.dtu.dk

A.1   Introduction

Fiber reinforced polymer composites (FRP) are excellent materials for applications where good corrosion resistance and high specific strength or stiffness is needed. Often complex structures require a mix of materials including FRP parts, as well as metal parts. In these cases a reliable mechanical fastening between FRP and metal parts is needed. This study focuses on a method for fastening load bearing FRP tendons in metallic structures. This is a subject of particular importance for the implementation of FRP tendons as primary axial load beading components in flexible unbonded pipes.

Fastening of FRP tendons can be achieved through adhesive bonding, mechanical anchoring or friction-type techniques. Most of the available literature on the anchoring of FRP tendons is related to bridges and power lines [19, 40], whereas the focus of this paper is tendons intended for service in flexible unbonded pipes with large diameter to be used in the off-shore oil industry.

According to the literature [41, 42, 43, 44, 45, 46], the main disadvantages of bonded joints are improper curing of bonding agent, long anchorage lengths, failure due to creep and ill-defined long term performance. Furthermore bonding requires a clean and well controlled environment which makes it hard to realize this type of fastening in an industrial environment or off-shore during repair operations. Thus, not only strength but also practicality dictates the use mechanical fastening in flexible pipes.

In the literature several methods for mechanical fastening has been discussed, such as spike [20], wedge [47], and anchoring of a composite shaft in a metallic hub [48, 22]. These studies show the effect of contact and friction on the pressure variation within a carbon fiber reinforced tendon /metal assembly, as well as the effect of surface treatment of the parts in contact [49]. According to [48] metallic counterparts can be manufactured from different materials, preferably copper or aluminum.

The current study will focus on the anchoring of basalt reinforced polymer (BFRP) tendons in an aluminum grip using dry friction. Aluminum was chosen, partly because of the excellent results obtained in existing literature and partly because aluminum is a readily available material easy to incorporate in flexible pipe structures. The BFRP tendons of interest are produced as thin pultruded strips which have a high surface to thickness ratio and can be stacked on each other to meet the strength requirements of any specific pipe.

A flexible pipe will as a minimum comprise of two helically wound layers each comprising of a multitude of BFRP tendons. These tendons should not be allowed

to slip relative to each other, as this will lead to local strains resulting in localized stress concentrations and ultimately the destruction of the pipe.

Due to geometrical constraints, crimping cannot be used to anchor the strips, instead a double clamp design with flat faces [26] is proposed. This geometry, the interaction of aluminum and BFRP as well as the optimal design of such a joint is not described in the literature [28, 50] and is the focus for this text.

A.2   Materials used

The strips used this study were reinforced with 67 % basalt fibres with a nominal diameter of 16 μm, produced by Techno Basalt. The strips were produced for NOV Flexibles by Vello Nordic AS, Norway, using a proprietary vinylester, see Table A.1.

Tensile strength	88	MPa
Tensile modulus	3,4	GPa
Flex strength	135	MPa
Flex modulus	3,5	GPa
Elongation at break	3–4	%
Heat deflection temperature	140	deg.C.

Table A.1: Vinylester material properties

The strips are 1.5 mm thick, 15 mm wide, and 200 mm long, see Fig.A.1. 50 mm aluminum log tabs are used.
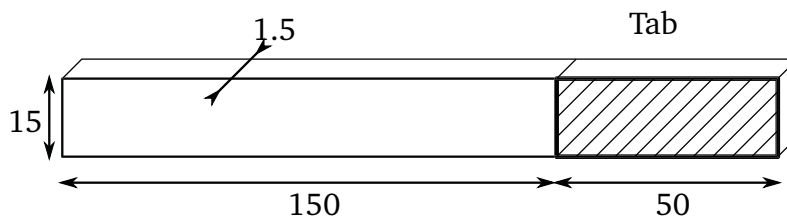

Figure A.1: BFRP specimen dimensions [mm].

A.3   Equipment

To simulate the double wedge system a special test rig was developed, comprising two rigid steel plates clamping around the wedge/strip configuration under investigation, see Fig.A.2. The two steel plates were forced together using 4 bolts each fitted with a load-cell. The load cells were custom made and consisted of a

length of pipe fitted with two strain gauge full bridges. Using these load cells it was simple to continuously monitor the clamping force.
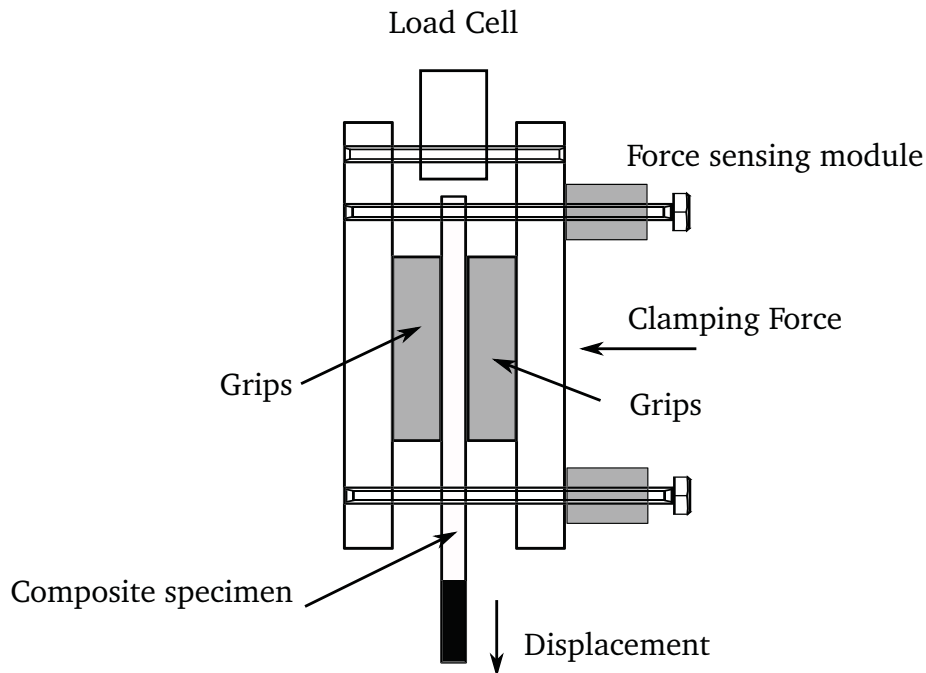

Figure A.2: Test rig for tensile tests. The specimen was placed in the middle between the grips. The clamping force could be controlled via dedicated force sensing modules. The test rig was introduced in this position in the tensile testing machine. Displacement was applied to the lower part of the specimen. The pull-out force was sampled at the load cell on top. Digital image correlation Aramis was used to record strain in the overlap area.

During tests, the clamping force, displacement, pulling force as well as the strain pattern of the strip/wedge assembly was recorded. An image correlation system Aramis with stereo cameras was used to record strain.

For recording the clamping force as well as the load, a Spider8 digital logger was used. The load was measured via the universal tensile machine load cell, and the signal was sent to the digital logger. The digital image correlation system (DIC) and digital logger were triggered simultaneously via a trigger signal from the MTS controller. Thus, all data sets were time synchronized. The same frequency was used to sample data over all systems.

Two sets of grips with different surface roughness were used during testing [**ISO1998b**]. The first set of grips where machined and had an arithmetic mean surface roughness of $Ra = 0.316 \, \mu m$ and a standard deviation of 14.5%. The maximum height of the roughness profile was $Rz = 2.076 \, \mu m$.

The second set of grips were sandblasted and had a mean surface roughness of $Ra = 3.969 \, \mu m$ and a standard deviation of 7.9%. The maximum height of the

roughness profile was $Rz = 24.175\,\mu m$.

A.4   Experimental setup and procedures

Before each test, the specimens and the grips were cleaned with a 50/50 mix of acetone/ethanol to ensure uniform initial conditions. Tests were carried out under normal laboratory conditions i.e. ambient temperature of $20\,^\circ C$.

All tests were carried at a relative velocity between 0.3 and $1.0\,mm/min$. The sampling rate was set to 5 Hz for all systems, sufficiently high to capture the onset of slippage between specimen and clamp.

The initial roughness of the grips had been measured using a profilometer according to ISO standard [**ISO1998b**], using five consecutive repetitions on each surface.
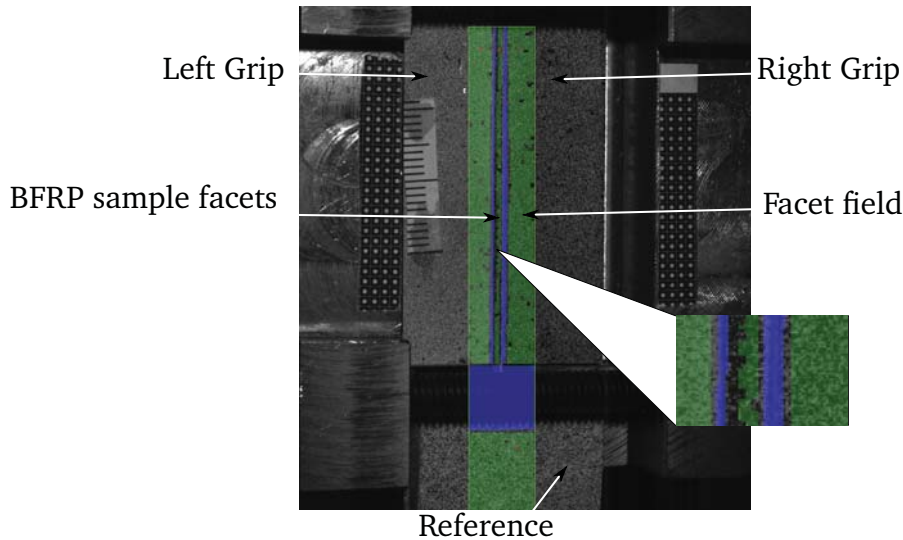

Figure A.3: Aramis facet field (green) over the grips and the specimen. Reference facets are used for movement correction. The magnified selection contains the facet fields (with green) covering the aluminum grips and the BFRP specimen. Blue marks the meshed-out part of the picture.

Prior to measurements the specimen had to be prepared for DIC by painting it with a black and white stochastic pattern, see Fig.A.3. The pattern makes it possible to track the movement and hereby measure strain. Several aspects have to be taken into account when making this pattern. The system operates by defining facets from the stochastic pattern. Although system resolution is $4MP$, the pixels are distributed in a square, thus, only relatively few pixels covers the narrow specimen strip. For accuracy and convergence it is recommended to use above $5X5$ pixels to define a facet. It was only possible to obtain a continuous row of facets 7 pixels wide with an

overlap of 2 pixels along the specimen. Although this is sufficient to measure the displacement of the specimen, the number of facets on the strip does not allow for reconstruction of the strain field over the thickness of the specimen. As specimen and the surrounding wedges move during test, reference facets were created on a surface, fixed directly to the steel supports of the grips. Hence, it was possible to track the relative displacement of the grips and the specimen during tests and eliminate rigid body movement.
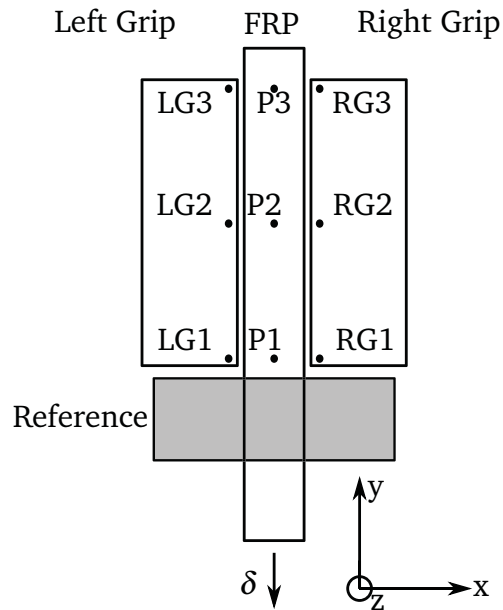

Figure A.4: Aramis stage points. Nine references are taken on the specimen and on the grips, where displacement is calculated. It is possible to track the relative displacement of the specimen to the grips and the overall displacement of the FRP. P3 is the farthermost from displacement application and its movement is the failure criterion for the grip.

To analyze the dynamics of grip failure, specimen displacement values were logged in three points, at three different locations (P1, P2, P3) along the specimen and grips, as shown in Fig.A.4. It was possible to track the relative displacement of the BFRP specimen relative to the grips. Only tests where the BFRP slipped simultaneously from both grips were considered. When used in the field any sliding of the tendons would result in irreversible lengthening and is to be avoided. Hence, zero displacement condition has to be ensured. Consequently, the failure of the grip is considered at the point where the third and farthermost reference point (P3) starts to displace, indicating irreversible lengthening.

Two mechanical configurations, Fig.A.5, were used for the tests. In the first configuration the specimen had the same length as the clamps, Fig.A.5(a). In the second configuration the strip is allowed to extend outside both ends of the clamp, Fig.A.5(b). The clamp was tested at 0.2, 1, 4, 8 and $16\,kN$ clamping force for both

clamp configurations. Five repetitions were done for each force level. A different specimen was used for each load level. Pull-out speeds of 0.3, 0.5, 0.7 and 1 mm/min were used.

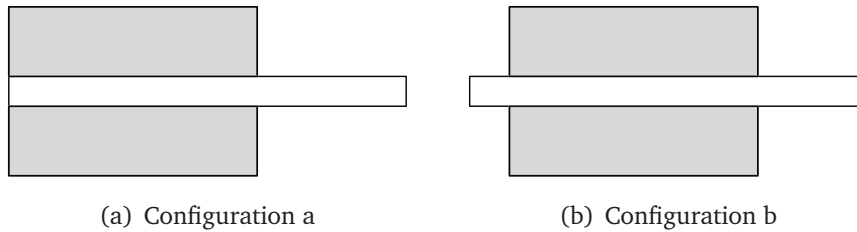(a) Configuration a   (b) Configuration b

Figure A.5: Test configurations showing the BFRP specimen and clamp configuration. In Fig.A.5(a) the specimen does not extend outside of the grips. In Fig.A.5(b) the specimen extends on both sides of the grip.

A.5   Data extraction

Depending on the clamping force, slip may happen either virtually simultaneously at P1, P2 and P3 or in a more sequential manner. P1 is the point closest to load application, and P3 is the point furthest from load application.
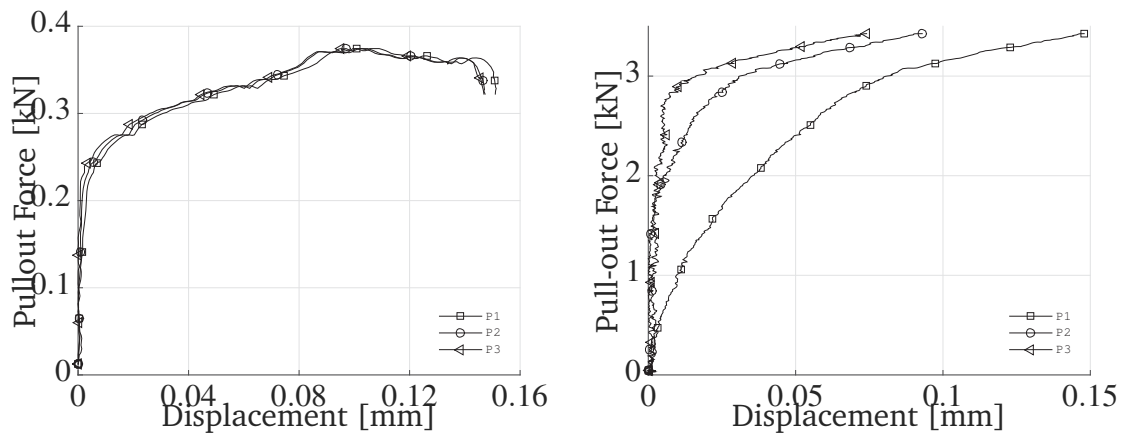
(a) BFRP displacement for tensile test at 1 kN clamping force. Here the specimen slipped simultaneously across the interface.

(b) BFRP displacement for tensile test at 8 kN clamping force. Here the specimen did not slip simultaneously across the interface.

Figure A.6: Pull-out tests and BFRP displacement for different clamping forces.

In Fig.A.6(a) are typical results from a test with a comparably low clamping force. Although it is apparent that the point closest to the pulling end (squared line) moves first and that the point with the longest distance to the pulling end moves last, the displacement of the three points is almost synchronized. Note the drop in force at

a displacement of 0.15 mm indicates rapid slippage across the entire surface. It is hard to pinpoint the transition from static to dynamic friction over the length of the specimen.

In Fig.A.6(b) are typical results from a test with a comparably high clamping force. Note, that there is a clear distinction between movement of the point closest to the pulling end (squared line) and movement of the point far away from the pulling end (triangles line). At $F = 2\,kN$ one notice that P1 has moved $0.03\,mm$ whereas P3 has moved only $0.002\,mm$, indicating that the strip has elongated $0.028\,mm$. Furthermore, it is clear, that the displacement difference between P1 and P2 is significantly higher than between P2 and P3, clearly indicating that the strip is stretched unevenly.

Another worthwhile thing to note from Fig.A.6(b) is, that even after the grip had failed, the pull-out force continues to increase. This is probably caused by the loss of energy in plastic deformation and material transfer between the BFRP and the grips. However, because there is no force drop at failure, this makes it very hard to identify when global failure of the clamp occurs. When the point farthest from load application (P3) slips it is reasonable to believe that slip over the entire length of the strip is eminent. Thus, in the text below global failure is defined when P3 slips.

From Fig.A.6(a)-A.6(b) it is hard to identify with precision the onset of slippage. Instead the data for both P1, P2 and P3 can be plotted in semi logarithmic graphs, as in Fig.A.7 b,c,d. When data is represented in this way, the onset of movement can be readily identified. In the graphs the onset of slip is marked with a black horizontal line. Below the black horizontal line the signal is erratic indicating noise, whereas the signal over the black horizontal line is quite clear and free of noise.

A.6   Validation of method

To validate the system and get a point of reference, the system was tested using strips made from clean polymer material. As benchmark materials homopolymer polypropylene (HPP) and high density polyethylene (HDPE) from Linatex A/S Denmark was tested. HPP and HDPE are considered excellent test materials since they are both polyolefines with an extremely well defined, and comparable chemistry, albeit significantly different coefficients of friction. Attempts were made to test both materials to a clamping force of $16\,kN$, however, due to the low strength of polyethylene, it was possible to test just up to around $8\,kN$ clamping force. The polypropylene has almost double the tensile strength, and it was possible to test up to $16\,kN$.

The results from the reference testing, where global slip is defined as the slip of the furthest point, is presented in Fig.A.8. From the figure a grip coeficient (gc) for
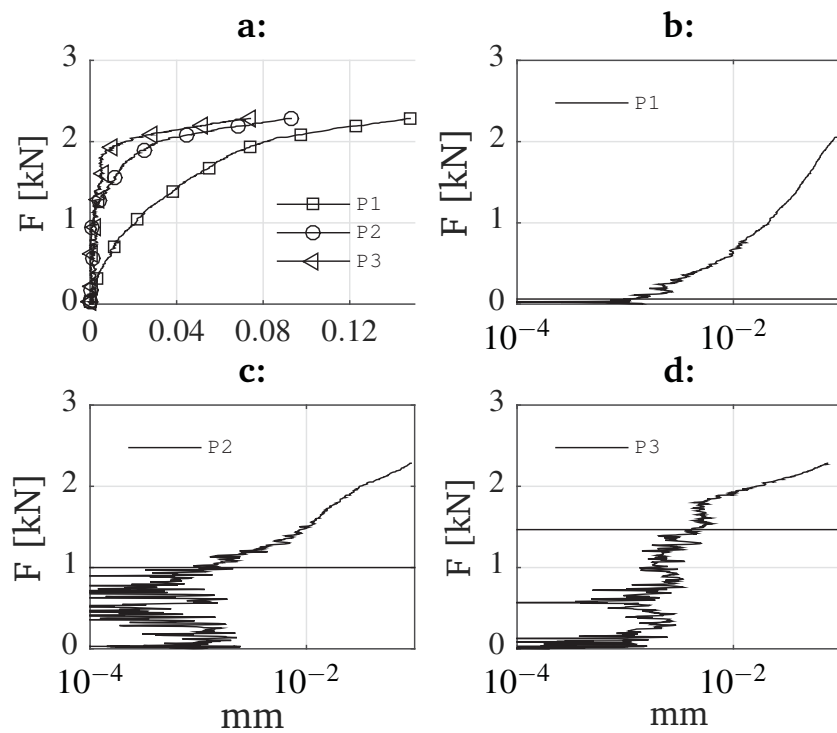
Figure A.7: Pull-out test 8 kN clamping force. The BFRP did extend on both sides of the grip. In the three subplots the logarithmic scale was used to zoom in the initial displacement. P1 is the point closest to force application. P3 is the point furthest from force application. The horizontal line shows the force value at which the BFRP started to slip. The specimen displacement is in [mm].
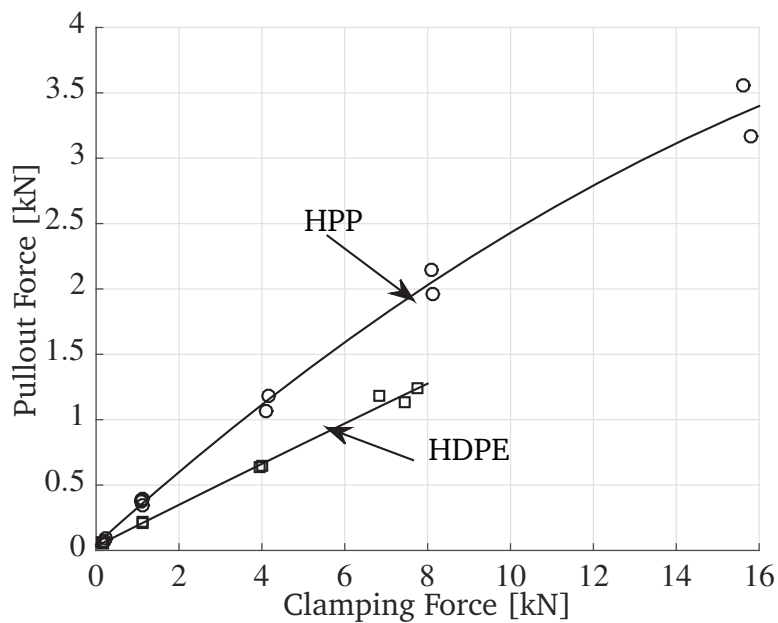

Figure A.8: Polypropylene (HPP) and High Density Polyethylene (HDPE) tensile tests. The specimen did extend on both sides of the grip. The lines are a polynomial fit.

aluminum/HPP and aluminum/HDPE can be derived. The values are gc(alu/HPP) = 0.26 and gc(alu/HDPE) = 0.16.

A.6.1   Coefficient of Friction

The static coefficient of friction (cof) of the BFRP was measured using the smooth grips from the setup, see Fig.A.9. Just one grip had been pressed against a 40 mm BFRP sample by dead weights. This was to avoid edge effects. The grip had been pulled uniformly via a pulley at $1\,mm/min$. The resulting linear fit gave a static cof of 0.25. This result is similar to that obtained for carbon fiber in contact with aluminum [28], where an average of 0.23 was obtained after wear-in. In a second test a coefficient of friction of 0.31 was obtained. This 19% difference could be explained by the different technique used to cut the samples. The lower cof was obtained for samples cut using a wet circular blade with a grit size larger then the basalt fiber diameter. The higher cof was obtained for a finer cut in air.

We can argue that there is a clear influence of the fibers on the cof by comparing the above results with the cof of bulk polypropylene (PP) and high density polyethylene (HDPE). The results of cof PP = 0.22 and cof HDPE = 0.11 are in the range with Bowers [35].
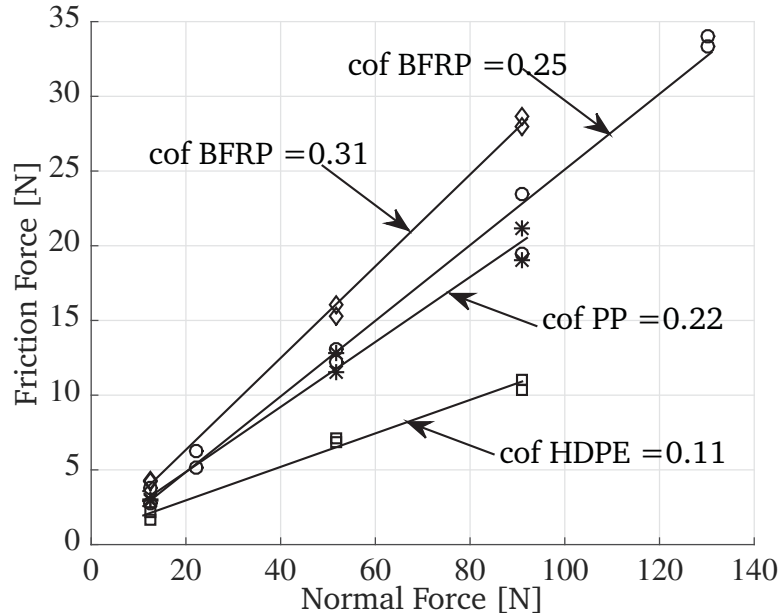

Figure A.9: Friction force vs. normal force. Basalt fiber reinforced polymer (BFRP), polypropylene (PP) and high density polyethylene(HDPE).

A.7   Experimental results and discussion

Fig.A.10 shows the required pulling force to move the furthest point from force application (P3) from the grips. The tests were done using machined surface grips and a clamping force of $0.2, 1, 4, 8$ and $16\,kN$. The figure shows results obtained using two configurations. For Conf. a the specimen did not extend on both sides of the grip, as in Fig.A.5(a). For Conf. b the specimen did extend on both sides of the grip, as in Fig.A.5(b). A different specimen was used for each load level.

Five repetitions were done for each force level. In Fig.A.10 the individual pull-out loads were plotted, together with a line representing the average curve fit.

It is obvious that the pull-out force using Conf. a is both more consistent and higher than that for Conf. b. Analyzing data closer one also realizes that both Conf. a and Conf. b. yields a linear correlation between clamping force and pull-out force from $0.2\,kN$ to $8\,kN$. Up to $16\,kN$ Conf. a maintains the linearity between clamping force and pull-out force, whereas the pull-out force for Conf. b degenerates to a level not much higher than the clamping force obtained for $8\,kN$.
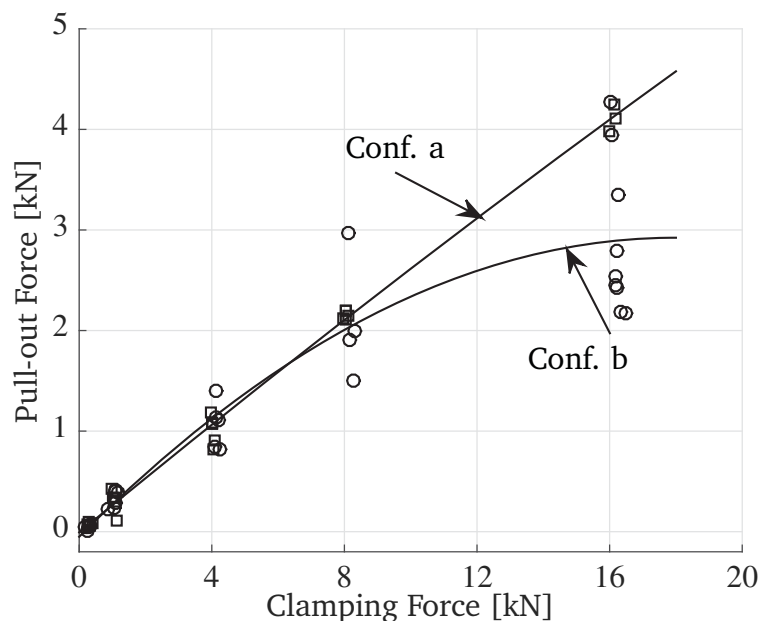
Figure A.10: The required pull-out force to move the furthest point from force application (P3) from the grips. For Conf. a the specimen did not extend on both sides of the grip, Fig.A.5(a). For Conf. b the specimen did extend on both sides of the grip, Fig.A.5(b). The lines are a polynomial fit.

All test results for Conf. contained very little scatter. The grip coefficient for this setup is the ratio of the pull-out force to the clamping force. A nearly constant value of 0.25 is obtained. The value is the same with that of the BFRP coefficient of friction tests in Fig.A.9. Pull-out tests for bulk HPP in Fig.A.8 gave roughly the same grip

coefficient and trend between 0.2 and $8\,kN$. The results diverge for $16\,kN$ clamping force. This is due to the lower elasticity modulus of the bulk HPP samples.

The above results show that the grip coefficient for Conf. a is the same as the coefficient of friction. The system behaved in accordance with dry friction. The friction tests in Fig.A.9 were done with just one contact area. The clamp system has two contact areas. By doubling the apparent contact area no significant variation of the coefficient of friction was obtained.

Because the behavior of the grips and BFRP setup is similar with the behavior of the grips and HPP, it means that the frictional behavior is matrix dominated. No significant variation of the frictional properties is observed, meaning that the fibers have no measurable influence. The contact is matrix to aluminum. Even with wear the scatter remained low. The above is also backed by the very small difference between the HPP and BFRP coefficient of friction in Fig.A.9. The vinylester matrix and the high density polypropylene have basically the same coefficient of friction. The only notable fiber effect is the increase in stiffness, which reduced plastic deformation. It was thus possible to achieve a higher pull-out force.

All results with Conf. b in Fig.A.10 show more scatter. The scatter did increase with clamping force. Larger differences were obtained between tests with the same specimen. When using a new specimen, the lowest pull-out force was obtained for the first test. Then the pull-out increased with subsequent tests with the same specimen. Deviation from linearity starts at $8\,kN$ clamping force. After this value, the pull-out force is no longer proportional to the clamping force. Recent studies have shown that the static coefficient of friction is sensitive to test conditions, especially the angle between the contact surfaces [37]. Due to the specimen extending outside of the grips on the side opposite to pull-out, small rotations could occur. The grips dig themselves in the specimen on the side opposite to force application. This meas that it was not possible to have the exact initial conditions for each test.

Additional tests were done using sandblasted surface grips and a clamping force of $0.2, 1, 4, 8, 12, 15$ and $20\,kN$. Fig.A.11 shows results obtained using one configuration, where the specimen did extend on both sides of the grips. A different specimen was used for each load level.

Marked (SB) are the results for the initial displacement of the furthest point from force application, and marked (SB max) is the absolute maximum pull-out force during the test. At $8\,kN$ clamping force the average pull-out force was SB $= 2.13\,kN$ and SB max$= 5.1\,kN$. At $15\,kN$ clamping force, SB $= 2.7\,kN$ and SB max$= 9.93\,kN$. The correlation between clamping force and pull-out force is almost linear for the SB max values. For the initial displacement, marked SB, the correlation is strongly non-linear. The pull-out force reaches a maximum at $16\,kN$ clamping force, and then
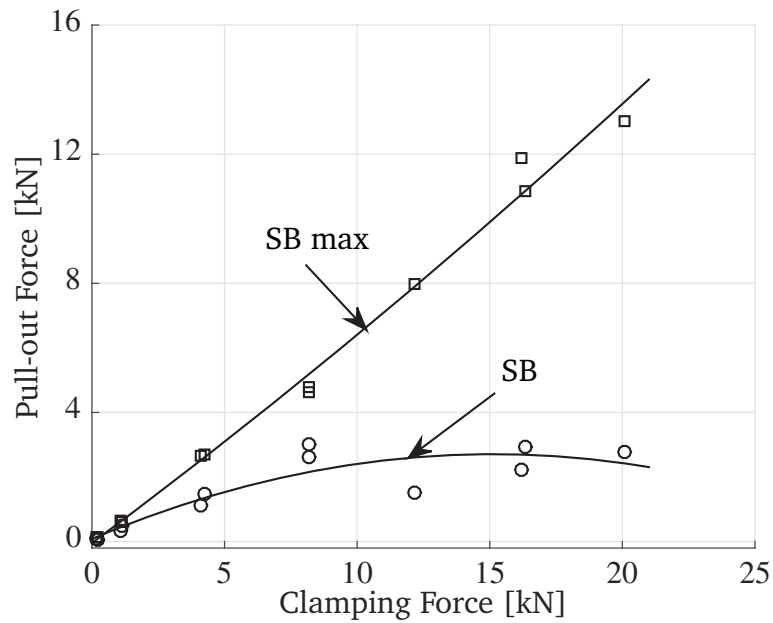
Figure A.11: Tensile tests with sandblasted grips. Marked (SB) are the results for the initial displacement of the furthest point from force application, and marked (SB max) is the absolute maximum pull-out force during the test. The lines are a polynomial fit.

starts to decrease.

Tests in Fig.A.11 show that the maximum pull-out force is significantly higher compared to those of Fig.A.10. Similar improvements due to sandblasting of the grip surfaces have also been reported[51]. The results marked SB in Fig.A.11 are in the same range with those marked Conf. b in Fig.A.10. The pull-out force is not proportional to the clamping force. This stagnation was because the tests had been done immediately after clamping the specimen. It is clear that the contact area did not increase with clamping pressure.

The large pull-out increase for SB max shows that by dragging the grips over the BFRP surface, much better contact was obtained. The deviation between the SB and SB max results is observed for all clamping forces, starting at $1\,kN$. After this value the normal pressure is high enough to make the grips dig into the specimen. Local plastic deformation occurs where the matrix material is picked-up by the grips.

This significant difference between the absolute maximum pull-out force and the load at which the third stage point starts to displace can be seen in Fig.A.12. These values diverge with increasing clamping force. When the grips start to dig into the BFRP, the large asperities make contact with the fibers. When contact was made at fiber level, the pull-out increases dramatically. For a 8 kN tensile test the total displacement to failure was 0.24 mm for P1.

For the results in Fig.A.11 failure load should be considered at 3 kN. However,
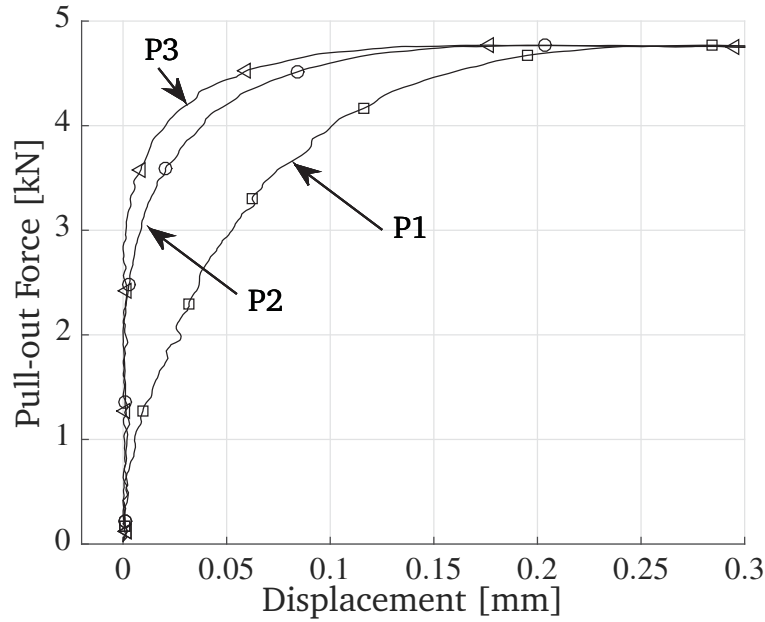
Figure A.12: Tensile test 8 kN clamping force, sandblasted grips. The initial displacement of all reference points is below the maximum pull-out force. P3 is the point furthest from force application.

the pull-out force increased up to 4.77. The maximum pull-out force was obtained with after a 0.2 mm total displacement of the BFRP in the grips.

The effects of test speed and number of repetitions with the same specimen on pull-out force are shown in Fig.A.13. The specimen did extend on both sides of the grip, and a clamping force of $16\,kN$ was used. Two specimens were tested, one for 3 pull-out tests and one for 5.

Specimen number (1) was tested at $0.7\,mm/min$. The pull-out force increased with subsequent repetitions, even if the clamping force at the moment of the test was almost constant. This is a clear indication that wear increases the coefficient of friction. Looking at the results specimen number (2) it is not clear if the test speed has any influence at all. The first results (2.1), at a test speed of $0.3\,mm/min$ give very close values, at $2.4\,kN$. Increasing the pull-out speed to $0.5\,mm/min$ results in two values (2.2), with a 29% difference. Further increasing the test speed to $0.7\,mm/min$ yields a lower spread of 13.8%. It can be said that the (2.1),(2.2) and (2.3) results in Fig.A.13 are roughly distributed around a $2.4\,kN$ mean. No significant influence of the test speed was observed.

A.7.1   Wear mechanisms

Wear of the BFRP surface in this study is an important measure of the amount of damage sustained after pull-out. Because of the size and weight of the specimens,
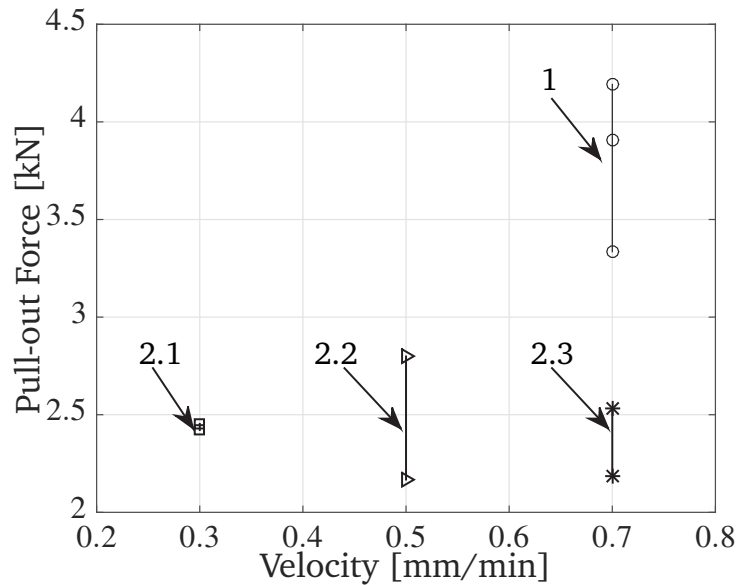
Figure A.13: Influence of the test speed on pull-out force. The clamping force is $\approx 16\,kN$. The same specimen and test speed was used for test (1). A different specimen was tested at three different speeds in (2.1), (2.2) and (2.3).

mass reduction as a result of material transfer is unmeasurable. But because localized damage in unidirectional composites can lead to premature failure, any surface modification is important. For better understanding the surface contact, the middle and the edges of the sample were compared. One specimen was in contact with the smooth grips, and one was in contact with sandblasted grips.
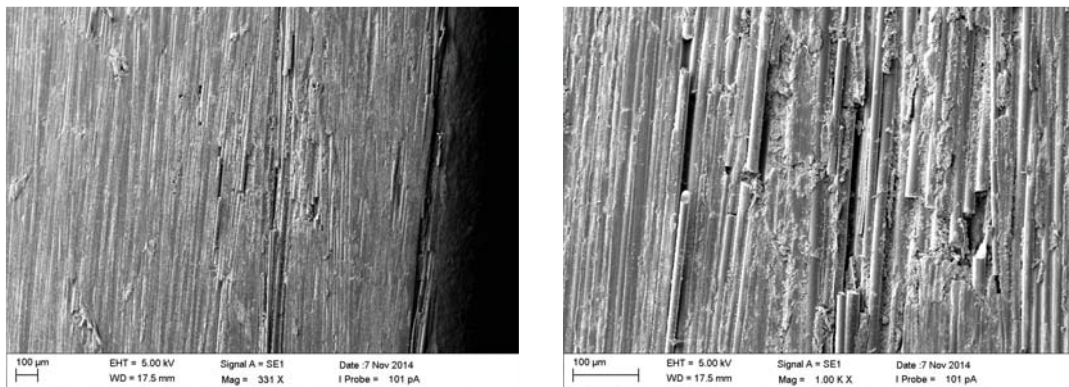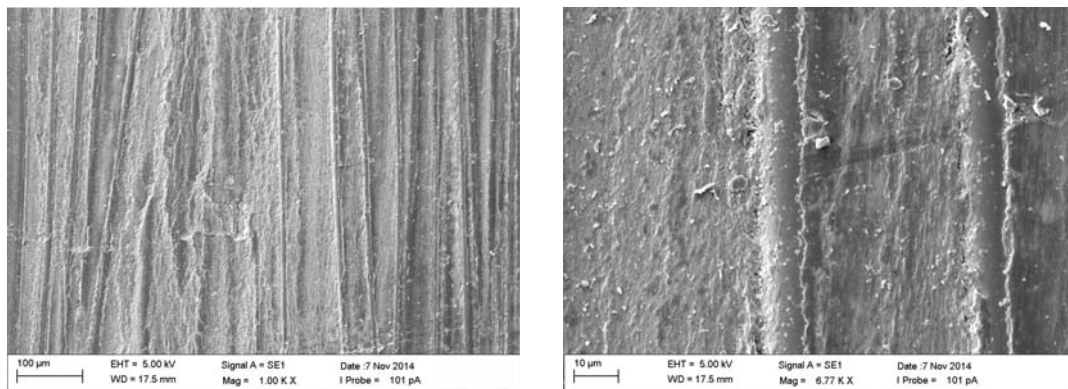

(a) Worn surface from the edge of the BFRP sample.

(b) Detail of the worn surface at the edge of the BFRP sample.

Figure A.14: Wear pattern at the edge of the sample in contact with smooth grips.

The specimen in Fig.A.14 was tested five times at a clamping force of 8 kN with the smooth grips. Scarring was concentrated at the edge, with some areas

more damaged then the others. Matrix material was removed from the surface and transfered to the grips. This result also explained why the first test with a new specimen always gave the lowest pull-out force. Once the fibers were exposed, larger scar marks had developed. A zoom at the largest damage in Fig.A.14(a) is shown in Fig.A.14(b). Here the damage was in-depth with missing and broken fibers. A lot of matrix was also removed. Wear caused delamination and fiber breakage. There was no evidence that the broken fibers had caused more damage as they were pulled over the surface.

In Fig.A.15 the center of the specimen appears mostly undamaged. Further zooming in, it is possible to see, that the matrix had been shaved from the top of the outermost fibers. This is very localized, indicating that limited contact took place here. No fibers had been broken. If sustained by the matrix, the fibers did not break. It appears that only when exposed from the matrix, and due to increased shear on their surface, the fibers break locally and are picked up by the grips. The non-uniform damage distribution between the edges and the middle of the specimen is a clear indicator of the unevenness of the surface.
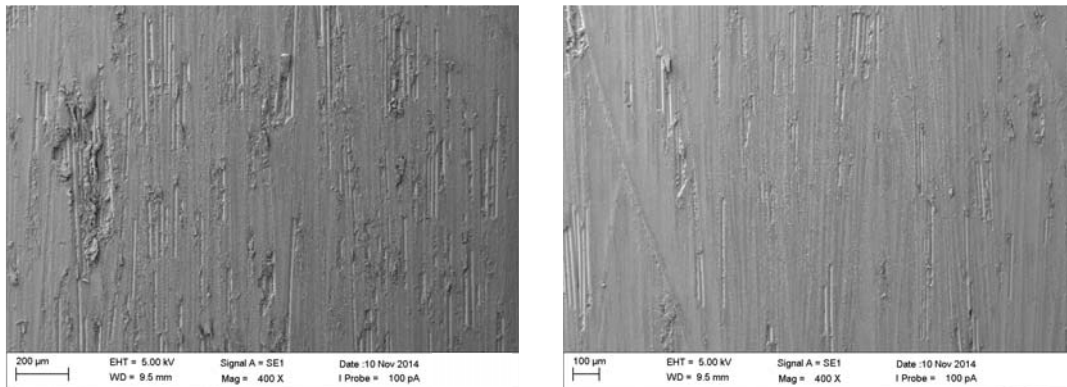

(a) Worn surface at the center of the BFRP sample.

(b) Detail of the worn surface at the center of the BFRP sample.

Figure A.15: Wear pattern at the center of the sample in contact with smooth grips.

The specimen in Fig.A.16 had been tested at 12 kN clamping force just once using sandblasted grips. In Fig.A.16 the average scar marks are larger, and more numerous at the edge of the specimen, when compared to results in Fig.A.14(a). They are less deep and the fibers are not broken. In Fig.A.16 the scars correspond to the highs of the profile, and the marks have been done by digging in and dragging the matrix material off the fibers. In many cases the material is still attached to the surface. One good result is that the fibers are not broken, which makes less probable the development of larger damage under cyclic loading. The damage was evenly distributed over the apparent contact area. When compared to results in Fig.A.14(b),

no large, deep, scar marks were present.

(a) Sandblasted grips; worn surface at the edge of the BFRP sample.

(b) Sandblasted grips; worn surface at the center of the BFRP sample.

Figure A.16: Wear pattern for contact with sandblasted grips.

In the center of the specimen, seen in Fig.A.16(b), several scar marks can be seen. They are less numerous than towards the edges, see Fig.A.16(a). This shoes that there is better contact between the grips and the sample across the entire surface. One reason could be that the sandblasted peaks are high enough to bridge over the valleys in the center of the specimen. Again, there are no broken fibers.

A.8   Conclusions

Pull-out tests of a composite to metal grip showed that it is possible to reliably anchor FRP using dry friction. Extensive tests have shown the relation between clamping force and pull-out force, using a wide range of parameters. It was found that the clamp setup is very sensitive to initial conditions. If the specimen was extending on just one side of the grip, the pull-out force to clamping force ratio did agree with Coulomb's law. For the setup where the composite extended on both sides of the clamp, a very large scatter was observed, together with a deviation of the friction law towards high clamping forces. The behavior of the grip system is dominated by polymer to aluminum friction. Comparing pull-out tests between bulk polymers and basalt fiber reinforced polymer no significant fiber influence was found. The pull-out to normal force ratio was in good agreement with the coefficient of friction measured for the same material pair. No significant correlation was found between pull-out speed and the static coefficient of friction. For application purposes, the sandblasted grips are better, giving superior pull-out force and less severe damage, when compared with flat grips. It is important to make direct contact with the fibers, as this improved force transmission between the aluminum

and BFRP. From this study it is possible to select the optimal clamp configuration and to estimate it's frictional behavior.

Acknowledgments

Paper B

Numerical Investigation of Friction Joint between Basalt Fiber Reinforced Composites and Aluminum

Andrei Costache[1][*], Kristian Glejbøl[2], Ion Marius Sivebæk[1], Christian Berggreen[1]

[1]Department of Mechanical Engineering, Lightweight Structures Group, Technical University of Denmark, Nils Koppels Allé, Building 403, 2800, Kgs. Lyngby, Denmark

[2]National Oilwell Varco, Subsea Production Systems, Priorparken 480, 2605, Brøndby, Denmark

Abstract:
Flexible risers are a type of pipe used to connect sub-sea oil wells to production and drilling equipment at the sea surface. The latest research in unbonded flexible pipes looks at reducing weight by introducing composite materials instead of steel. Lighter and stiffer pipes are designed for ultra deep water applications. The scope of this paper is to develop a new finite element model used for evaluating the efficiency of anchoring flat fiber reinforced tendons using dry friction. The model consists of a double grip system with two flat grips. This is used to squeeze a unidirectional basalt fiber reinforced tendon. The novelty of the paper consists in a detailed investigation of the relation between the coefficient of friction and the pullout force. By comparing numerical and experimentally obtained results, it is possible to show the importance of friction decay in the grip. Improper contact between the grips and the composite is taken into account. Good agreement is achieved between numerical and experimental results. This study shows how to avoid over-estimating

[*]Principal corresponding author. Tel.: +45 45251391; E-mail: ancos@mek.dtu.dk

the efficiency of a double grip to fiber reinforced polymer clamp, and how to use contact dry friction contact in finite element models.

Keywords: Friction Joint; Clamping Force; Fiber Reinforced Polymer; Coefficient of Friction; Pullout Force

B.1 Introduction

Flexible risers are a specific type of pipe used in the offshore oil industry. They serve as the connection between the subsea facilities and the production and drilling equipment at the sea surface. Flexible risers can be used for extraction and injection. During extraction, oil or gas are transported from the sea-floor to the sea surface. Ultra deep water drilling is now taking place for depths in excess of 1500 m. If the exploitation takes place at smaller oilfields, or in ultra deep water, it is best to use floating facilities. These are ships which move laterally and vertically with the waves.
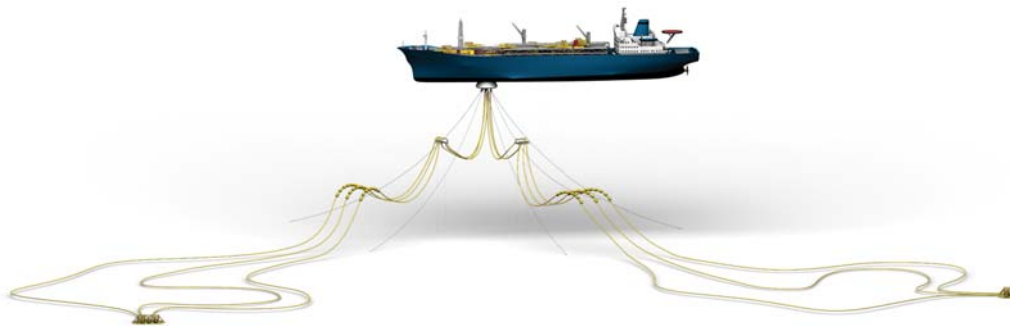

Figure B.1: FPSO and flexible pipe connection.

Flexible risers are ideal for accommodating the relative movement of these FPSOs. They are designed to withstand a multitude of dynamic load cases, which include cyclic tension, compression and bending. The main limitation of these systems is their ability to withstand tensile loads. These are caused by their own weight, coupled with the vertical rise and fall of the floating facility.

Going to ultra-deep water forced the industry to look into using composite materials instead of steel. These risers consist of several concentric layers, each having a dedicated purpose. Steel was used in all structural layers, while polymers are used as permeation and protection barriers. More recent designs intend to reduce the weight of the pipes by replacing the pressure armor [52], or the tensile armor with composite materials. In some cases glass fiber reinforcement tapes are used as reinforcement between two extruded layers [53]. A prominent example

of unbonded flexible pipe design is the Flextreme$^{\text{TM}}$ concept [17]. It consists of only three concentric layers. The inner layer resists the outside pressure, the center layer resists the internal pipe pressure, and the CFRP armor gives the pipe its tensile strength.
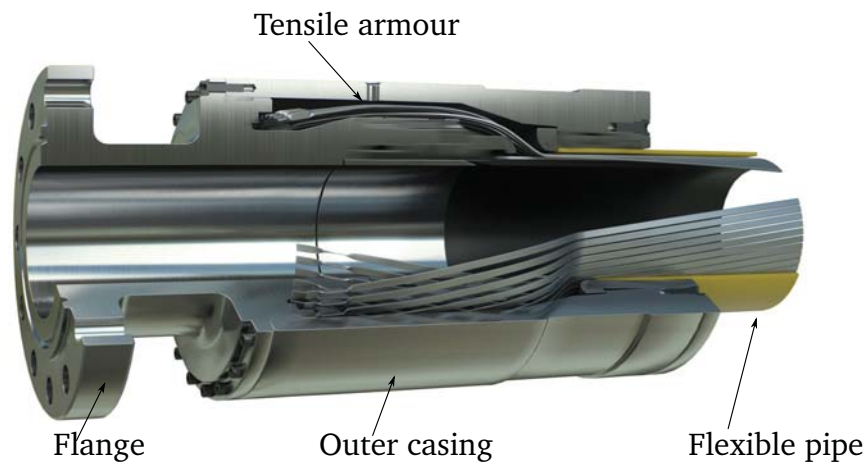

Figure B.2: Typical end-fitting for unbonded flexible pipes. The tensile armor wires give the pipe its tensile strength. They terminate in the end-fitting, and have to be anchored in order to transfer loads from the pipe to the flange. The anchoring method is critical for the structural integrity of the pipe/end-fitting assembly.

This tensile armor consists of two helically wound layers. The optimal shape of the tensile wires is rectangular, in order to stack the maximum amount of material in a reduced space. The wires terminate in the end-fitting, and have be anchored individually, see Fig. B.2.

Anchoring a flat fiber reinforced specimen is a less researched topic, since initial effort concentrated on gripping circular tendons. Prestressing carbon fiber reinforced tendons is investigated both experimentally [22], as well as numerically [54], using different configurations [19]. Adhesive bonding was used initially for anchoring rectangular strips [18]. The first study into frictional anchoring of strips used a barrel and wedge design [27], and focused on minimizing the stresses in the composite. More advanced profiles were developed since [55].

There are several reasons for using friction instead of adhesion: the clamp can be taken apart with ease for repairs; there is no need to use adhesives or to verify the curing process; and the contact pressure can be controlled by changing the length of the grips.

This research wants to create a realistic finite element model for a friction clamp between a flat fiber reinforced polymer tendon and aluminum grips. This model is used to estimate the pull-out force required to move the FRP from the grips for several clamping pressures. All previous studies assume a coefficient of friction μ

taken from literature, and do not vary the normal force in the grip. It is necessary to check what is the influence of the coefficient of friction and to compare the pullout force with experimental data. A 2D finite element model is created, with contact between both grips and the FRP.

B.2 Finite element model

The purpose of this model is to make a detailed investigation of the relation between the coefficient of friction and the friction force at the contact between a metal clamp and the FRP material.
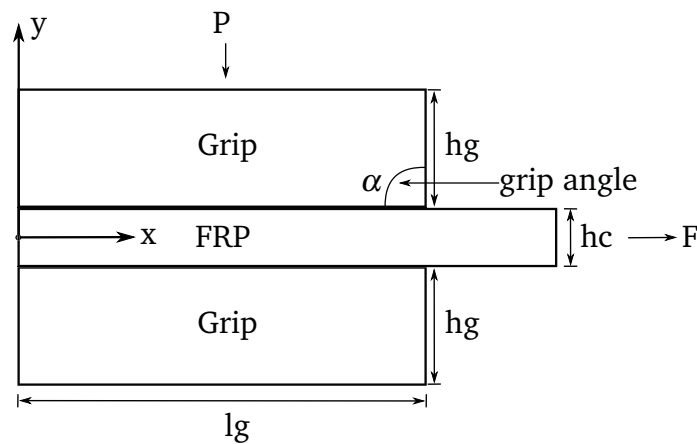

Figure B.3: Model geometry. The system consists of two grips and a unidirectional basalt fiber reinforced polymer in between. The grips have length lg, and height hg. The FRP is extending beyond the right end on the grips, and has the thickness hc. A clamping pressure P is applied to the top grip. The friction force F is obtained by pulling the FRP in x direction.

The full friction clamp model consists of two aluminum grips and a unidirectional basalt fiber reinforced polymer squeezed in between. The grips are pressed against the FRP with a pressure P, and the friction force F is developed when pulling out the right end of the composite.

The origin of the coordinate system for the entire model is located to the left side. The x-axis running horizontally, and the y-axis is in vertical direction, as shown in Fig. B.3. The grips have a rectangular shape, with length $l_g = 50$ mm, and height $h_g = 15$ mm. The angle between the vertical faces of the grips and the FRP is $\alpha = 90°$. The composite is thin compared to the grips, with thickness $h_c = 1.5$ mm, and extends to the right side of the grips.

The 2D finite element model in Fig.B.4 is built in Ansys 15.0, using a 2D 8-node solid element. A plane stress with thickness definition is used. To keep the size of the model to a minimum, and to have good accuracy where the corners of the grips

come in contact with the FRP, the finite element mesh is more dense towards the corners of the grip. The same line division ratio is used in both the grips and the FRP. This ensures that the solid element nodes are in perfect initial overlap. Because contact is nonlinear, a nonlinear solver which includes large geometrical effects is used.
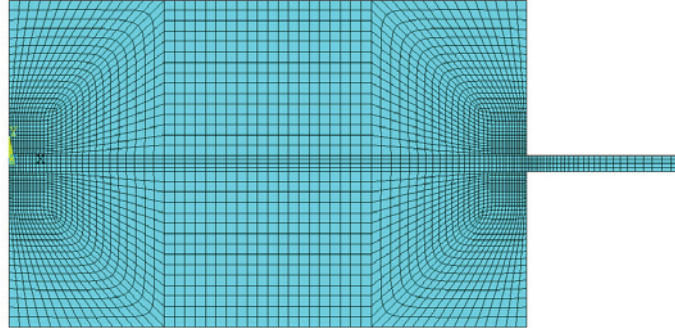

Figure B.4: Finite element model of the grips and FRP. A full model is built instead of a 1/2 symmetric model. This allows to have two contact areas. In each contact area it is possible to define a coefficient of friction μ. The top grip is allowed to move in y direction. The bottom grip is constrained in all directions. The grip angle is $\alpha = 90°$.

Solving this problem includes two load steps. The boundary conditions for the first load step imply constraining the top line of the top grip against movement in x direction. The grip is allowed to slide vertically, and pressure is applied uniformly at the top line. The lower grip is constrained in all directions at the line opposite the FRP. The nodes at the right end of the FRP have a coupled degree of freedom. In the second load step, displacement is applied to the master mode of the coupled DOF.

The two contact areas between the grips and the FRP were modeled with 2D 3-node surface-to-surface contact elements. The FRP, which is more deformable, is the contact surface. The target surface is defined on the grips. CONTA172 and TARGE169 contact elements are generated on top of the solid elements. The contact pair is generated automatically by the software, which matches the nodes that are at the same position. The initial contact status is closed, and effects of initial interpenetration are excluded. Contact detection is set at the nodes. A value of 0.1 is used for the normal penalty stiffness factor. The value is recommended in the user manual for contact pairs which have greatly different stiffnesses.

A specific coefficient of friction is used in each contact surface. Because the FRP is unidirectional, an isotropic friction model is used. Experimental tests have shown that the coefficient of friction between aluminum and vinylester reinforced basalt fiber is between 0.25 and 0.35 [1] in longitudinal direction. When contact status changes from stick to slip, there is a drop from the static coefficient of friction μ_s, to

the dynamic coefficient of friction μ_d. This behavior can be modeled using a ratio μ_s/μ_d between the static and dynamic coefficients of friction.

The grips are modeled as isotropic materials, with $E_x = 69$ GPa and $\nu_{xy} = 0.33$ for aluminum. The FRP is modeled as an orthotropic material. Transverse elastic modulus $E_y = 9.51$ GPa is calculated for the FRP. This is done using a micro-mechanics approach based on fiber volume fraction and material properties of the fibers and matrix provided by the manufacturer. The shear modulus in principal direction is $G_{xy} = G_{xz} = 6.23$ GPa, and the transverse shear modulus is $G_{yz} = 2.59$ GPa. The major Poisson's ratios are $\nu_{xy} = \nu_{xz} = 0.29$ and the minor Poisson's ratio is $\nu_{yz} = 0.32$. Five longitudinal tensile tests have resulted in a longitudinal elastic modulus $E_x = 41.88$ GPa.

B.3   Model validation

The relative sliding between the surfaces in contact generates contact friction stresses for each contact node pair. This stress acts tangential to the surface and is proportional to μ times the contact pressure. It is necessary to achieve a stable solution for the pressure distribution in the contact area between grip and FRP, while at the same time keeping the size of the model at a minimum.
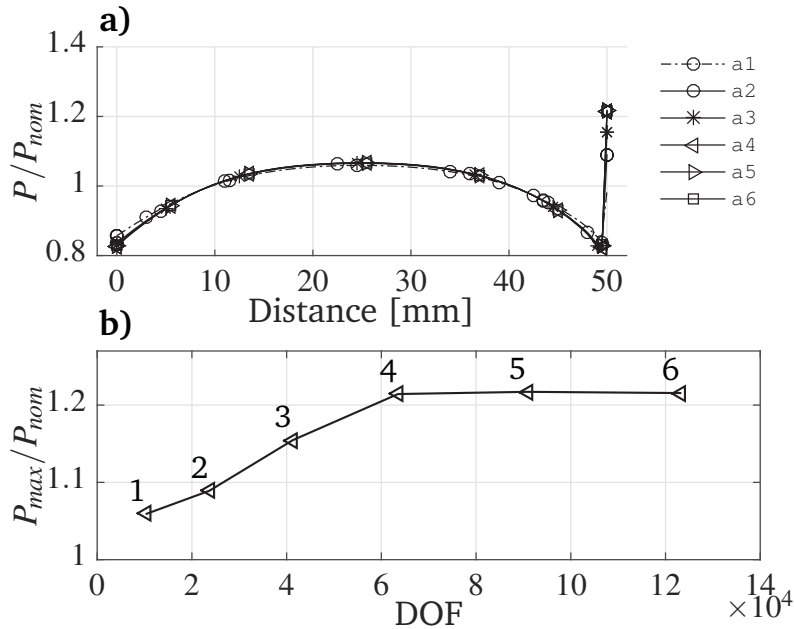

Figure B.5: Pressure distribution at the contact between the grips and the FRP. Legends a1 to a6 correspond to increasingly finer meshes, from 10^4 DOF to $12 * 10^4$ DOF. The pressure P and the maximum pressure P_{max} are normalized with the nominal applied pressure P_{nom}. The contact length is 50 mm. A coefficient of friction $\mu = 0.25$ is applied for both contact areas.

For the results in Fig. B.5, the length of the grips is 50 mm and the FRP tendon extends with 12 mm to the right side of the grips. A uniformly distributed pressure of 5.33 MPa is applied to the top grip, and the bottom grip is constrained from displacing in all directions. The static and dynamic coefficients of friction in both contact areas are $\mu = 0.25$. Because contact is nonlinear, the normal force is applied in 5 load steps, to achieve convergence. The contact pressure distribution in Fig. B.5 a is obtained using six different mesh densities. Line a1 corresponds to the coarsest mesh, with 10446 degrees of freedom. Lines a2 to a5 represent increasingly refined meshes. The most refined mesh, with 123118 DOF, is represented by line a6. The contact pressure achieves a maximum value at the right end of the grip, due to the increased stress at the corner. There are some differences in the pressure profiles for different discretizations. For the coarsest mesh, line a1, the distribution is less convex. With increasing DOF the differences become almost inexistent.

The DOF has it's biggest effect over the maximum pressure at the corner. By plotting the normalized pressure value versus mesh density in Fig. B.5 b, the trend becomes clear. The maximum value increases almost linearly from a value of 1.05 to a value of 1.21 obtained for a mesh density of $6.3 * 10^4$ DOF. Increasing the DOF further does result in a constant pressure ratio. To keep the model size at a minimum, a mesh density of $6.3 * 10^4$ DOF is used in all subsequent calculations.

The pull-out force is the resultant of contact friction stresses at each node pair. The friction stress is proportional to the contact pressure times the coefficient of friction. The contact pressure profile during pullout is shown in Fig. B.6. In this case a displacement of 0.1 mm is applied to the right end of the FRP. Due to axial elongation of the composite, coupled with lateral contraction, the contact pressure starts to decrease at the right end of the grip, as shown in Fig. B.6 a. This unbalanced pressure distribution is compensated by an increase at the unloaded end, where the FRP is still not moving. The contact sliding distance is given in Fig. B.6 c. It shows that at the left end of the grip there is no movement, while at the loaded end a maximum sliding of 0.06 mm has occurred. From Fig. B.6 b it is clear that the contact friction stress is proportional to the normalized contact pressure times μ. There are no significant differences between results in lines 1 and 2, which means that the DOFs have no significant influence over the pullout force. The most important observation which can be made from Fig. B.6 is that the transition from stick to slip happens in a progressive manner along the contact area. Because the contact pressure is relatively low, the contact status changes from stick to slip when the pullout force exceeds the static shear stress. It is not necessary to set a maximum equivalent static shear stress value to ensure transition to the dynamic regime, as it happens in bulk forming processes. There the contact shear stress can exceed the
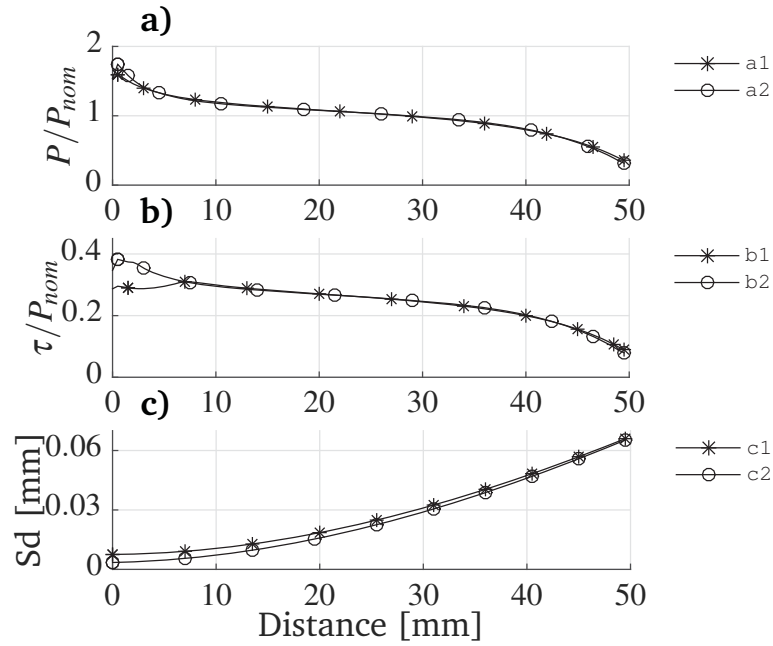
Figure B.6: Contact area status. Line number 1 corresponds to 10^4 DOF, and line number 2 corresponds to $6.3 * 10^4$ DOF. A displacement of 0.1 mm is applied to the right end of the FRP tendon. The contact pressure P and the contact friction stress τ are normalized with the nominal applied pressure P_{nom}. Sd is the sliding distance in the contact region. The length of the grips is 50 mm. A coefficient of friction $\mu = 0.25$ is applied for both contact areas.

maximum shear stress of the material.

B.4 Numerical analysis

The accuracy of the FE friction clamp can be understood by comparing numerical and experimental results. The experimental pullout results in Fig. B.7b are obtained using a setup in which the FRP tendon extends to the right of the grips. For this reason, the FE model is the same.

For the FE results in Fig. B.7, a normal force of 1, 4, 8, and 16 kN is applied to the top grip before pullout. The resulting pullout force is measured when applying a total displacement of 0.5 mm to the right end of the FRP. In the two contact areas between the grips and the FRP, a coefficient of friction $\mu = 0.25$ is used. Friction tests for basalt FRP on aluminum [1] have showed that μ has a value between 0.25 and 0.31. This value is similar with results for carbon fiber reinforced polymers on aluminum [28].

When the normal force is low, the FRP tendon slips almost at the same time along the entire contact length, as shown in Fig. B.7 a. Increasing F_n results in a nonlinear behavior of the pullout force F_x. This behavior is caused by the gradual transition
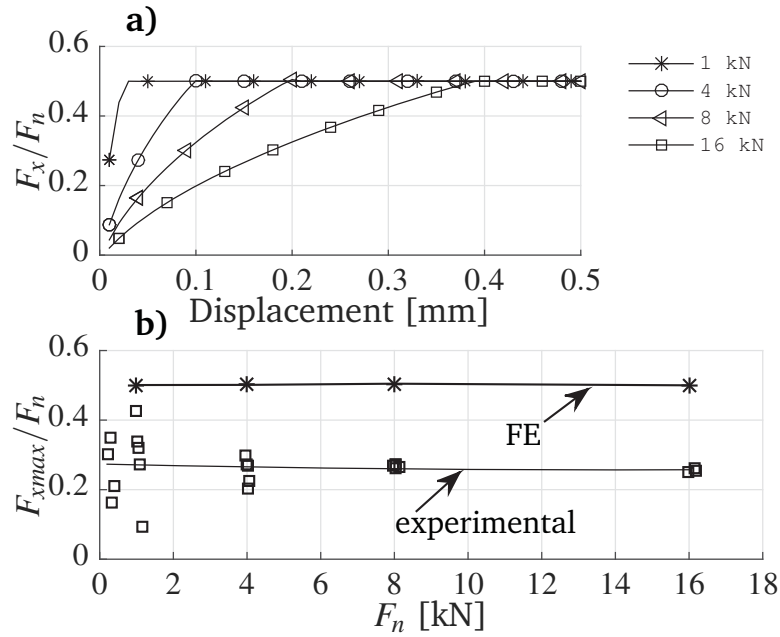
Figure B.7: Pullout force F_x for 1, 4, 8 and 16 kN normal force F_n. A displacement of 0.5 mm is applied to the FRP. The same coefficient of friction $\mu = 0.25$ is used in the two contact areas between the grips and the FRP. The maximum normalized pullout force F_{xmax}/F_n is compared with experimental results obtained for the same configuration.

from stick to slip along the contact area. The displacement required to achieve complete pullout is 0.4 mm for $F_n = 16$ kN. After pullout is achieved, F_x remains constant. This is because the static and dynamic μ is the same. No stick-slip behavior is observed, which sometimes appears for pull-out tests in laboratory conditions [56].

In Fig. B.7 b the maximum pullout force F_{xmax} is normalized with the normal force F_n. The result is compared with experimental results obtained for the same configuration [1]. Despite large scatter at low normal force, the experimental results are almost linear, with a value of 0.26. This value is almost the same with the measured μ, which shows that doubling the apparent contact area does not increase the pullout force. The FE results have a value of 0.5. Subsequent analysis investigates means of obtaining a Coulomb friction response from the FE grip system.

B.5   Frictional behavior

A parameter analysis involving several coefficients of friction is done in order to reduce the difference between the FE analysis and experimental results. A static coefficient of friction μ_s, and a dynamic coefficient of friction μ_d is introduced in the model. When the contact changes from stick to slip, the friction reduces from μ_s to

μ_d. The drop in friction is quantified by the ratio μ_s/μ_d.

For experimental results, it is also possible that μ is different between the two contact areas. These differences could be due to pollutants, different surface roughnesses, geometrical imperfections, etc. A tribotester is used to investigate the change in friction between the static and dynamic regime [57]. Friction tests are done between AISI 304 stainless steel and the basalt reinforced FRP. The acceleration from zero is $70\,mm/s^2$, followed by a constant speed of $0.5\,mm/s$. The friction ratio μ_s/μ_d is measured for a constant pressure of 3 MPa and different wait times. After waiting $180\,s$ $\mu_s/\mu_d = 8.23\,\%$. After waiting $600\,s$ $\mu_s/\mu_d = 10.52\,\%$.
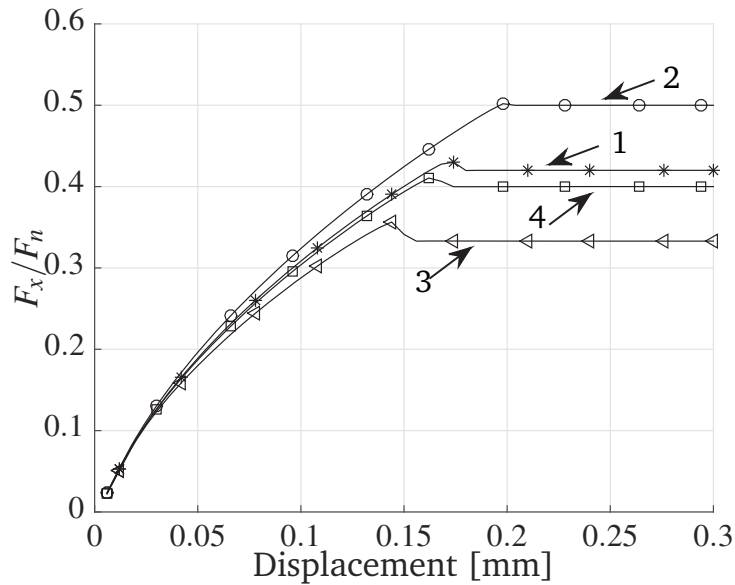
B.5.1 Static and dynamic friction

Figure B.8: Pullout force to normal force ratio F_x/F_n. For all results $F_n = 8$ kN. The displacement applied to the FRP is 0.3 mm. The static to dynamic friction ratio is μ_s/μ_d. Line 1: $\mu_d = 0.21$, $\mu_s/\mu_d = 1.2$; Line 2: $\mu_d = 0.25$, $\mu_s/\mu_d = 1$; Line 3: $\mu_d = 0.16$, $\mu_s/\mu_d = 1.5$; Line 4: $\mu_d = 0.2$, $\mu_s/\mu_d = 1.25$.

A displacement of 0.3 mm is applied to the right end of the FRP. Then the reaction force is measured. The normal force is F_n. F_x is the pullout force. The ratio of the normal force to the pullout force F_x/F_n represents the grip coefficient. For all results presented in Fig.B.8, a static coefficient of friction $\mu_s = 0.25$ is used in the two contact areas. For the result in Fig. B.8 line 2, where $\mu_s/\mu_d = 1$, no drop in friction is observed. Once the maximum F_x/F_n value is reached, the ratio remains constant for the rest of the displacement. The grip coefficient F_x/F_n is 0.5. The first step is to introduce a 20 % decrease in friction, with $\mu_s/\mu_d = 1.2$. This results in a significant drop of the grip coefficient, from 0.5 to 0.42, as shown in line 1. Further

decreasing to $\mu_s/\mu_d = 1.5$ in line 3 results in the lowest grip coefficient $F_x/F_n = 0.33$. It is observed that the displacement needed to achieve complete pullout also decreases with decreasing dynamic friction. F_x/F_n drops from the peak pullout to a steady value, once the entire contact area is moving.

Based on the experimental results with the tribotester, it is reasonable to consider that $\mu_s/\mu_d = 1.2$ is an acceptable parameter. The grip coefficient reduction is less than the reduction in friction. Between Fig. B.8 lines 1 and 2, the reduction in friction is $\mu_{d2}/\mu_{d1} = 20\%$. The reduction in grip coefficient is 16%. The biggest difference is between the results in lines 2 and 3. Here the reduction in friction μ_{d2}/μ_{d3} is 50%, and the reduction in F_x/F_n is 34%.

B.5.2 Friction variation between the two contact areas

It is made clear that using a reasonable reduction between the static and dynamic regime does result in a reduction of the grip coefficient. But there is still a large difference between experimental and numerical results. Further investigation is done for understanding which contact friction definition brings FE analysis results closer to experimentally obtained values.

The normalized grip coefficient F_x/F_n in Fig. B.9 is obtained using a 8 kN normal force. In a1 the came static and dynamic coefficient of friction is used in both interfaces, with $\mu_d = 0.21$ and $cof_s/cof_d = 1.2$. In a2, the static and dynamic friction is the same, but with different μ in each contact area: $\mu_{d1} = 0.25$; $\mu_{d2} = 0.21$; and $\mu_{s12}/\mu_{d12} = 1$. Even though the two cases should give similar results, it is clear that a lower grip coefficient is obtained when there is a drop in friction between the static and dynamic regime, as shown in a1.

It becomes clear that the change in regime between static and dynamic friction has the biggest influence over the grip coefficient. It is thus sensible to combine this with using different μ in each contact area, as shown in Fig. B.9 b. A very small difference in friction between the contact areas is used in b1. Here $\mu_{d1} = 0.21$, $\mu_{d2} = 0.2$ and $\mu_s/\mu_d = 1.2$. $F_x/F_n = 0.41$, which is lower then the 0.42 value obtained in a1. A very close value is obtained in b3, with $F_x/F_n = 0.40$. There is a bigger difference between the dynamic coefficients of friction, with $\mu_{d1} = 0.21$, $\mu_s/\mu_d = 1.2$ and $\mu_{d2} = 0.19$, $\mu_s/\mu_d = 1.3$. The result in b2 is obtained by reducing the friction in one of the contact areas more aggressively. The following values are used: $\mu_{d1} = 0.21$, $cof_s/cof_d = 1.2$ and $\mu_{d2} = 0.17$, $\mu_{s12}/\mu_{d12} = 1.2$. This leads to the most significant drop in grip coefficient, with $F_x/F_n = 0.38$.

In conclusion, the largest drop in F_x/F_n is obtained using a small difference between μ_s and μ_d, together with significantly different μ in each contact area. For experimental results, such difference in friction could be the result of having
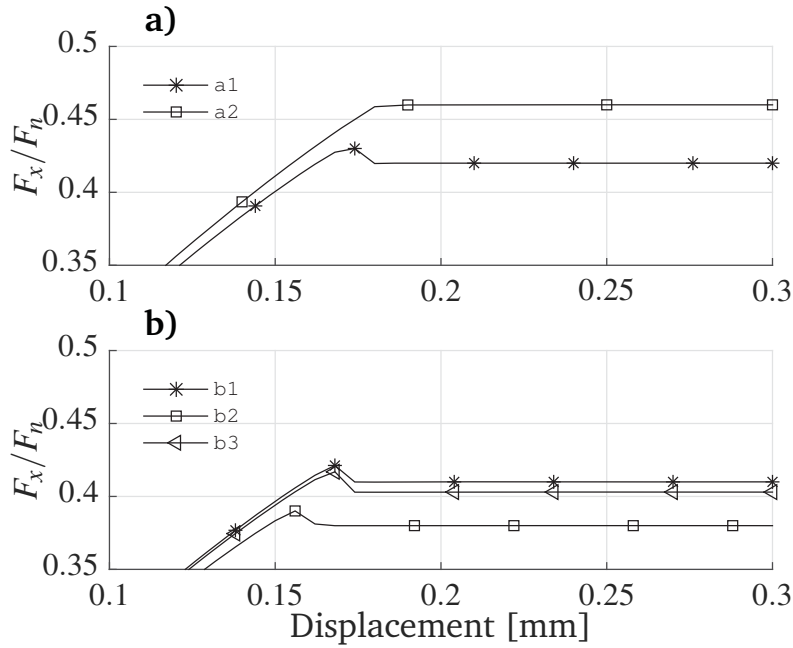
Figure B.9: Effect of friction on the grip coefficient F_x/F_n. A normal clamping force F_n of 8 kN is applied to the top grip. The displacement applied to the right end of the FRP is 0.3 mm. In the top figure, results are compared between: a1) $\mu_d = 0.21$, $\mu_s/\mu_d = 1.2$ in both contact areas; a2) different coefficients of friction between contact areas $\mu_{d1} = 0.25$, $\mu_s/\mu_d = 1$ and $\mu_{d2} = 0.21$, $\mu_s/\mu_d = 1$. In the bottom figure, results are compared between: b1) $\mu_{d1} = 0.21$, $\mu_{d2} = 0.2$, with $\mu_s/\mu_d = 1.2$; b2) $\mu_{d1} = 0.21$, $\mu_s/\mu_d = 1.2$ with $\mu_{d2} = 0.17$, $\mu_s/\mu_d = 1.2$ and b3) $\mu_{d1} = 0.21$, $\mu_s/\mu_d = 1.2$ with $\mu_{d2} = 0.19$, $\mu_s/\mu_d = 1.3$.

different surface roughnesses between the grips or due to pollution of the surface. A different waviness of the grip profile can also modify the real contact area between the grips.

Experimental tests have shown that a 50% drop between μ_s and μ_d does not occur for this material pair. It is safe to consider that the parameters in b2 are appropriate.

B.5.3   Imperfect contact

When putting the two grips in contact with the FRP, the apparent area of contact doubles. This is the effect obtained in the simulations. According to experimental results, the real contact area should remain almost constant. It is possible to model imperfect contacts between the grips and the FRP by choosing contact element pairs and making $\mu = 0$. These elements will stop contributing to the total pullout force. An algorithm is implemented, which picks contact pairs situated at the same location along the contact area, and changes their μ. By counting the total number

of selected contact pairs and subtracting it from the initial value, the loss in contact area is given in percent. The drop of the grip coefficient is calculated by decreasing the contact area from 100 % to about 67 %, and it is plotted in Fig. B.10 a.
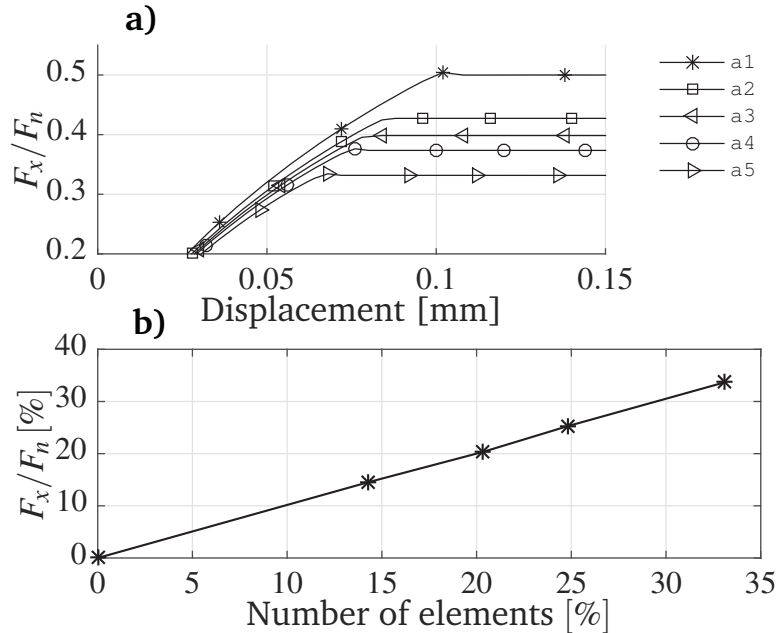

Figure B.10: Imperfect contact effect. A coefficient of friction $\mu = 0.25$ is used in both contact areas. A normal clamping force $F_n = 4$ kN is applied to the top grip. Displacement is applied to the right end of the FRP. For the results in a, the grip coefficient F_x/F_n is plotted in relation to the number of elements in contact: a1) 100%; a2) 85.71%; a3) 79.69%; a4) 75.18%; a5) 66.91%; In b, the grip coefficient decrease is given as a function of the loss of contact in percent. Here 0% is full contact and 33% represents the maximum loss of contact.

A normal force $F_n = 4$ kN is applied to the grips, before pullout. The static and dynamic coefficient of friction values are equal in both contact areas, with $\mu_s = \mu_d = 0.25$. F_x/F_n drops from a value of 0.5 at 100 % contact to a value of 0.33 at 67 % contact area. The change in grip coefficient against the change in contact area in Fig. B.10 b is linear.

The results in Fig. B.11 are obtained by putting together the friction parameters used in Fig. B.9 b2 with the contact area reduction method. The result in line 1 represent the grip coefficient corresponding to the entire contact area. The first contact area has $\mu_{d1} = 0.21$ and $cof_s/cof_d = 1.2$. The second contact area has $\mu_{d2} = 0.17$ and $\mu_s/\mu_d = 1.2$. A normal force $F_n = 8$ kN is applied to the top grip, which increases the displacement necessary to achieve pullout. For line 2 the normal force is $F_n = 4$ kN, and the contact area is 75 % of the initial value. The grip ratio drops to $F_x/F_n = 0.28$. The F_x/F_n drop in percent is equal to the reduction from the initial contact area, and has a value of 25 %. In line 3 $F_x/F_n = 0.25$. This is equal to

the experimentally obtained value. Here, the remaining contact area is 67 % of the initial value.

B.5.4   Solution

Numerical simulations show that the points at which the contact changes between stick and slip do not coincide between the two contact areas.
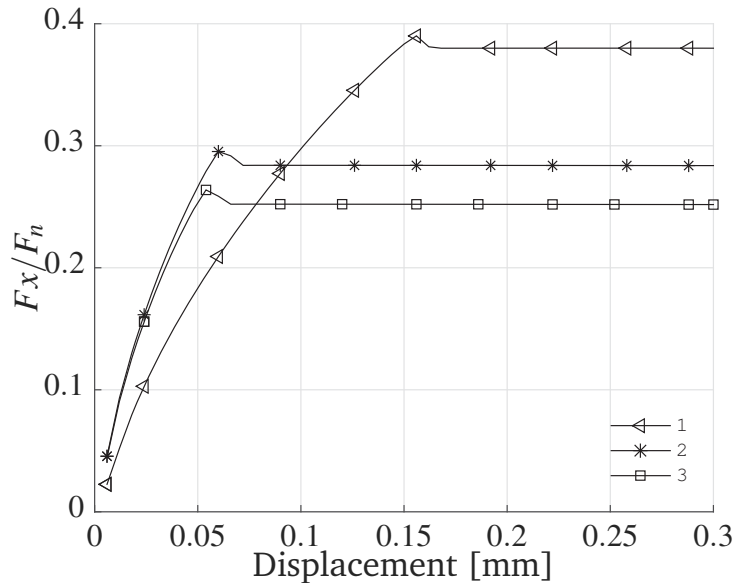

Figure B.11: Model calibration. Different coefficients of friction are used in the two contact areas between the grips and the FRP. In the first contact area $\mu_{d1} = 0.21$ and $cof_s/cof_d = 1.2$. In the second contact area $\mu_{d2} = 0.17$ and $\mu_s/\mu_d = 1.2$. Perfect contact is used for the results in line 1. A normal clamping force $F_n = 8$ kN is applied to the top grip. In line 2 only 75 % of the area remains in contact. This value is decreased to 67 % for the result in line 3.

The reduction of grip coefficient F_x/F_n is higher when the change in contact status between the top and bottom areas is large. This offset can be increased by introducing a small difference between the coefficient of friction of the two. A 20 % difference is used for the results in Fig. B.11 line 1. The drop between μ_s and μ_d, based on experimental results, is 20 % as well. If the contact area is reduced by 25 %, F_x/F_n drops to under 0.3, as shown by line 2. Matching experimental results, where $F_x/F_n = 0.25$, requires a further reduction of the contact area. The exact solution is obtained when the contact area is reduced with 33 %, as shown in line 3.

The experimental data which is used as reference in this article consists of the normal force, the pullout force and the displacement values. Until now just the normalized pullout force is compared. The FE contact sliding distance, using the parameters from Fig. B.11 line 3, is compared with experimental results obtained using a 4 kN normal force [1]. Experimentally obtained displacement values are

used, one for the left grip corner contact with the FRP, and one at the right. Digital image correlation is used to track the displacement of the FRP at these two locations.
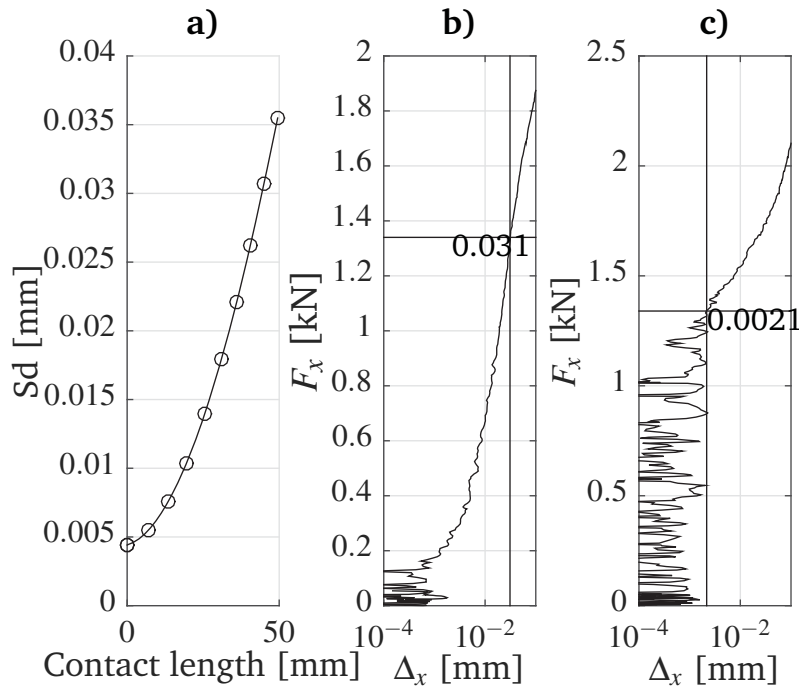

Figure B.12: Contact sliding distance compared with experimentally obtained values. Sd in line 1 is the FE contact sliding distance, where a normal force of 4 kN was applied to the top grip. The coefficients of friction in the two contact areas are $\mu_{d1} = 0.21$, $\mu_{d2} = 0.17$ with $\mu_{s12}/\mu_{d12} = 1.2$. The displacement of the FRP at the left in c, and right end in b of the grip is tracked in an experimental test with the same normal force applied to the grips. The displacement value in line c where the FRP starts to displace is the reference at which complete pullout occurs. F_x is the pullout force.

It is possible to identify the onset of displacement by plotting pullout force vs. displacement in logarithmic x axis. In Fig. B.12 c, below the horizontal line the signal is erratic, indicating noise. Above the line the signal is clear and free of noise, indicating that the FRP is sliding along the entire contact area. The displacement value of $21*10^{-4}$ mm corresponds to a pullout force of 1.33 kN. Using this force value, a displacement of $31*10^{-3}$ mm is identified in b. The FE sliding distance over the entire contact area is showed in a. This value corresponds to the first load sub-step at which the entire contact is in slip. The value of $35*10^{-3}$ mm matches well with experimental data. The value of $50*10^{-4}$ mm is in the same order of magnitude with the result in line c. In conclusion, there is good correlation between the FE end experimental displacement values.

B.6   Conclusions

The load-displacement behavior of the friction contact between an aluminum grip a FRP tendon is investigated using a 2D finite element model. The proposed model consists of two contact surfaces between the FRP tendon and the grips. Two load steps are used. First a normal force is applied to the top grip. Then displacement is applied to the composite. The contact friction force buildup, contact shear stress and contact sliding distance are modeled. An extensive analysis of the contact friction parameters is made in order to obtain good correlation between the finite element model and experimental results.

Using the experimentally obtained coefficient of dry friction for the contact pair results in large errors. Numerical analysis shows that it is necessary to include a drop in friction between static and dynamic regimes, together with using different coefficients of friction between the contact areas. The efficiency of the grip, which is the ratio of the pullout force divided with the normal force, decreases if there is an imbalance in the contact shear stresses between the two contact areas. This will allow the change from stick to slip to happen in an uneven manner between the two contact areas. Decreasing the real contact area further decreases the grip efficiency. The numerical solution agrees with the experimentally obtained grip coefficient when using a 20% drop between μ_s and μ_d. It is also necessary to use a slightly different μ between the two contact areas, and to take into account the loss of contact over small portions. The numeric and experimental sliding distance is similar. This means that the complicated pullout behavior of the grip is modeled accurately.

Based on this analysis, it is possible to improve the efficiency of a dry friction grip by increasing the contact friction, and by ensuring the same conditions in both contact areas. One way to improve friction is to increase the surface roughness of the grips, and to reduce the waviness of the profiles.

Acknowledgements

Paper C

Stress Analysis of a Friction Joint between Basalt Reinforced Composite and Aluminum

Andrei Costache[1*], Kristian Glejbøl[2], Ion Marius Sivebæk[1], Christian Berggreen[1]

[1]Department of Mechanical Engineering, Lightweight Structures Group, Technical University of Denmark, Nils Koppels Allé, Building 403, 2800, Kgs. Lyngby, Denmark

[2]National Oilwell Varco, Subsea Production Systems, Priorparken 480, 2605, Brøndby, Denmark

Abstract:

Offshore oil and gas fields benefit from the use of flexible risers which make the connection between the underwater oil well and the production and offloading equipment at the sea surface. The depletion of hydrocarbon resources close to the shoreline has driven the development of flexible risers which can operate in very deep waters. The new generation of hybrid risers will incorporate composite materials as primary load bearing elements. The subject of this paper is the proper transfer of loads between a unidirectional basalt fiber/vinylester reinforced tendon and a metallic grip. A finite element model is developed and used together with an analytic solution. Its purpose is to find the optimal solution for a double clamp with flat faces which squeezes a fiber reinforced tendon in between. The variation of the contact stress with regard to the coefficient of friction, grip geometry and position are thoroughly investigated. The numerically obtained pullout force is compared with experimental results. Based on this study, it is possible to choose a geometry which minimizes stresses and at the same time maximizes the grip efficiency.

---

[*]Principal corresponding author. Tel.: +45 45251391; E-mail: ancos@mek.dtu.dk

C.1   Introduction

Flexible risers are a type of pipe used to transport gas and liquids between the sea floor and the equipment at the sea surface. They are ideal solutions because they can withstand the high loads and displacements which occur due to the relative movement of the ships. The drive to go deeper forces the industry to look into using composite materials, which offer higher strength and stiffness to weight ratio than metals. The risers capacity to withstand high axial loads can be improved by replacing the metallic tensile armor with fiber reinforced composites. Thus, a critical problem is to ensure the transmission of loads to the FRP. Understanding the stress state in the contact region between the composite tendon and metal grips during pullout is necessary for the design of optimal friction grips.
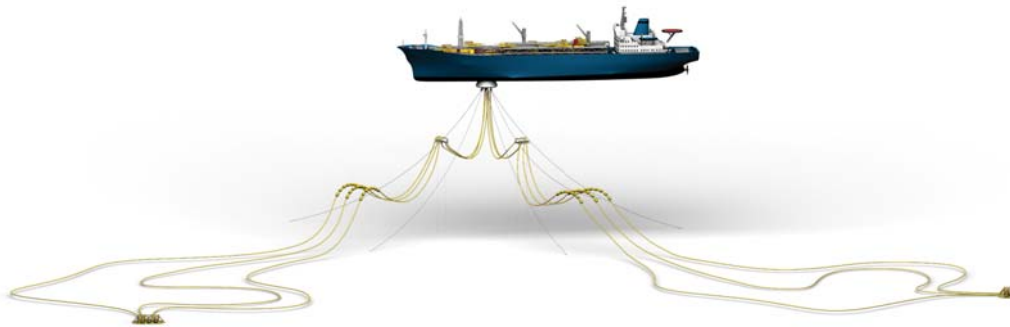

Figure C.1:   FPSO and flexible pipe connection [2].

A pure friction grip design was considered where the pullout force was transmitted through frictional shear stresses. Several advantages are achieved with such a design. The device is easy to assemble/disassemble during maintenance. There is no need to inspect the adhesion/curing as in the case of adhesive bonding. By changing the length of the grips it is possible to obtain a contact pressure value below the maximum compressive strength of the FRP.

Several anchoring systems have been investigated [19]. Most of the focus is on circular geometries [58]. Flat tensile specimens typically include adhesively joined tabs [59] to provide transition with the grips of a tensile machine [26].

In this first part, a non-linear finite element model of a FRP tendon and two symmetric aluminum grips was developed. The accuracy of the stress distribution in the interface was compared against an analytic solution [38]. The effect of the overlap length, and geometric positioning of the FRP was discussed. Next, a detailed

study of the influence of the coefficient of friction and of the maximum stress in the FRP and grips was done. Several grip profiles were modeled, to see the development of the stress state in the interface. Force and displacement was applied to the FRP to select the optimal geometry for maximal grip efficiency. Experimental results with the same geometry are used for comparison purposes.
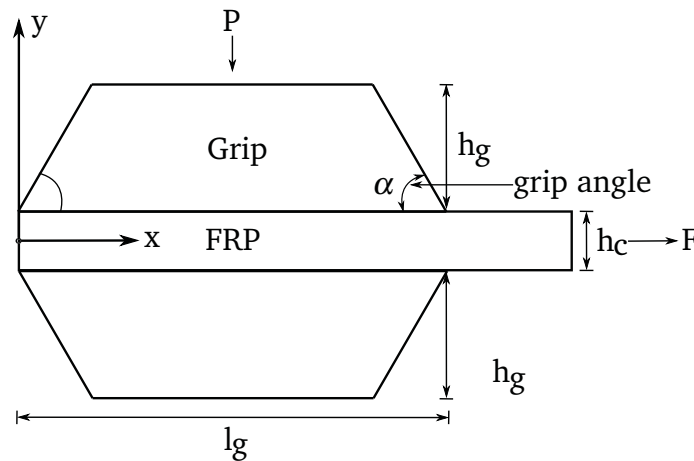
C.2   Finite element model

Figure C.2: The system consists of a unidirectional FRP tendon clamped symmetrically between two grips. The grips have length l_g and height h_g. The FRP has thickness h_c and extends outside the grips on the right side. The grip angle is denoted by α. A clamping pressure P was applied to the top grip. Force or displacement can be applied to the right side of the FRP.

The purpose of this test is to find the best geometry for the grips. The grips must transfer compressive forces to the FRP and minimize stress concentrations. The pullout force developed by the grips/FRP pair is evaluated and compared with experimentally obtained data.

The configuration of the grip and tendon analyzed is shown in Fig.C.2. A unidirectional FRP is gripped between two grips and loaded in tension at the right end. The overlap length is the contact length between the grips and the FRP. The origin of the xy coordinate system is located in the center of the tendon, at the left edge. The tilt angle between the lateral faces of the grip and the horizontal is denoted by α.

The initial dimensions are as follows: grip length $l_g = 50\,mm$, grip height $h_g = 15\,mm$, composite tendon hight $h_c = 1.5\,mm$ and overall thickness of $15\,mm$.

A 2D plane stress finite element model was built in Ansys 15.0 using 2D, 8-node solid element, as shown in Fig.C.3. The contact between the grips and the FRP

were modeled with 2D 3-node surface-to-surface contact elements. The FE mesh in Fig.C.3 consists of a densely refined grid towards the edges of the grip, and a coarser grid in the center of the model. This improves the accuracy towards the edges, where higher stresses are expected. The FRP extended to the right of the grip, in order to capture the change in stresses after the grip. The FRP mesh had the same discretization as the grip. In Fig.C.3 the angle between the lateral faces of the grip and the horizontal is $\alpha = 90°$.
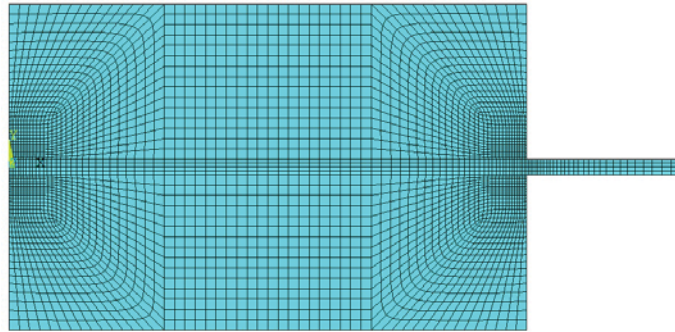

Figure C.3: Finite Element Model of the grips and FRP. A full model was built instead a 1/2 symmetric model in order to have two contact areas. In each contact area it is possible to define a coefficient of friction (μ). The top grip is allowed to move in y direction. The bottom grip is constrained in all directions. The grip angle is $\alpha = 90°$.

The grip on top can displace vertically. The bottom grip is constrained against all displacements. Two load steps were used to simulate how such a grip functions. In the first, pressure is applied to the top grip. The FRP tendon is kept in place by friction. A second load step applied displacement to the FRP in x direction. A reaction force is developed due to friction between the grips and FRP. A coefficient of friction (μ) could be defined for each contact area.

The grips are modeled as isotropic materials, with $E_x = 69$ GPa, and $\nu_{xy} = 0.33$ for aluminum. The FRP is modeled as an orthotropic material. Using a micro-mechanics approach based on fiber volume fraction and material properties of the fibers and matrix provided by the manufacturer, a transverse elastic modulus $E_y = 9.51$ GPa is calculated for the FRP. The shear modulus in principal direction is $G_{xy} = G_{xz} = 6.23$ GPa, and the transverse shear modulus is $G_{yz} = 2.59$ GPa. The major Poisson's ratios are $\nu_{xy} = \nu_{xz} = 0.29$, and the minor Poisson's ratio is $\nu_{yz} = 0.32$. The longitudinal elastic modulus E_x is determined experimentally, using five tensile tests. A value of 41.88 GPa is obtained.
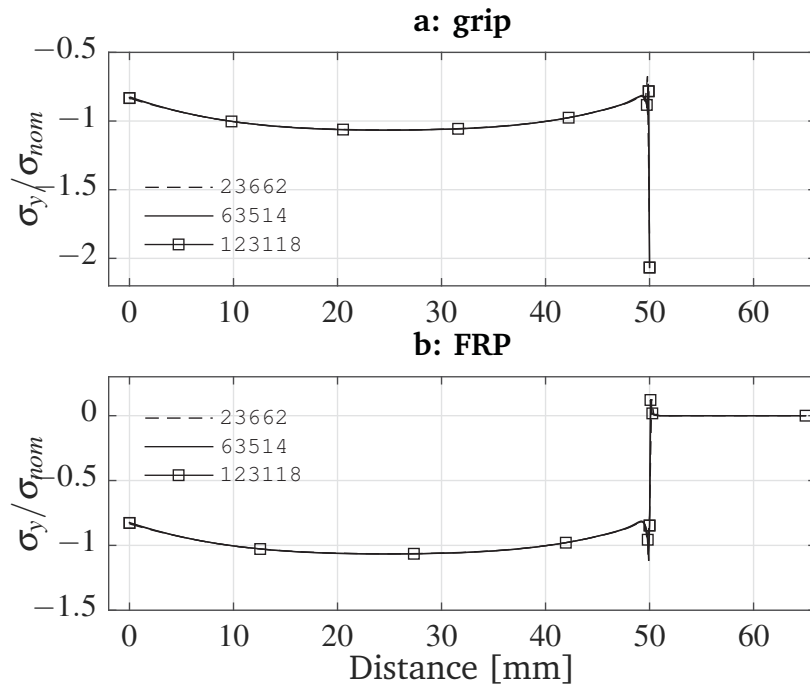
Figure C.4: The normal stress σ_y is normalized with the average distributed pressure σ_{nom} for the grip (a) and the FRP (b). Three mesh densities are compared, with 23662, 63514 and 123118 degrees of freedom (DOF). The stress is taken at the contact between the grips and the FRP, which is 50 mm long. Coefficient of friction $\mu = 0.25$.

C.3   Model validation

The stress concentration at the reentrant corner was estimated from numeric and analytic stress analyses. The normal stress was calculated by applying a 4 kN force on the top grip. This is divided over a 750 mm^2 area, resulting in a average distributed pressure of 5.33 MPa. No load was applied to the FRP tendon. A coefficient of friction $\mu = 0.25$ was used in both contact areas. Several mesh refinements were used, with 23662, 63514 and 123118 degrees of freedom (DOF). A nonlinear solver is used. The load was applied in 10 load steps for increased accuracy. The nodal stress for the aluminum grip is plotted in Fig. C.4a. The nodal stress for the FRP is plotted in Fig. C.4b.

For the grip and FRP, the stress distribution along the entire contact area has the same distribution for all mesh densities. The only difference was the maximum value at the corner. For the aluminum grip the stress profile has a concave shape along the contact length. The ratio doubles at the tip of the right corner. For the FRP the normal stress jumped from a negative ratio of -1.12 to zero value at the end of the grip. The maximum stresses for the grip in Fig. C.4a is compared with an analytic result to get the adequate mesh refinement.

A zoom of the stress distortion is shown in Fig. C.5, which shows the normalized stress σ_y/σ_{nom} for the various mesh densities. The stress at the grip edge, Fig. C.5a, increased with increasing dof. The maximum compressive stress of -2.06 was obtained for 123118 DOF. For the FRP in Fig. C.5b, the stress has a negative before the end of the grip, and a positive peak right after. The negative stress ratio is -1.12 and the positive ratio 0.12. After this the stress becomes zero.
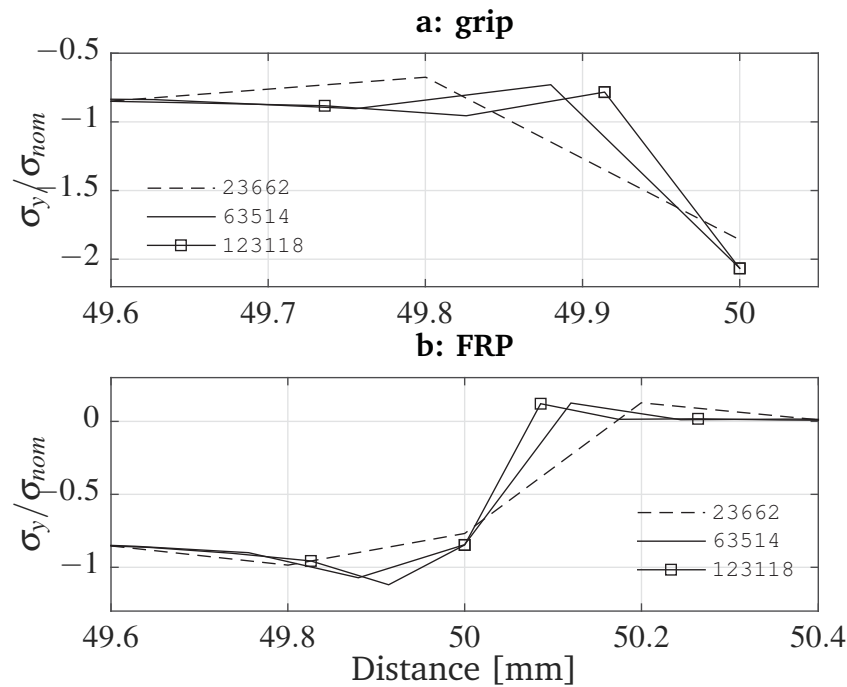

Figure C.5: Zoom of the normal stress intensity σ_y along the grip (a) and the FRP (b) for several mesh densities (23662, 63514 and 123118 DOF). The grip overlap length is 50 mm. Nominal stress $\sigma_{nom} = 5.33$ MPa. Coefficient of friction $\mu = 0.25$.

The function in Fig. C.6 is used to estimate the power of a stress singularity [38] for a block pressed against a continuum. The function F contains parameters which characterize the mismatch in the elastic constants of the two materials [39], the coefficient of friction and the grip angle. Power singularities appear for the real roots of F in the interval $0 < p < 1$. There are multiple solutions for the function F in zero and one. The non-trivial solution p is estimated numerically, and is dependent of the grip angle and the coefficient of friction. For the results in Fig. C.6, a coefficient of friction $\mu = 0.25$ is used, with grip angles α between 50° and 90°.

In Fig. C.6 the function F has a clear non-trivial solution for angles of and above 70°. The value of p is used in conjunction with Eq.C.1 to calculate the maximum stress at a sharp edge in contact with friction, where Aij is the uniform stress and r is the distance to the corner. The maximum stress values for several DOF are compared
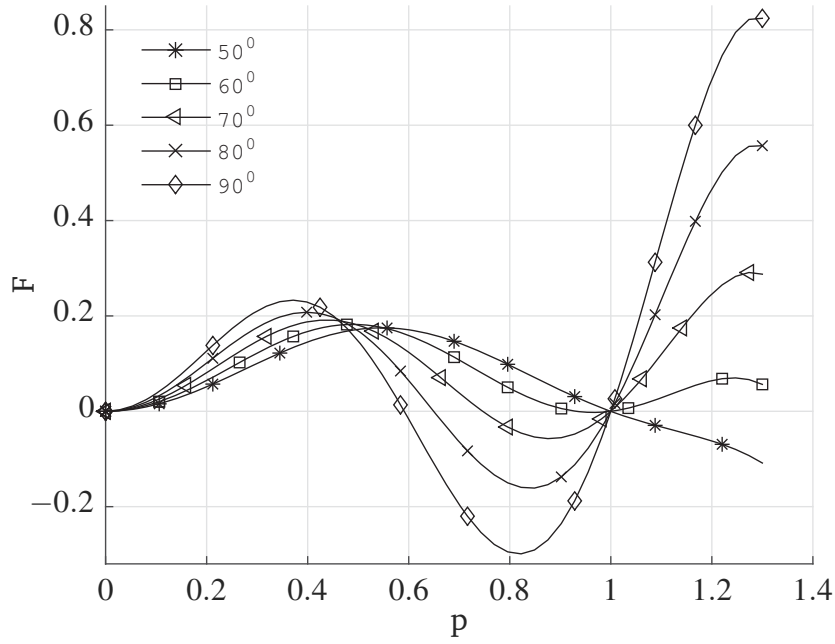
Figure C.6: The function F estimates the development of a stress concentration at a sharp edge in contact problems with friction [38]. p is the non-trivial solution of the function F. The grip angle takes values between 50° and 90°. The coefficient of friction between both surfaces is $\mu = 0.25$.

with the results from Eq.C.1.

$$\sigma_{ij} = Aij * r^{(p-1)} \tag{C.1}$$

Using the solution of F for $\alpha = 90°$, the stress at the corner grows asymptotically towards the edge no faster than $r^{(p-1)}$. Fig. C.7 shows the maximum analytic stress σ_{ymax} normalized with the uniformly distributed stress σ_{nom}, calculated based on Eq. C.1. It is used as a reference. The difference between the analytic and the maximum normal stresses at the grip for six different DOF is shown in Fig. C.7b.

It is shown that the stress increased linearly from 23662 to 63514 DOF. Between 63514 and 123118 DOF the stress remained at almost the same value. Further increasing the number of elements led to a further increase in stress. In order to keep the size of the model to a minimum, the lowest DOF which resulted in a 5% error was chosen. As such, a mesh density of 63514 DOf was used from this point on in all subsequent calculations.

C.4   Parametric analysis

The maximum contact stress σ_y in the corner region defined by the grip right end and the FRP was calculated using several clamping pressures. A clamping force of 4
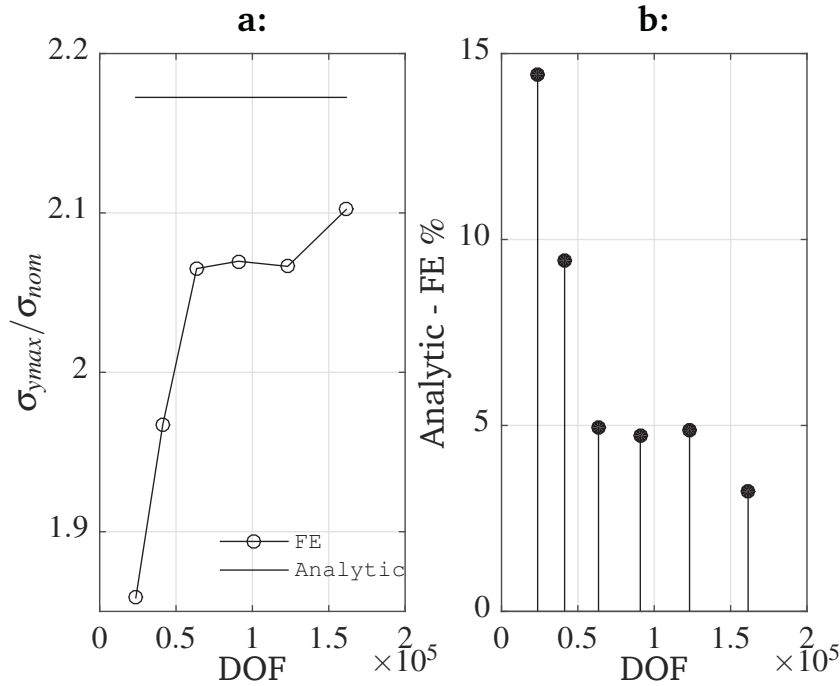
Figure C.7: Grip maximum stress for different DOF. The analytic solution is used as reference. The difference between the FE results and the analytic solution is given in percent. Coefficient of friction $\mu = 0.25$. Wedge angle 90°. Nominal stress $\sigma_{nom} = 5.33$ MPa. No load was applied o the FRP.

kN was applied in all cases and the grip length was increased from 35 to 80 mm. A coefficient of friction of 0.25 was used for the contact of both grips with the FRP. The nominal stress (σ_{nom}) is the applied force over grip area. The maximum compressive stress at the contact between the grip corner and the FRP (σ_{ymax}), normalized by (σ_{nom}) for both grip and FRP, is shown in Fig. C.8.

The stress in the grip is roughly twice as large as in the FRP. There is a rapid decrease in stress from the shortest grip length up to 50 mm. From there on the stress in the FRP becomes independent of of the grip length. The stress ratio continues to decrease even slightly from a value of 2. Because the FRP is softer than the grip, the stress transmitted by the contact is lower. For a grip length in excess of 60 mm, the peak FRP stress does not exceed the nominal stress.

C.4.1   Stress state vs. coefficient of friction

The stress state at the contact between the grips and the FRP is evaluated. A uniform normal stress σ_{nom} is applied to the top grip. No displacement is applied to the composite. For each calculation a coefficient of friction between 0.1 and 0.5 is used. Two geometries were examined. In the first geometry, the FRP does not extend beyond the unloaded side of the grip, and is designated with number 1 in Fig.
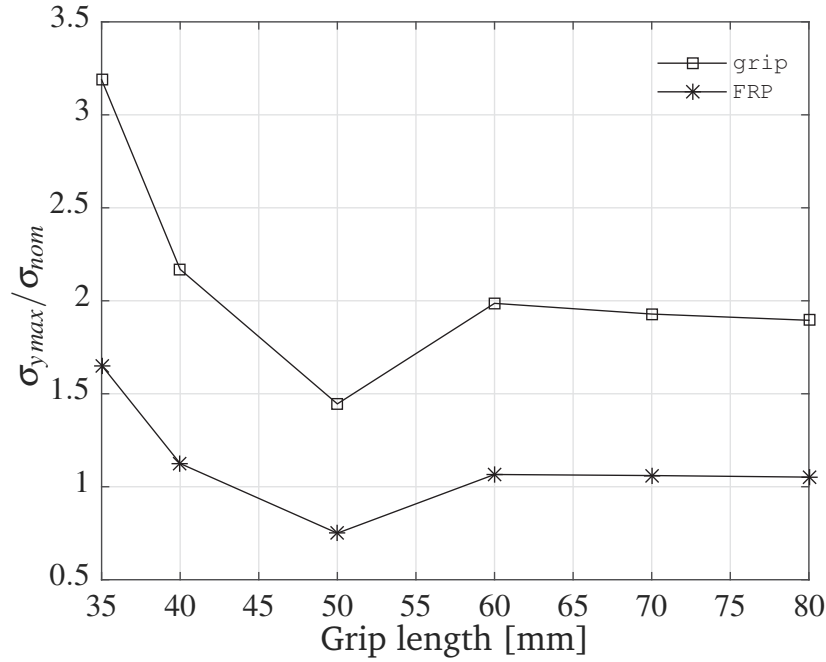
Figure C.8: Grip length effect. The stress is evaluated at the contact between the right grip corner and the FRP. The maximum normal stress (σ_{ymax}) is divided by the nominal stress (σ_{nom}) for the grip and the FRP. The grip length is increased from 35 mm to 80 mm. A nominal stress $\sigma_{nom} = 5.33$ MPa is applied in all cases. Coefficient of friction for both interfaces is 0.25. All cases were calculated for a 90° grip angle.

C.9. For the geometry designated with number 2 in Fig. C.9, the FRP is extending on both sides of the grip. The the maximum normal σ_{ymax}, longitudinal σ_{xmax}, and shear stresses τ_{xymax} are normalized with the normal stress σ_{nom}. These stresses are taken at the right grip corner, where contact between the grip and FRP occurs.

The normalized normal stress $\sigma_{ymax}/\sigma_{nom}$ decreases non-linearly with increasing friction for both the grip and the FRP, is shown in Fig. C.9 A,B. When the FRP extends on both sides of the grip, the normal stress is higher in both contact materials. A similar trend is observed for the normalized longitudinal stress $\sigma_{xmax}/\sigma_{nom}$. It is in the FRP that a clear difference between the two griping configurations is observed, as shown in Fig. C.9 C,D. This decrease in normal and longitudinal stress happens together with an increase in shear stress in both grip and FRP. The effect is more pronounced for the FRP in Fig. C.9 F.

C.4.2   Optimal grip angle

The function F in Fig. C.6 shows for which grip angle values a stress concentration appears. Until now, all results have been based on a geometry with $\alpha = 90°$. Based on analytical results, the minimum angle for a stress concentration to develop is 60°.
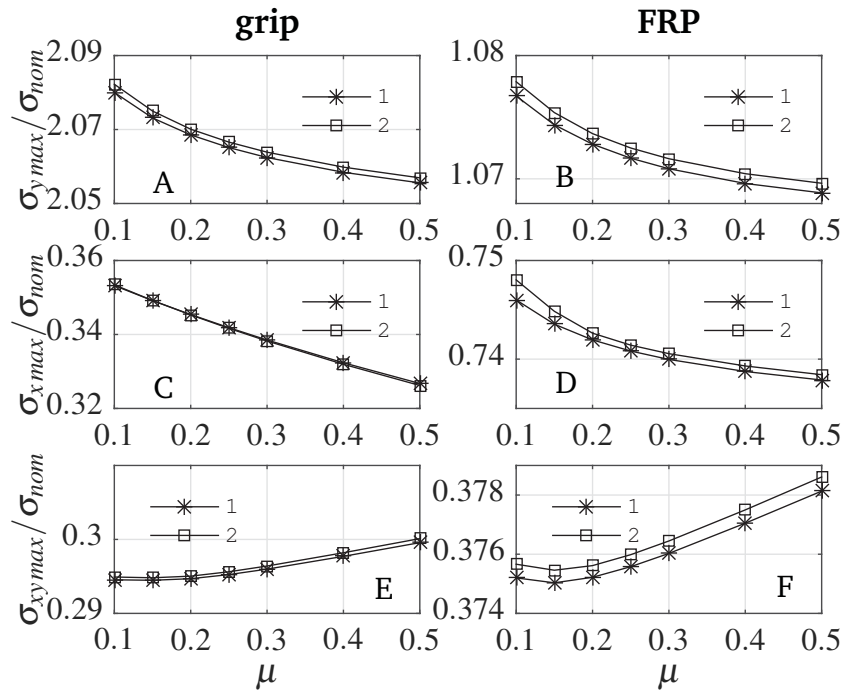
Figure C.9: Maximum normal stress σ_{ymax}, longitudinal stress, σ_{xmax}, and the shear stress τ_{xymax}. The results are normalized with the nominally applied stress $\sigma_{nom} = 5.33$ MPa. For legend 1 the FRP did not extend beyond the unloaded side of the grip. For legend 2 the FRP did extent on both sides of the grip. Wedge angle $\alpha = 90°$. The grip length is 50 mm.

In order to find the optimal grip geometry, the normal stress at the contact between the grip and FRP is compared for angles of 50°, 70° and 90°. The composite tendon did extend on both sides of the grip. A nominal stress of 5.33 MPa is applied to the grips, and no forces are applied to the composite. The results in Fig. C.10 have been normalized for both grip and FRP.

The stress profile for $\alpha = 50°$ has a pronounced oval shape, with the maximum at 25 mm distance. Due to the decreased stiffness of the canted profile, the stress is greatly minimized at the edge if the grip, with a smooth transition to zero. This is valid for both the grip and the FRP. Increasing the grip angle to $\alpha = 70°$ results is a more flat stress profile. A stress ratio of 1 is obtained in the middle of the profile, and the value decreases towards the edges. There is a very small increase in stress right at the edge of the grips. For the FRP the value is insignificant. For the grip the value is half the value of the stress at the 25 mm length. This result confirmed the analytical estimation only qualitatively, and shows that the stress transmitted to the FRP at the grip edge is minimal. Further increasing the grip angle to $\alpha = 90°$ results in the most flat stress profile. Even so, there is a reduction in stress towards the edges, before the stress ratio doubles at the edge of the grip. Because the FRP is softer, the transmitted peak stress is only 1.07. This means that it is less probable to
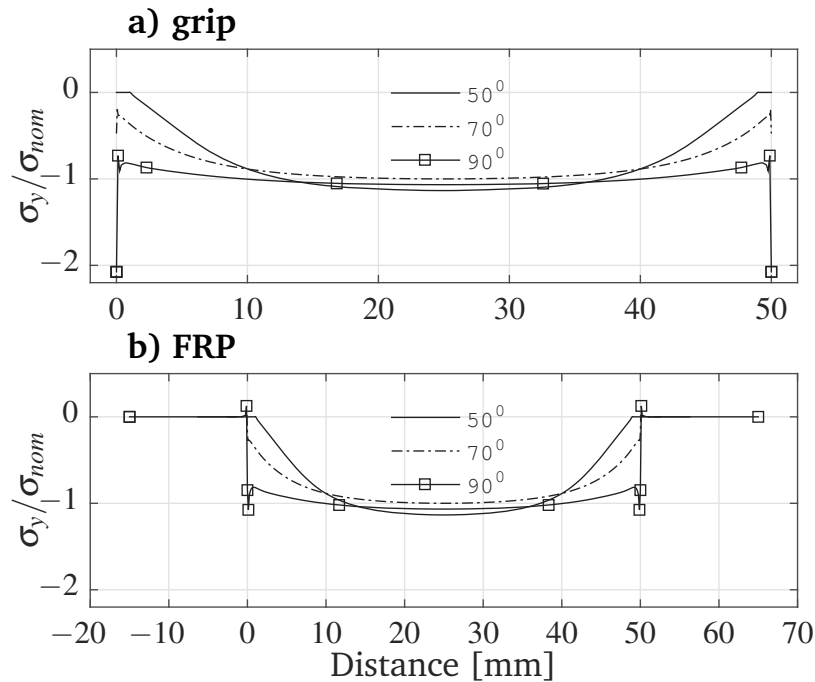
Figure C.10: Stress distribution for grip angles $\alpha = 50°$, $70°$ and $90°$. σ_y is the normal stress. The FRP did extend on both sides of the grip. The coefficient of friction is $\mu = 0.15$. The results are normalized with the nominally applied stress $\sigma_{nom} = 5.33$ MPa.

damage te composite, even when using $90°$ grips. From Fig. C.10 can be concluded that a $70°$ grip angle combines minimum stress at the grip corners with an optimal stress distribution.

C.4.3   Gripping method

The gripping method reffers to the relative position of the grips and FRP. A normal stress σ_{nom} is applied to the grips. This stress is transmitted to the FRP through contact. Because the FRP is the weakest material, only the stress in the FRP is analyzed.

Two sets of grips are compared. The first set has a $70°$ grip angle to the right and a $90°$ angle to the left. The second set is symmetric with $\alpha = 70°$ at both ends. The FRP extends on both sides of the grip in one configuration, as shown in Fig. C.11 B,D. In the second configuration, the FRP does not extend after the left grip edge, as shown in Fig. C.11 A,C.

If the left grip angle is $\alpha = 90°$, the stress ratio at 0 mm is close to -0.9, see Fig. C.11 A. The maximum stress is skewed towards the 20 mm mark, and has a value of -1.125. Using a left grip angle of $\alpha = 70°$ reduces the stress ratio to -0.2 at the 0 mm mark, as shown in Fig. C.11C. The stress profile along the contact length is no
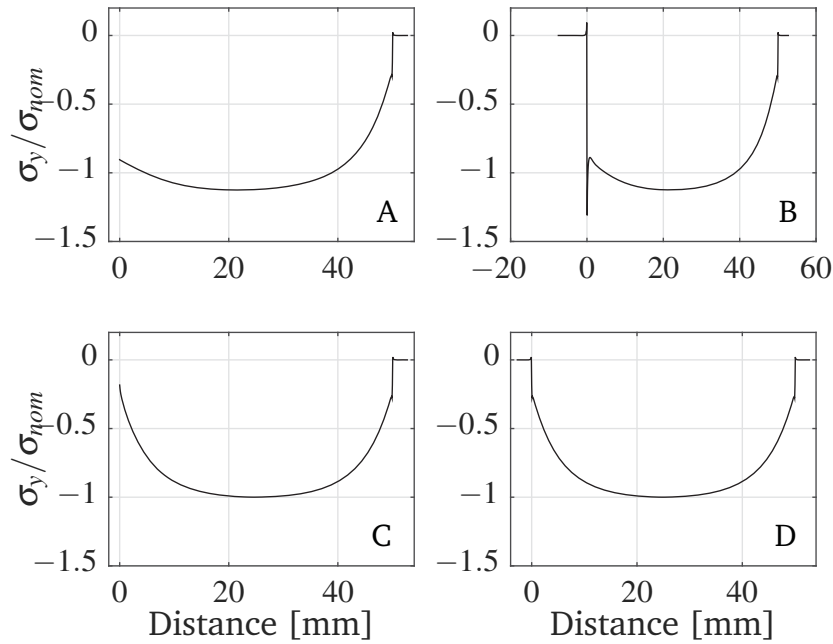
Figure C.11: Normal stress σ_y in the FRP. In legends A and C the FRP did extend only to the right side of the grips. In B and D the FRP did extend on both sides of the grips. For A and B the grip angle was 90° to the left and 70° to the right. For C and D the grip angle was 70° on both sides. The coefficient of friction is $\mu = 0.15$. The results are normalized with the nominally applied stress $\sigma_{nom} = 5.33$ MPa.

longer exceeding the -1 value. In Fig. C.11B the FRP extends on both sides of the grip. The left grip angle is $\alpha = 90°$. The maximum σ_y/σ_{nom} value increases to -1.31. The most balanced stress profile is obtained for a symmetric grip with $\alpha = 70°$, and with the FRP extending on both sides of the grip. This is shown in Fig. C.11D. There are no significant variations in the stress at the contact with the corners of the grips. The stress profile is symmetric, with the maximal σ_y/σ_{nom} value in the middle of the overlap length.

C.4.4 Summary of results

A summary of the maximum stresses at the grip edge, together with the influence of the coefficient of friction and grip angle is presented in Table.C.1. These results are obtained by applying a uniform normal stress to the grips. For $\alpha = 50°$ grip angle the stress values at the contact with the corners of the grips are very small. For this reason, the results are not normalized. It is observed, that for all geometries with $\alpha = 50°$, the longitudinal stress σ_x is quite small.

The largest σ_y values are obtained for $\alpha = 90°$. σ_y depends on the length of the FRP and the coefficient of friction. Higher σ_y are obtained when the FRP extends

Table C.1: Effect of grip configuration and coefficient of friction (μ) on the maximum stresses.

Geometry		α [deg]	μ	σ_x^{max} [MPa]		σ_y^{max} [MPa]		τ_{xy}^{max} [MPa]	
				grip	FRP	grip	FRP	grip	FRP
1		90	0.15	1.862	3.965	11.056	5.730	1.570	2.000
			0.3	1.805	3.946	10.999	5.711	1.578	2.005
2			0.15	1.862	3.972	11.066	5.735	1.572	2.002
			0.3	1.803	3.949	11.007	5.715	1.580	2.007
3		70	0.15	1.925	1.431	2.711	1.595	0.971	0.558
			0.3	1.852	1.408	2.720	1.602	0.996	0.577
		50	0.15	0.121	0.427	0.0	0.0	0.0	0.0
			0.3	0.139	0.399	0.0	0.0	0.0	0.0
4		70	0.15	1.935	1.437	2.731	1.607	0.980	0.563
			0.3	1.861	1.413	2.741	1.614	1.006	0.583
		50	0.15	0.121	0.423	0.0	0.0	0.0	0.0
			0.3	0.139	0.394	0.0	0.0	0.0	0.0
5		70	0.15	1.805	1.320	2.533	1.484	0.903	0.520
			0.3	1.744	1.299	2.539	1.488	0.923	0.535
		50	0.15	0.108	0.422	0.0	0.0	0.0	0.0
			0.3	0.125	0.397	0.0	0.0	0.0	0.0
6		70	0.15	1.799	1.318	2.530	1.483	0.903	0.520
			0.3	1.736	1.296	2.538	1.488	0.924	0.536
		50	0.15	0.105	0.422	0.0	0.0	0.0	0.0
			0.3	0.126	0.397	0.0	0.0	0.0	0.0

on both sides of the grips. This is shown in Table. C.1, line number 2. Results at line numbers 3 to 6 confirm the absence of any stress jump for $\alpha = 50°$ in all configurations. For $\alpha = 70°$, σ_y increases with increasing coefficient of friction. The shear stress, τ_{xy}, increases with a maximum of under 4% for all geometries from $\mu = 0.15$ to 0.3. For $\alpha = 70°$, σ_y was less than the average distributed stress.

C.5 Pullout

Two load steps are used for simulating pullout. First a uniformly distributed stress $\sigma_{nom} = 5.33$ MPa is applied to the grips. Then a pullout force P_f of 0, 0.5, 1 and 1.5 kN is applied at the right end of the composite. Two coefficients of friction,

μ = 0.25 and 0.35, are used. The shear stress τ_{xy} in Fig. C.12 a is obtained after griping the FRP. The local shear at the right end of the grip is caused by the local deformation of the FRP.
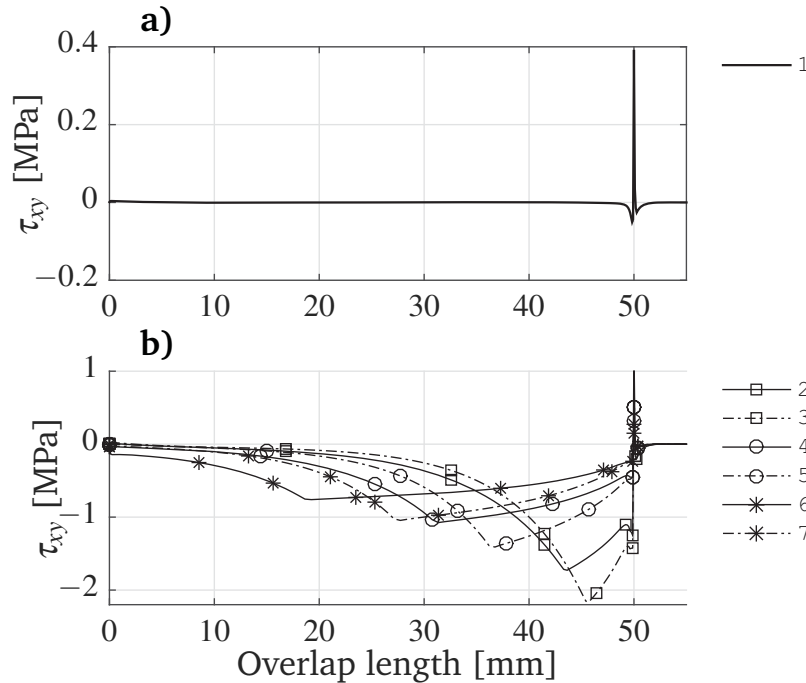

Figure C.12: Shear stress in the FRP during pullout. Wedge angle $\alpha = 90°$. The grip length is 50 mm. Nominal stress $\sigma_{nom} = 5.33$ MPa. A pullout force P_f between 0 and 1.5 kN was applied to the FRP. 1 - [μ = 0.25, P_f = 0 kN]; 2 - [μ = 0.25, P_f = 0.5 kN]; 3 - [μ = 0.35, P_f = 0.5 kN]; 4 - [μ = 0.25, P_f = 1 kN]; 5 - [μ = 0.35, P_f = 1 kN]; 6 - [μ = 0.25, P_f = 1.5 kN]; 7 - [μ = 0.35, P_f = 1.5 kN];

In Fig. C.12 b, a constant load is applied at the right end of the FRP. In Fig. C.12 b2 a force of 0.5 kN is applied. The coefficient of friction is μ = 0.25. The result is a drop in the shear stress from 2.1 MPa to 0.9 MPa, and the development of a second shear peak at -1.15 MPa. For the same pullout force and μ = 0.35, a shear stress of -1.44 MPa is obtained in Fig. C.12 b3. Subsequent increases in pullout lead to a decrease of this negative shear stress. The peak shear stress moves from the right to the left of the grip.

It is clear that for μ = 0.35, the peak had a larger value and was trailing behind the peak at μ = 0.25. The peak negative shear stress indicates where contact changes from stick to slip. From Fig. C.12 b2 to b7 it is possible to see for a certain load level how much of the contact is in stick or slip.

The efficiency of the grip was compared for several grip angles and different coefficients of friction. The grips are symmetric, with $\alpha = 50°, 70°, 90°$. At the contact between the grips and the FRP the contact can change from stick to slip. When there
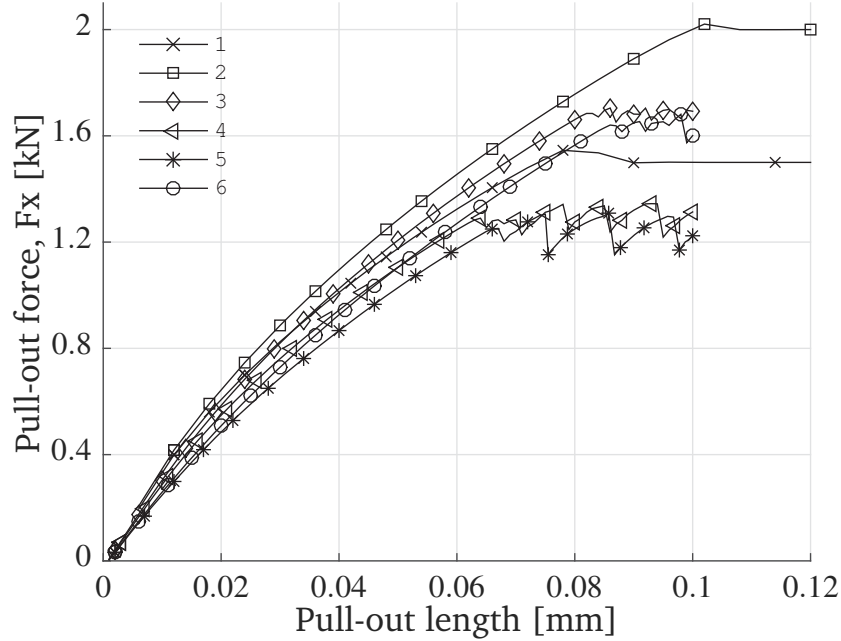
Figure C.13: Pullout force vs. pullout length. A nominal stress $\sigma_{nom} = 5.33$ MPa is applied to the grips. The pullout length is the displacement applied to the right end of the FRP. The composite did extend on both sides of the grip. μ_{d1} and μ_{d2} were the coefficients of friction for the two interfaces. The static to dynamic ratio was defined as μ_s/μ_d. 1 - [$\alpha = 90°, \mu_{d1} = 0.20, \mu_{d2} = 0.16, \mu_s/\mu_d = 1.2$]; 2 - [$\alpha = 90°, \mu_d = 0.25, \mu_s/\mu_d = 1$]; 3 - [$\alpha = 70°, \mu_d = 0.25, \mu_s/\mu_d = 1$]; 4 - [$\alpha = 70°, \mu_{d1} = 0.20, \mu_{d2} = 0.16, \mu_s/\mu_d = 1.2$]; 5 - [$\alpha = 50°, \mu_{d1} = 0.20, \mu_{d2} = 0.16, \mu_s/\mu_d = 1.2$]; 6 - [$\alpha = 50°, \mu_d = 0.25, \mu_s/\mu_d = 1$];

is no relative movement between the contact node pairs, the contact shear stress is calculated with the static coefficient of friction μ_s. Once the shear stress exceeds the static shear stress value, the contact changes from stick to slip. The dynamic shear stress is calculated with using the dynamic coefficient of friction μ_d The static to dynamic friction ratio μ_s/μ_d takes into account how much the friction changes from stick to slip. By applying displacement to the FRP, the maximum friction force in the grip is measured. A clamping force of 4 kN is applied for all results in Fig.C.13. The pullout force F_x was plotted vs. pullout length.

The wedge angles are $\alpha = 90°$ for Fig. C.13 legends 1,2, 70° for Fig. C.13 legends 3,4, and 50° for Fig. C.13 legends 4,5. The same coefficient of friction is used for both interfaces in legends 2, 3 and 6, with no change between the static and dynamic friction, $\mu_s/\mu_d = 1$. The pullout force for $\alpha = 90°$, legend 2, is significantly higher then the 70° and 50° results. No drop in force was observed after the peak value.

For the results in Fig. C.13 legends 1, 4 and 5, two different coefficients of friction are used, $cof_{d1} = 0.20, cof_{d2} = 0.16$. A 20% drop in friction between the static and dynamic regime is considered, with $\frac{cof_s}{cof_d} = 1.2$. These parameters give a significant

drop in pullout force. Results with 70° and 50° angles showed a pronounced stick-slip behavior, especially for results with legends 4 and 5. The 90° angles did not produce stick-slip. A small drop in force was obtained for Fig. C.13 legend 1.

Correlating the results in Fig. C.13 legend 1 and Fig. C.10, the highest results were obtained in the case where the stress distribution was the flattest, with significant stress singularities at the corners. A lower pullout force was obtained when the stress concentration value was zero or smaller then the average distributed stress. For the 70° and 50° grip angles, the coefficient of friction had more influence than the geometry. Significant stick-slip behavior was also obtained.

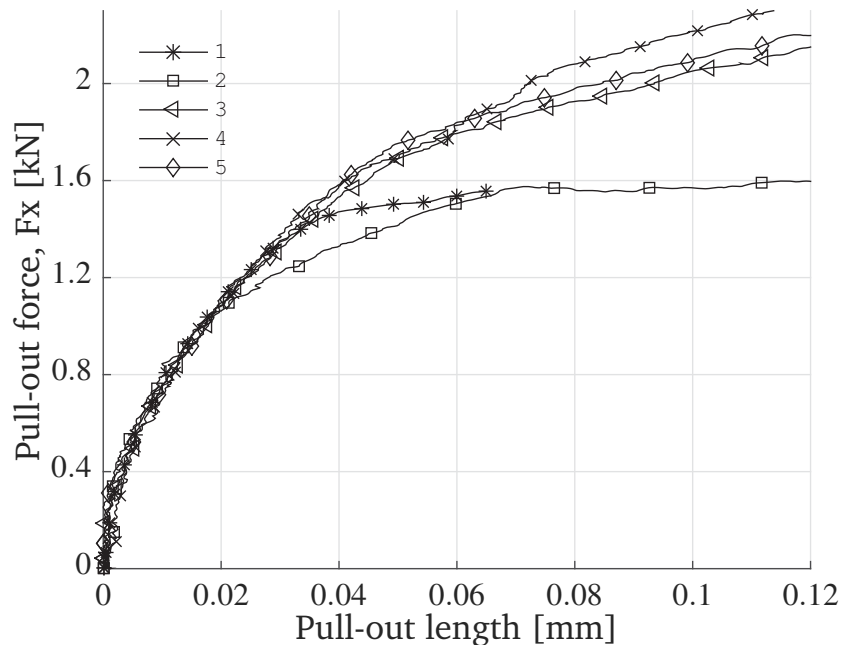### C.5.1 Experimental pullout results

Figure C.14: Experimental pullout tests for a nominal stress $\sigma_y = 5.33$ MPa. The composite did extend on both sides of the grip. Wedge angle $\alpha = 90°$. The grip length is 50 mm. Five tests are presented, and numbered with legends 1 to 5.

A set of five experimental pullout tests is presented in Fig. C.14. These are obtained using a test setup where two aluminum grips were pressed against a strip of FRP material with the same dimensions as the FE model. A 50 mm long grip with a 90° grip angle is used. Two stiff plates are used to press together the grips with a uniformly distributed pressure. The same materials are used, and the extensive experimental procedure and test results are presented in [1].

After the clamping pressure is applied, the grip setup is put in a universal tensile machine and the FRP is pulled out. The reaction force is measured. The FRP is

pulled with a constant speed of 0.3 mm/min. Fig. C.14 shows that the pullout force vs. displacement response is non-linear for the entire test. 4 out of 5 tests have the same behavior up to a value of 1.4 kN. After this point the FRP starts to slide along the entire contact region between the grips.

The pullout continues to increase slowly in some cases, but this is a result of material transfer and plastic deformation of the FRP matrix material. The maximum pullout force in Fig. C.13 legend 1 is 1.5 kN. Even though the experimental results show a significant amount of scatter, the values between Fig.C.13 and C.14 are similar. For the numeric results a larger pullout length before failure is obtained. It was not possible to capture the slow increase in pullout after slip, but this occurs after the grip has failed.

C.6 Conclusions

In this study the stresses at the contact between aluminum grips and a FRP tendon has been analyzed using a FE model. It was shown that the stress increase at the contact between the FRP and a sharp grip corner scales non-linear with the normal applied pressure. The maximum normal stress in the composite was found to be much lower then that experienced by the grip. This result showed that a double grip design using dry friction is a viable method of clamping unidirectional composite materials. Various grip angles were examined to find a configuration without increasing the stress.

Several stress profiles in the contact area were evaluated, together with different positions between the grip and FRP. This made possible to find the best grip geometry and position, which is a 70° grip angle with the FRP extending on both sides of the grip.

Extensive parametric analysis show that the coefficient of friction did influence the normal stress σ_y. Tests have shown that the maximum shear stress during pullout did not exceed the static value. This made possible to track the boundary between stick and slip in the grip, by looking at the maximum shear stress σ_{xy} during pullout. Applying displacement to the FRP showed that the grip geometry has a strong influence on the pullout force. By applying different static and dynamic coefficients of friction, the pullout force was reduced, which is in agreement with previous experimental and numerical analysis [1]. It is thus possible to design and evaluate efficient mechanical grips for flat FRP specimens.

Acknowledgements

Paper D

Improved friction joint with v-shaped grips

Andrei Costache[1][*], Kristian Glejbøl[2], Ion Marius Sivebæk[1], Christian Berggreen[1]

[1]Department of Mechanical Engineering, Lightweight Structures Group, Technical University of Denmark, Nils Koppels Allé, Building 403, 2800, Kgs. Lyngby, Denmark

[2]National Oilwell Varco, Subsea Production Systems, Priorparken 480, 2605, Brøndby, Denmark

Abstract:

Flexible risers are used in the oil industry to transport liquids and gas from the sea-floor to extraction and production equipment at the sea surface. Ongoing research aims at using composite materials instead of steel, in order to reduce weight and increase stiffness. Ensuring an optimal load transfer between the composite and metal components is very important. This paper presents an improved method for anchoring a flat fiber reinforced tendon using a double grip system with canted faces. The novelty of this paper is that it presents all the tools necessary to develop a superior grip, using dry friction. Experimental equipment and results are used together with a new finite element model. The experimental results show that the grip system works as expected, and are used to calibrate the model. Numerical results offer an in-depth understanding of the influence of friction and geometrical parameters over the grip efficiency. This makes possible to select the optimal grip design. Results show that this is a superior solution, when compared to previous attempts. It is also shown that this grip offers immediate technical applications, in a variety of conditions.

[*]Principal corresponding author. Tel.: +45 45251391; E-mail: ancos@mek.dtu.dk

D.1   Introduction

Unbonded flexible pipes are used in the offshore oil industry to connect from the subsea oil wells to extraction and production equipment at the sea surface. These pipes can be also used to connect between underwater facilities, or between ships. They offer many advantages when compared to traditional stiff pipes. Because they are flexible, they come spooled on large reels, and can be installed very fast. Their flexibility also compensates for the relative movement between the ship and the seabed.

Flexible risers are designed to withstand a multitude of dynamic load cases, which include cyclic tension, compression and bending. The main limitation of these systems is their ability to withstand dynamic tensile loads. These are caused by their own weight, coupled with the vertical rise and fall of the floating facility.

For ultra-deep water it is necessary to use composite materials instead of steel. This would increase the stiffness, while at the same time reducing weight and improving buoyancy. The internal structure of the risers consist of several concentric layers, each having a dedicated purpose. Steel was used in all structural layers, while polymers are used as permeation and protection barriers.

Recent designs intend to replace the pressure armor [52], or the tensile armor with composite materials. Glass fiber tapes are proposed as a reinforcement between two extruded layers [53]. A prominent example of unbonded flexible pipe design is the Flextreme$^{\text{TM}}$ concept [17]. It consists of only three concentric layers. The inner layer resists the outside pressure, the center layer resists the internal pipe pressure, and the CFRP armor gives the pipe its tensile strength.

The tensile armor gives the riser its longitudinal strength, and consists of two helically wound layers. The optimal shape of the tensile wires is rectangular, in order to stack the maximum amount of material in a reduced space. The wires terminate in the end-fitting, and have be anchored individually, see Fig. D.1.

Using a grip system to anchor a flat fiber reinforced specimen is a less developed topic. Initial effort concentrated on gripping circular tendons. Prestressing carbon fiber reinforced tendons is investigated both experimentally [22], as well as numerically [54], using different configurations [19]. Adhesive bonding was used initially for anchoring rectangular strips [18]. The first study into frictional anchoring of strips used a barrel and wedge design [27], and focused on minimizing the stresses in the composite. More advanced profiles were developed since [55].

There are several reasons for using friction instead of adhesion: the clamp can be taken apart with ease for repairs; there is no need to use adhesives or to verify the curing process; and the contact pressure can be controlled by changing the length of
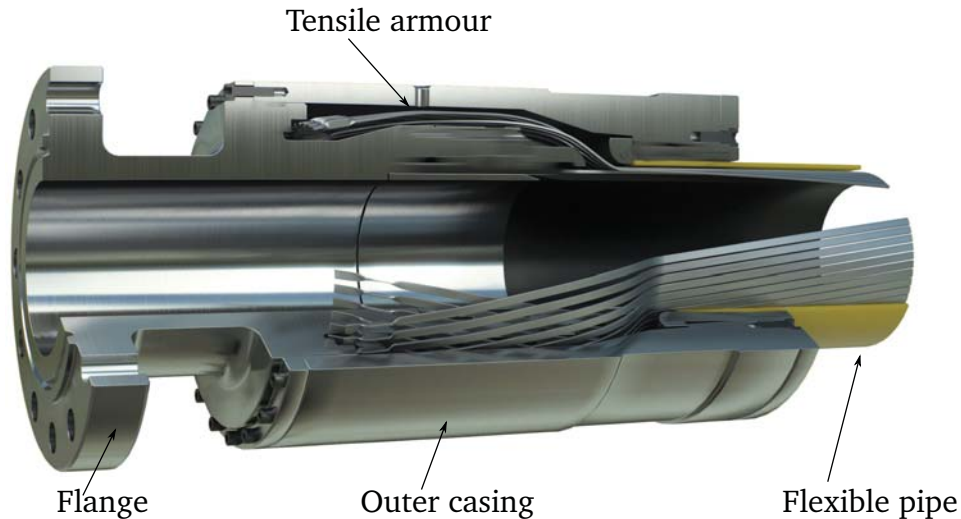
Figure D.1: Typical end-fitting for unbonded flexible pipes. The tensile armor wires give the pipe its tensile strength. They terminate in the end-fitting, and have to be anchored in order to transfer loads from the pipe to the flange. The anchoring method is critical for the structural integrity of the pipe/end-fitting assembly.

the grips.

This paper combines experimental and finite element analysis of an improved double clamp design with flat faces. Two v-shaped grips are used to squeeze a fiber reinforced polymer tendon. The experimental results and setup are used to provide information about the behavior of the device, and to measure the parameters which are then used by the finite element model. The FE analysis builds on the experimental results and is used to investigate the influence of the coefficient of friction and geometry on the contact pressure and pullout force.

D.2   Model geometry

The basic structure of the system is shown in Fig. D.2. It consists of two v-shaped grips, which make contact with the FRP on one side, and slide against 2 inverted grips to the other side. These inverted grips are called the fixture.

The grips have a height h1 to the left and h2 to the right. The contact area between the grips and the FRP has the length l1. On the opposite side to the contact with the FRP, the grips are tilted with an angle α. The composite extends to both sides of the grips, and has the height h3. Pressure P is applied to the top fixture. The pullout force Fx is obtained by pulling the FRP in positive x direction.

As boundary conditions, the following has to be considered: The bottom fixture is constrained against displacement in x and y direction. The top fixture can displace vertically under the influence of P, but cannot move in x direction.
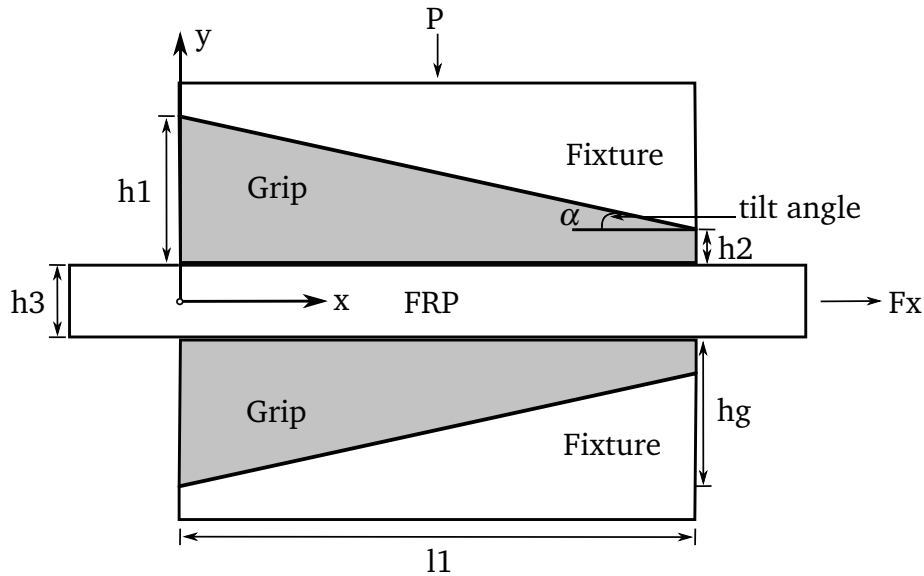
Figure D.2: Model geometry. The system consists of two v-shaped grips and a unidirectional basalt fiber reinforced polymer in between. The grips are held in a fixture to which pressure is applied. The wide end of the grip has height h1. The narrow end has height h2. Total grip length is l1. The FRP can extend to both sides of the grip. The force Fx is obtained by pulling the FRP in x direction.

D.3   Experimental setup

The test rig consists of the components described in Fig. D.2, plus some additional elements. The two grips which compose the fixture are held together by two thick metal plates. These plates have a guide-rail to center the fixture and a set of washers to hold them in place. The plates are pressed with a uniformly distributed load. This clamping force is achieved by tightening 4 bolts, and the load value is monitored with the help of a specially designed strain gage setup [1]. The entire test rig is installed vertically in a universal tensile test machine. Displacement is applied to the specimen using a constant rate. The pullout force is sampled using a load cell.

All loads, which include the clamping force, the pullout force and the displacement of the actuator, are recorded using a digital logger. The sampling frequency is set at 5 Hz. The displacement of the FRP tendon in the grip area is monitored using digital image correlation. The system is capable of recording very accurately the displacement. This data is also logged with 5 Hz frequency. A trigger signal starts all the equipment simultaneously. This ensures that the load and displacement vectors are synchronized.

Fig. D.3 shows the stochastic pattern painted on the grips and FRP tendon. The DIC system creates facets on the surface of the test rig components, and is able to track their position. Two reference surfaces are attached to the compression plates,
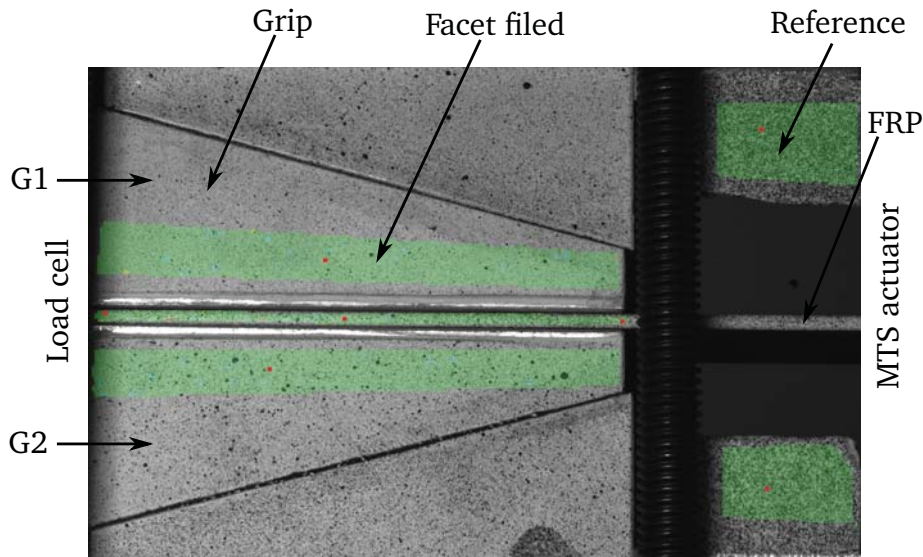
Figure D.3: Test setup with stochastic pattern. The FRP tendon is squeezed between two triangular grips, namely G1 and G2. The actuator pulls the tendon at constant speed. A load cell is installed opposite to the actuator to record the pullout force.

which are considered rigid. The displacement of the references is used to correct for rigid body movement. Displacement data is tracked for three positions along the length of the FRP to aluminum contact. One is to the right, one is in the center, and the third is at the left. Complete pullout is achieved when the left side of the contact starts to displace. This means that movement has occurred over the entire contact area.

D.4   Experimental results

Experimental pullout tests are done using the setup described in Fig. D.2. The length of the grips is l1 = 50 mm. The tilt angle is $\alpha = 15°$. It starts at a hight h2 = 3 mm, above the FRP. The left side of the grip has h1 = 15 mm. The FRP tendon is extending on both sides of the grip, and has the height h3 = 1.5 mm. The thickness of the grips and the FRP is 15 mm.

Aluminum tabs are glued to the end of the FRP, where the specimen is gripped by the tensile machine. The contact surfaces between the grips and the composite are cleaned before each test with a 50/50 solution of acetone and ethanol. A new specimen is used for each test.

This grip system should work in the following way: after the specimen is squeezed with a normal load, the grips and FRP should slide together. In this way the normal pressure increases, because the grips are forced closer together by the fixture. Grease is applied at the contact between the two aluminum surfaces, to achieve sliding of

the grips with the fixture, before the FRP is pulled out.

Two sets of grips are used. One set has a smooth surface, and the other set has a sandblasted surface. The roessughness measurements are done according to ISO standard [60], with a cutoff wavelength of $lc = 800\,\mu m$, and an evaluation length $ln = 5 * lc$. The arithmetic mean surface roughness of the smooth grips is $Ra = 1.027\,\mu m$ with a standard deviation of 10.7%. The maximum height of the roughness profile within the cutoff wavelength is $Rz = 8.414\,\mu m$. The sandblasted grips are rougher, with $Ra = 4.462\,\mu m$ and a standard deviation of 9.7%. $Rz = 38.04\,\mu m$.

The normal force takes values of 1, 4, 8 and 16 kN. Several tests are performed for each load level. The pullout speed varies between 0.5 and 1 mm/min. For longer tests the pullout speed is increased because of the limited storage space of the DIC system.
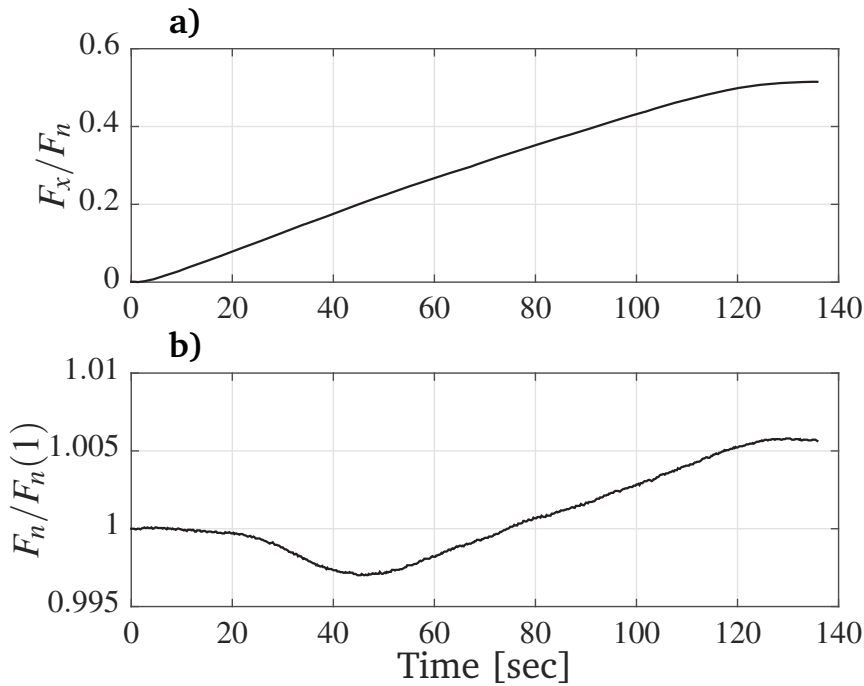

Figure D.4: Pullout test for a normal force $F_n = 16$ kN. F_x is the pullout force. F_x/F_n is the grip coefficient. In legend b, $F_n(1)$ is the initial normal force value, at the beginning of the test. A displacement of 0.8 mm/min is applied to the FRP. The grip surface is sandblasted.

The results help to explain the mechanics of the grip. The pullout process is complicated, and several plots are necessary to fully understand the process. Fig. D.4 shows the results of a test with a normal force $F_n = 16$ kN, and with sandblasted grips. F_x/F_n in legend a is the grip coefficient. The entire test duration is just under 140 sec. The grip coefficient is almost linear, and starts to flatten after approx. 110 sec. The maximum pullout is achieved after 120 sec. After this, it becomes clear that the FRP is being pulled out uniformly from the grip.

It is difficult to see that the initial change in F_x/F_n slope happens earlier than 110 sec. The results in legend b show the normalized clamping force, where $F_n(1)$ is the normal force at the beginning of the test. This test is successful, which means that the grips are sliding together with the FRP. This is visible due to the increase in $F_n/F_n(1)$ after the 47 sec mark. The change in $F_n/F_n(1)$ also marks a modification of the slope in legend a. It is this increase in $F_n/F_n(1)$ which takes F_x/F_n to a maximum value of 0.5. This is how the grip system is intended to function.
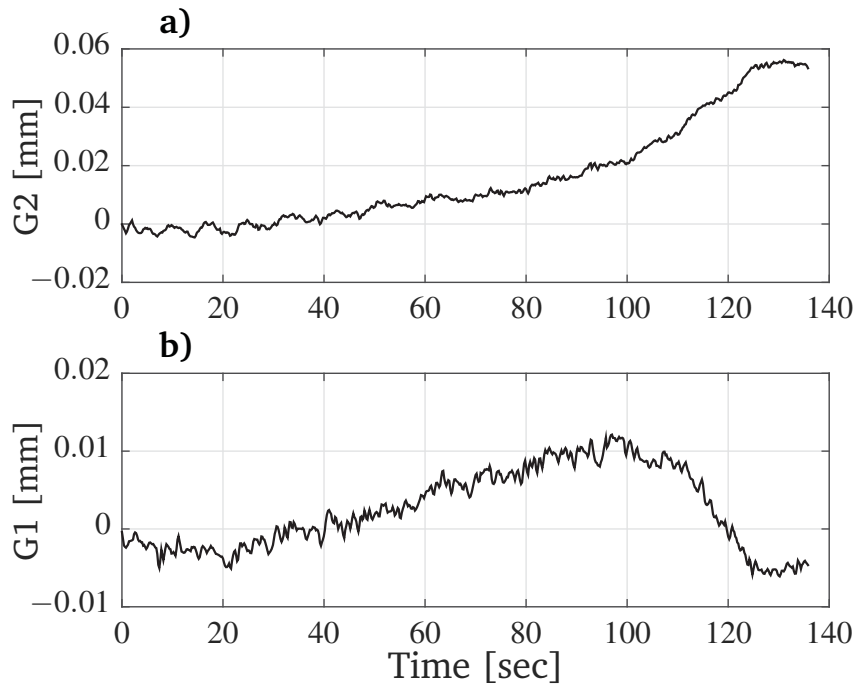

Figure D.5: Grip displacement for $F_n = 16$ kN. G1 in legend b is the displacement of the top grip. G2 in legend a is the displacement of the bottom grip. A displacement of $0.8\,mm/min$ is applied to the FRP. The grip surface is sandblasted.

In Fig. D.5 legend a, G2 is the displacement of the bottom grip. G1 in legend b is the displacement of the top grip. At the beginning of the test G2 does not move, but G1 displaces slightly backwards. This effect can be due to some misalignment between the test rig and the actuator. G1 starts to displace in positive direction, and after 47 sec the displacement of both grips is clearly positive. They continue to travel together until after 100 sec. F_n increases during this process. The change in G1 displacement between 100 and 125 sec means that the contact between the FRP and G1 has changed to slip. The negative G1 movement is compensated by a much higher displacement of G2. It is possible to see that the slope of F_x/F_n changes after 100 sec.

The contribution brought by the sliding of the grips is visible in Fig. D.6. The displacement of three reference points is tracked in legend a. P1 is the point at the

right end of the contact area, closest to displacement application. P3 is the point to the left, farthest from displacement application. When P3 starts to move, the grip fails. P1 displaces first, fallowed by P2 and P3. P2 is in the middle of the contact area, but it travels tighter together with P3. This shows the progressive onset of slip in the contact area, which propagates from the point closest to load application.
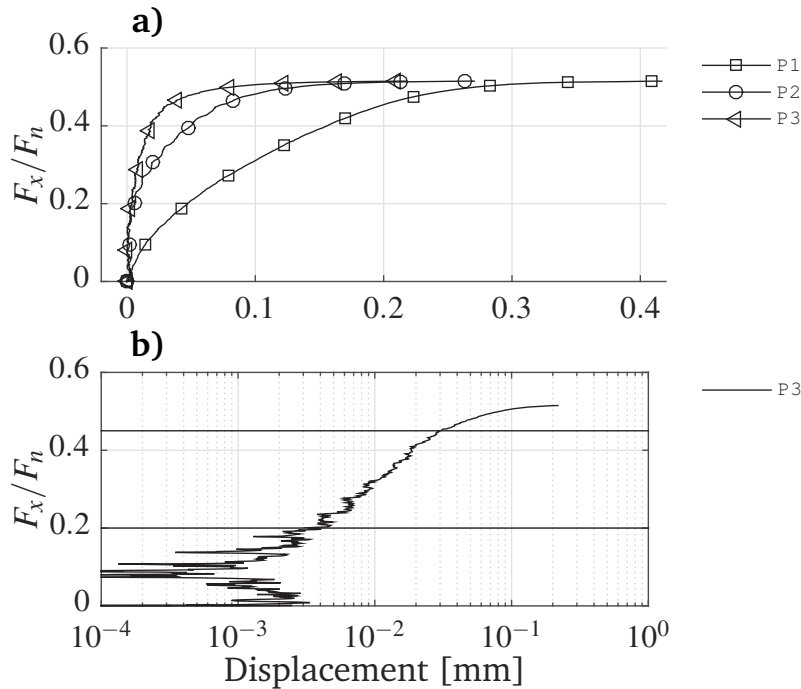

Figure D.6: FRP displacement for $F_n = 16$ kN. P1 is the point closest to displacement application. P3 is the point farthest from displacement application. P2 is in the middle of the contact area. The FRP is pulled with $0.8\,mm/min$. The grip surface is sandblasted. The linear part of the grip coefficient is between $F_x/F_n = 0.2$ and 0.45.

The initial displacement of P3 is magnified in legend b. The linear part of P3 is between $F_x/F_n = 0.2$ and 0.45. The result also corresponds with those above. At $F_x/F_n = 0.2$, the grips and the FRP start to displace, This increases the F_n value. Although small, this increase is sufficient to keep the FRP and grips from slipping, up to a ratio of $F_x/F_n = 0.45$. This is a 55 % increase of the grip coefficient. Above this value the FRP slides along the entire contact area.

Previous tests with rectangular grips have showed that F_x/F_n was equal to 0.25, which is the coefficient of friction between aluminum and the vinylester matrix FRP [1]. Obtaining $F_x/F_n = 0.45$ with the canted grips represents a 44 % increase. A displacement of 0.03 mm is necessary to obtain this increase. The initial displacement of the FRP takes place before the grips start to slide against the fixture. $F_x/F_n = 0.2$ is close to the value of $\mu = 0.25$.

Each point i Fig. D.7 represents one pullout test. A new specimen and cleaned

surfaces are used for each repetition. The normal force and its distribution at the start of each test is almost constant.
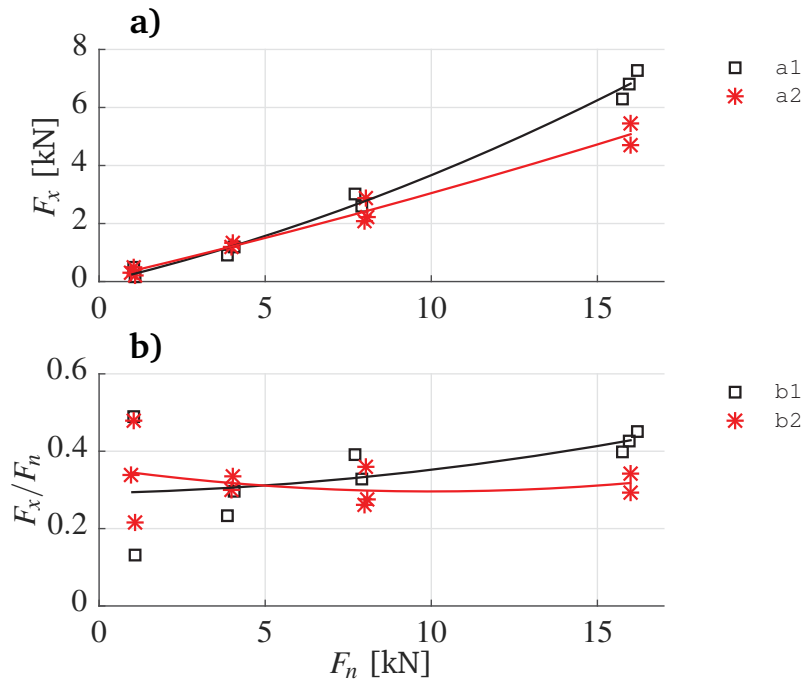

Figure D.7: Pullout force F_x and grip coefficient F_x/F_n for a normal force $F_n = 1, 4, 8$ and 16 kN. Results using the sandblasted grips are marked with lines a1 and b1. Results using the smooth grips are marked with lines a2 and b2.

The results with the smooth grips are marked with lines a2 and b2. Because there is a lot of scatter in the results, a second order polynomial is fitted to the data. The pullout force increases almost linearly from 0.36 kN to 5 kN. The grip coefficient in legend b2 is a more accurate tool for understanding the behavior of the grip. The largest scatter is obtained for $F_n = 1$ kN. At this low value, the initial conditions have a big impact on the results. This behavior has been observed for tests with rectangular grips as well [1]. Increasing F_n results in less scatter. The polynomial fit of F_x/F_n varies very little, dropping from an initial value of 0.34 to 0.32. This almost constant value shows that there is no significant improvement with the v-shaped grips when using smooth surfaces. The FRP slips out before the grips start to slide against the fixture and increase F_n.

Superior results are obtained using sandblasted grips, which are marked by lines a1 and b1. The pullout force F_x for line a1 is initially lower than a2 for F_n between 1 and 4 kN. Line b1 is as well lower than b2 in this interval. The reason is that at low F_n values, the real contact area achieved with the sandblasted grips is lower than that obtained with the smooth grips. A high pressure is necessary to push the high metal asperities in contact with the FRP. The contact pressure for $F_n = 4$ kN is 5.33

MPa. This increases to 10.66 MPa for $F_n = 8$ kN, and 21.33 MPa for $F_n = 16$ kN.

Clearly better results are obtained for $F_n = 16$ kN. The polynomial F_x/F_n fit, line b1, increases from an initial value of 0.29 up to 0.43. Increasing the normal force results in a better grip, and this increases the pullout. At $F_n = 16$ kN the difference is clear. The contact friction between the FRP and the aluminum grips is sufficient to counteract the friction with the fixture. The small sliding in positive x direction of the grips increases F_n enough to retain the static grips to FRP contact. The maximum average F_x/F_n increase between b1 and b2 is 26%. If we consider previous results with rectangular grips, where F_x/F_n is 0.25, the increase is 42%.
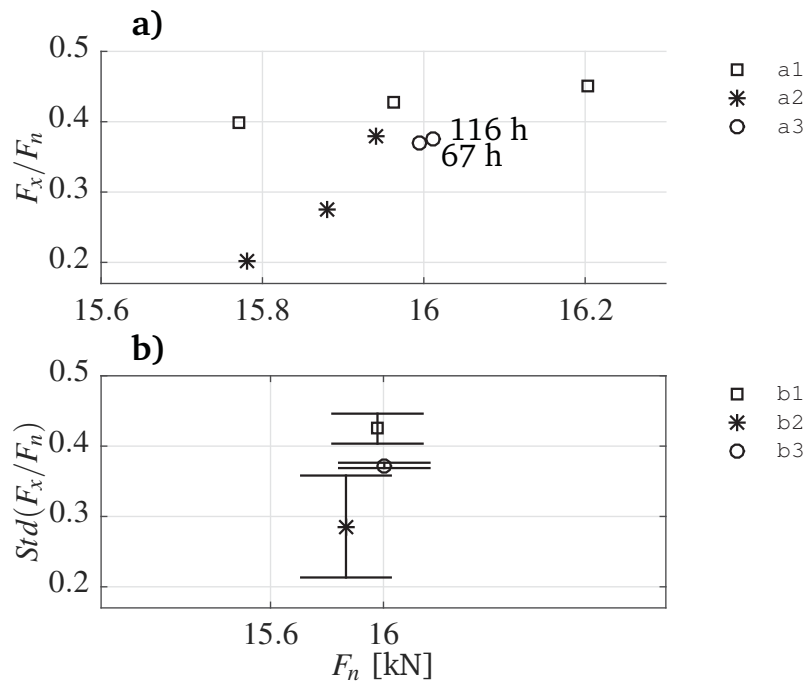

Figure D.8: Grip coefficient F_x/F_n and standard deviation $Std(F_x/F_n)$ for $F_n = 16$ kN. a1 represents results where a new specimen is used every time. a2 are results obtained by gripping and pulling the same specimen, without cleaning the grips. a3 are creep tests after 67 and 116 hours. Their standard deviation is given in legend b. All results are obtained using sandblasted grips.

Additional tests are done with sandblasted grips at the highest normal force. These results are displayed in Fig. D.8. The scatter of F_x/F_n, line a1, is low when a new specimen is used for each test, combined with cleaning the grips every time. F_x/F_n varies from 0.39 to 0.45. This steady increase in grip efficiency demonstrates that at the grip system functions as expected. Clamping and pulling at the same specimen without cleaning the grips, line a2, results in more scatter, see a2. Matrix material gets deposited on the grips when the FRP is pulled. This fills up the asperities and reduces μ. The reduced contact friction between the FRP and the

grips is not sufficient to pickup the grips, and the system does not function as expected.

Two creep tests are done. One after waiting 67 h, and the second after waiting 116 h. They are marked with line a3. Analysis of F_n versus time shows no increase for the 67 h test. This means that the grips did not slide against the fixture. In the 116 h wait test, F_n increased twice , with a drop in the middle. The F_x/F_n value is taken at the end of the first F_n peak, even if it continued to increase at a slower rate. Keeping the grips pressed for a long time seems to increase the friction between the metal parts more than that between the metal and FRP. Changing the type of lubricant used between the metal parts could mitigate this problem.

D.5   Analytic results

F_T is the force equilibrium calculated at the contact area between the wedge and fixture. The coefficient of friction for lubricated aluminum to aluminum is $\mu = 0.3$.
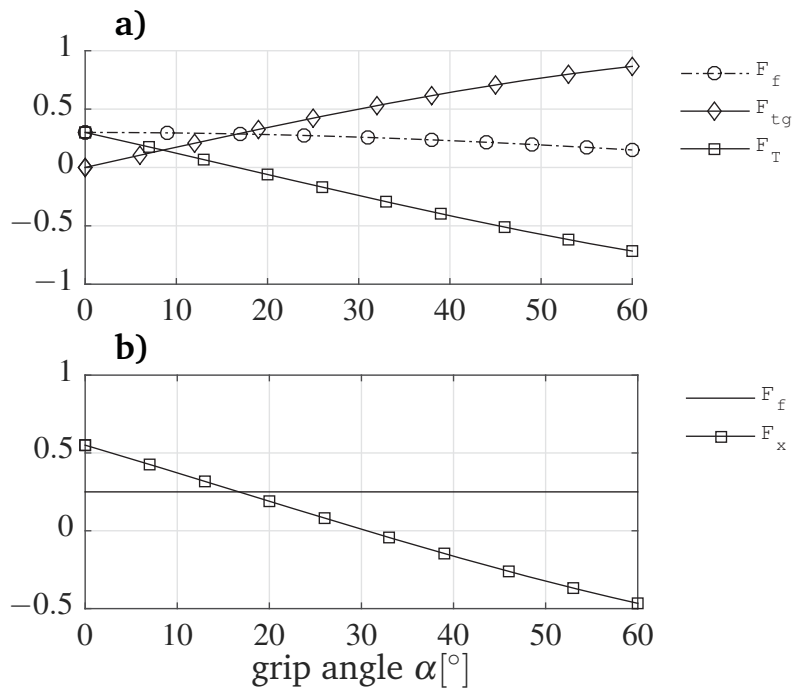

Figure D.9: Force equilibrium. a) The Al to Al contact between the grips and fixture with $\mu = 0.3$. F_f is the friction force, F_{tg} the tangential force, and F_T is the force equilibrium. b) The Al to FRP contact with $\mu = 0.25$. F_f is the contact friction force and F_x is the available pullout force.

F_f is the friction force and F_{tg} is the tangential component of the force applied to the grip. In Fig. D.9 legend a, unity force is applied to the grip. The grip angle α takes values between 0° and 60°. F_{tg} increases with increasing α, while F_f slowly

decreases from a maximum of 0.3. The positive part of F_T means that the grip does not slide back from the fixture. As α increases, so does F_{tg}. After $\alpha = 16°$, F_T becomes negative, which means that the grips will slide back from the fixture, unless they are kept in place due to the contact with the FRP. This means that for these frictional properties, the maximum grip angle is $\alpha = 16°$. The friction force at the contact between the grips and the FRP is shown in Fig. D.9 legend b. It is calculated with a μ for Al to FRP of 0.25. F_x is the pullout force, and is the difference between F_T and F_f. If the force equilibrium at the Al to Al contact is not enough to keep the grips in place, the available F_x decreases. Above $\alpha = 30°$ the grips will slide completely out. From this calculation, and with $\alpha = 15°$, the available grip coefficient is 0.28. Reducing α increases the grip coefficient.
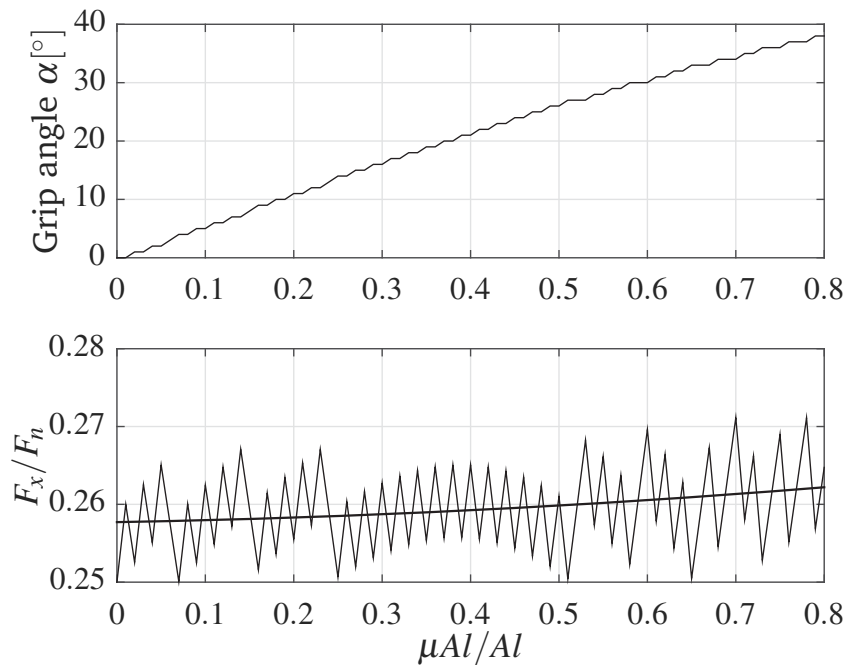

Figure D.10: Parametric analysis. a) The influence of friction at the contact between the grips and the fixture, μ Al/Al, and the grip angle α. b) The grip coefficient F_x/F_n. μ Al/FRP is 0.25.

The parametric analysis in Fig. D.10 legend a shows what is the correlation between μ at the contact between the grips and the fixture and the α value for which $F_x = 0$. It is clear that a higher μ allows us to increase the grip angle. This result is counter-intuitive, but shows that more friction is better for the pullout force. The minimum grip coefficient F_x/F_n increases slowly with increasing friction, as shown in legend b. For a certain combination of μ, F_x/F_n can be further increased by choosing a grip angle α smaller than the threshold.

D.6 FE results

A 2D finite element model is created, which has all the components presented in Fig. D.2. There are four contact areas, two between the grips and the fixture, and two between the grips and the FRP. The purpose of the model is to simulate the behavior of the grips, and to show the influence of the grip angle, friction parameters and boundary conditions.

The bodies are meshed with 8 node solid elements in Ansys 15.0, under a plane stress with thickness condition. 3-node contact elements are meshed where the components meet. The FRP is the contact surface and the grips are the target. The solver is nonlinear. The initial contact is closed, and inter-penetration effects are excluded.

Because the FRP is unidirectional, and it only slides in one direction, isotropic friction is used. When contact changes from stick to slip, there is a change from the static coefficient of friction μ_s, to the dynamic coefficient μ_d. The ratio between static and dynamic friction is μ_s/μ_d.

The grips are modeled as isotropic materials, with $E_x = 69$ GPa and $\nu_{xy} = 0.33$ for aluminum. The FRP is modeled as an orthotropic material. Transverse elastic modulus $E_y = 9.51$ GPa is calculated for the FRP. This is done using a micro-mechanics approach based on fiber volume fraction and material properties of the fibers and matrix provided by the manufacturer. The shear modulus in principal direction is $G_{xy} = G_{xz} = 6.23$ GPa, and the transverse shear modulus is $G_{yz} = 2.59$ GPa. The major Poisson's ratios are $\nu_{xy} = \nu_{xz} = 0.29$ and the minor Poisson's ratio is $\nu_{yz} = 0.32$. Five longitudinal tensile tests have resulted in a longitudinal elastic modulus $E_x = 41.88$ GPa.

Two load steps used. In the first, F_n is applied to the top fixture, as a uniformly distributed pressure. In the second, displacement is applied to the right side of the FRP in positive x direction. The reaction force F_x is then measured.

D.6.1 Mesh discretization

The top fixture is constrained in x direction, but is allowed to slide vertically. The constraint is applied at the top line. The bottom fixture is constrained in all directions. The constraint is applied at the bottom line. The contact friction stress is calculated for each contact node pair as the normal pressure times μ. For this reason it is important to achieve a stable solution for the pressure distribution along the contact area.

The pressure distribution at the contact between the aluminum grip and the FRP is calculated for several mesh discretizations. $\mu_{s1} = 0.25$ for the Al to FRP contact,
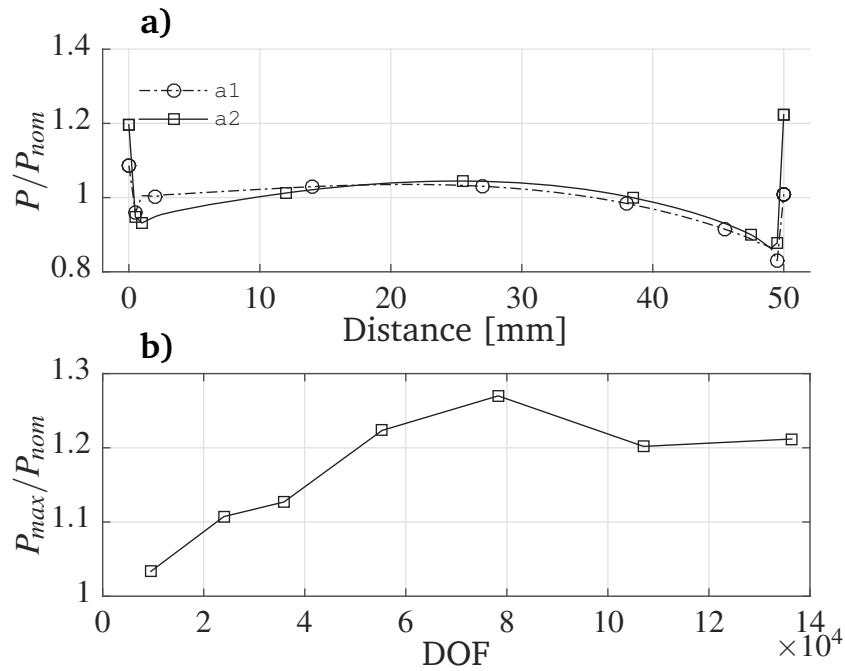
Figure D.11: Pressure distribution at the contact between the grips and the FRP. Line a1 corresponds to 9530 DOF, and line a2 corresponds to 55302 DOF. The pressure P and the maximum pressure P_{max} are normalized with the nominal applied pressure $P_{nom} = 5.33$ MPa. For this aluminum to FRP contact, the static coefficient of friction is $\mu_{s1} = 0.25$. $\mu_{s2} = 0.3$ is used at the contact between the grip and fixture. The contact length is 50 mm, and $\mu_s/\mu_d = 1.2$. $\alpha = 15°$.

and $\mu_{s2} = 0.3$ for the Al to Al contact. $\mu_s/\mu_d = 1.2$.

The solution in Fig. D.11 line a1 is obtained using the coarsest mesh, with only 9530 DOF. The pressure distribution is skewed towards the right side. This is because of the grip is tilted with $\alpha = 15°$. In Fig. D.11 line a2 the number of elements is increased to 55302 DOF. This results in a more evenly distributed pressure, but with higher maximum values at the extremities. The maximum value increases faster at the left side that the right side value, when the DOF increases. P_{max} is the maximum contact pressure at 50 mm. P_{nom} is the nominal applied pressure. P_{max}/P_{nom} in legend b increases, after which it remains in the 1.2 to 1.27 band. Keeping the size of the model to a minimum means that a number of 55302 DOF is used in all subsequent calculations.

D.6.2 Pullout force

Previous analysis for a double clamp with rectangular grips [2] shows that good agreement is achieved between FE and experimental results under certain conditions. These consist of using a slightly different coefficient of friction between

the two aluminum to FRP contact areas. This model is also capable of simulating imperfect contact, by introducing $\mu = 0$ in some of the contact pairs. Based on previous experience, the initial friction coefficients are $\mu_{s1} = 0.25$ and $\mu_{s2} = 0.2$ for the aluminum to FRP contact areas, and $\mu_{s3} = 0.3$ for the aluminum to aluminum contact. The drop in friction between static and dynamic regime is $\mu_s/\mu_d = 1.2$.

The influence of the friction parameters over the grip coefficient F_x/F_n is shown in Fig. D.12. Full contact is used for the result in line a1. F_x/F_n and the displacement needed to achieve complete pullout is the largest of all the results. The nonlinear response of the system is caused by the gradual transition between stick and slip in the contact area. The maximum value of $F_x/F_n = 0.38$ is obtained before complete pullout. After this value, F_x/F_n drops to a stable value of 0.37, which is higher than the experimental results in Fig. ?? line b2.
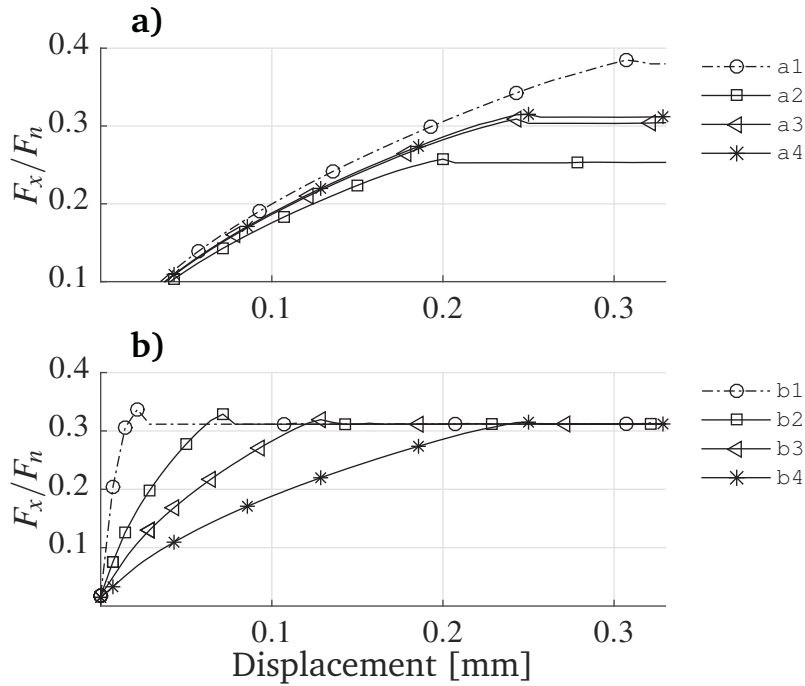

Figure D.12: Grip coefficient F_x/F_n. The pullout force F_x is obtained by applying displacement to the FRP in positive x-direction. For the results in legend a, the normal force F_n is 16 kN. The static coefficient of friction for the contact between the top grip and the FRP is $\mu_{s1} = 0.25$. The coefficient of friction at the contact between the lower grip and the FRP is μ_{s2}, and the reduction in contact area takes the following values: a1) $\mu_{s2} = 0.2$, $a = 0\%$, a2) $\mu_{s2} = 0.2$, $a = 33\%$, a3) $\mu_{s2} = 0.2$, $a = 20\%$, a4) $\mu_{s2} = 0.22$, $a = 20\%$. Legend b: F_n effect. The friction properties are $\mu_{s1} = 0.25$, $\mu_{s2} = 0.22$ and $a = 20\%$. b1) $F_n = 1$ kN, b2) $F_n = 4$ kN, b3) $F_n = 8$ kN, b4) $F_n = 16$ kN. The aluminum to aluminum friction is $\mu_{s3} = 0.3$. $\mu_s/\mu_d = 1.2$. The grip angle is $\alpha = 15°$.

Parametric analysis [2] shows that the reduction of the contact area efficiently

reduces the grip coefficient. The area reduction for line a2 is 33%. The pullout response of the system is less stiff, and the displacement necessary to achieve pullout is also reduced. F_x/F_n drops to 0.25. The exact result is obtained by reducing the contact with $a = 20\%$, and by increasing the friction to $\mu_{s2} = 0.22$.

The normal force effect is shown in legend b. F_n is increased from 1 to 16 kN. F_x/F_n is almost linear for b1, where $F_n = 1$ kN. This is because the transition from stick to slip is more abrupt, and happens very fast. For this reason, there is a large drop from $F_{xmax}/F_n = 0.33$ to $F_x/F_n = 0.31$. Increasing F_n produces a more nonlinear result. The displacement necessary for pullout increases, and the drop between static and dynamic friction is reduced.

The friction parameters used in Fig. D.12 legend a are chosen using a normal force $F_n = 16$ kN. It is necessary to compare the accuracy of the FE model at different F_n values against experimentally obtained results.
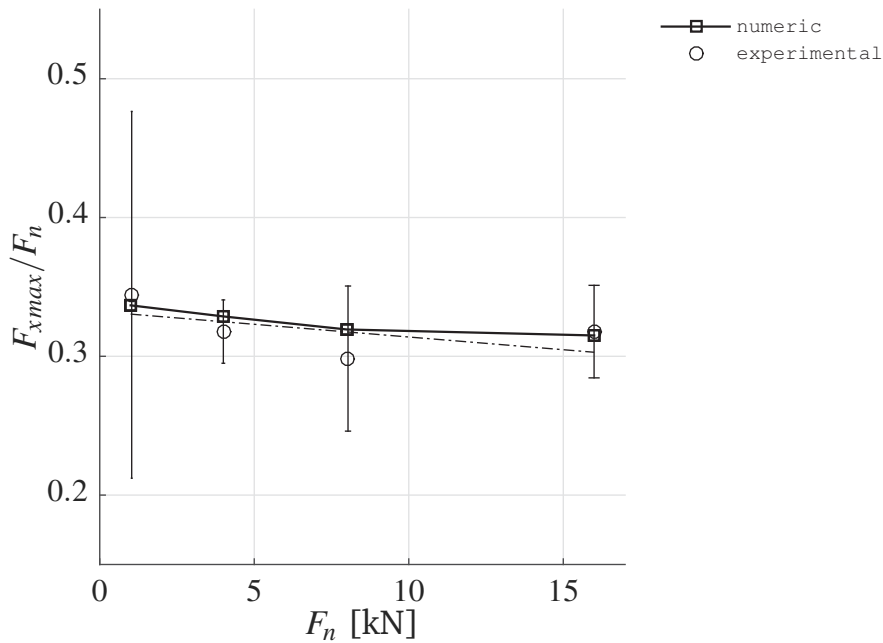

Figure D.13: Experimental and numeric results. Maximum grip coefficient F_{xmax}/F_n as a function of the normal force F_n. The tilt angle is $\alpha = 15°$. $\mu_{s1} = 0.25$, $\mu_{s2} = 0.22$, $\mu_{s3} = 0.3$, $\mu_s/\mu_d = 1.2$, $a = 20\%$.

The experimental results in Fig. D.13 are obtained using grips of the same dimension as the FE model. Because of the large scatter, a first order polynomial is used to show their trend. The numerically obtained values of F_{xmax}/F_n correlate well for the entire F_n range. The important result is the gradual decrease of F_{xmax}/F_n, which is outlined by both results. This means that the FE model is accurate, no matter the F_n value.

D.6.3   Grip angle

The parameter under investigation in Fig. D.14 is the grip angle α. Three different models are compared, with α values of 3°, 8° and 20°. Based on previous analysis, the coefficients of friction at the contact between the grips and the FRP are $\mu_{s1} = 0.25$ and $\mu_{s2} = 0.22$. A 20% reduction in contact area is used. The normal force in all cases is $F_n = 16$ kN.
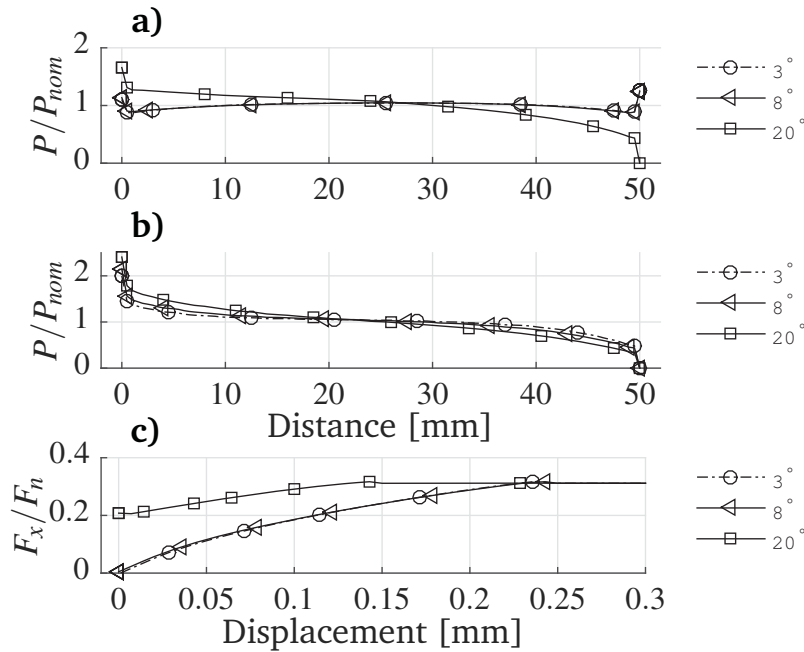

Figure D.14: Grip angle α effect. Three α values are compared, namely 3°, 8° and 20°. The pressure P and the pullout force F_x are normalized with the nominal applied pressure P_{nom} and normal force $F_n = 16$ kN. Two load steps are used. In the first pressure is applied to the fixture, and the contact pressure distribution is given in legend a. In the second load step, displacement is applied to the right end of the FRP. The pressure distribution just before pullout is given in legend b. The grip coefficient F_x/F_n is given in legend c. $\mu_{s1} = 0.25$, $\mu_{s2} = 0.22$, $\mu_{s3} = 0.3$ and the contact area reduction is $a = 20\%$. The contact length is 50 mm.

There are two important time-steps for the normalized contact pressure P/P_{nom}. The first is after P_{nom} is applied. The second is just before complete pullout. For low α values the P/P_{nom} distribution is virtually unaffected, as shown in Fig. D.14 legend a. Increasing to $\alpha = 20°$ results in an unbalanced distribution, with the maximum at a distance of 0 mm. This means that the grip did slide back from the fixture, coupled with a small rotation.

The pressure distribution just before pullout is rotated, with the maximum at the right end of the grip. This is given in Fig. D.14 legend b. It shows that P/P_{nom} shifts toward the right end of the grip, due to the increase of α . This means that it is more

probable to exceed the compressive strength of the FRP when using higher α values.

The maximum F_x/F_n in legend c is independent of the grip angle. The analytic solution shows that there is a maximum α value, before the grips slide in negative x direction. $\alpha = 20°$ is above the threshold, and the negative displacement of the grips results in a pre-tension of the FRP tendon.

D.6.4 Grip to fixture friction

The effect of changing μ at the contact between the grip and the fixture is shown in Fig. D.15. The grip angle is kept constant at $\alpha = 10°$. The pressure distribution after the first load step is given in Fig. D.15 legend a.

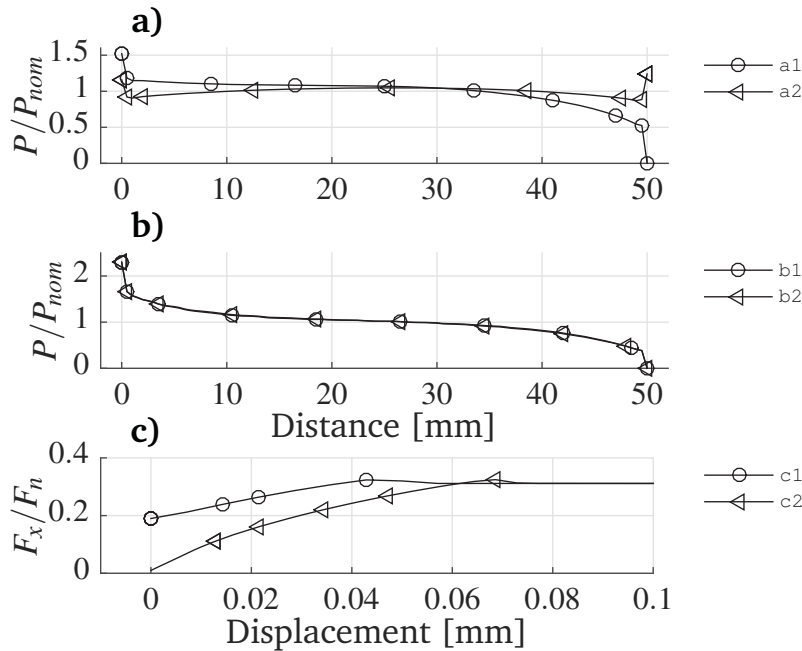**Figure D.15:** Grip to fixture friction. a) After P_{nom} application. b) Before pullout. The coefficient of friction for line 1 is $\mu = 0.1$. For line 2 is $\mu = 0.3$. For the aluminum to FRP contact $\mu_{s1} = 0.25$, $\mu_{s2} = 0.22$, and contact area reduction is $a = 20\%$. The contact length is 50 mm. The grip angle is $\alpha = 10°$.

When $\mu = 0.3$, see line a2, P/P_{nom} is symmetrically distributed across the contact area. Reducing to a very low friction, with $\mu = 0.1$ for line a1, produces a shift in the pressure profile. P/P_{nom} increases at the left side of the contact, from 1.15 to 1.52. It becomes zero at the right side. The maximum F_x/F_n in legend c is not influenced by μ. This is because the pressure profile just before pullout is the same, as shown in legend b. The only visible effect is the initial increase of F_x/F_n in line c1, where $\mu = 0.1$. At low friction, the grips slide back from the fixture, and pre-tension

the FRP tendon. Because of this, the displacement required to achieve pullout is significantly reduced.

D.6.5   Boundary conditions

Until now, all results are obtained using the same boundary conditions. The fixture consists of two parts, one above the grips, and one below. Pressure is applied to the upper fixture, and the top line is constrained in x-direction. The bottom line of the fixture below the grips is constrained in all directions. These conditions replicate the experimental setup conditions, with the results plotted in Fig. D.16 line 1.
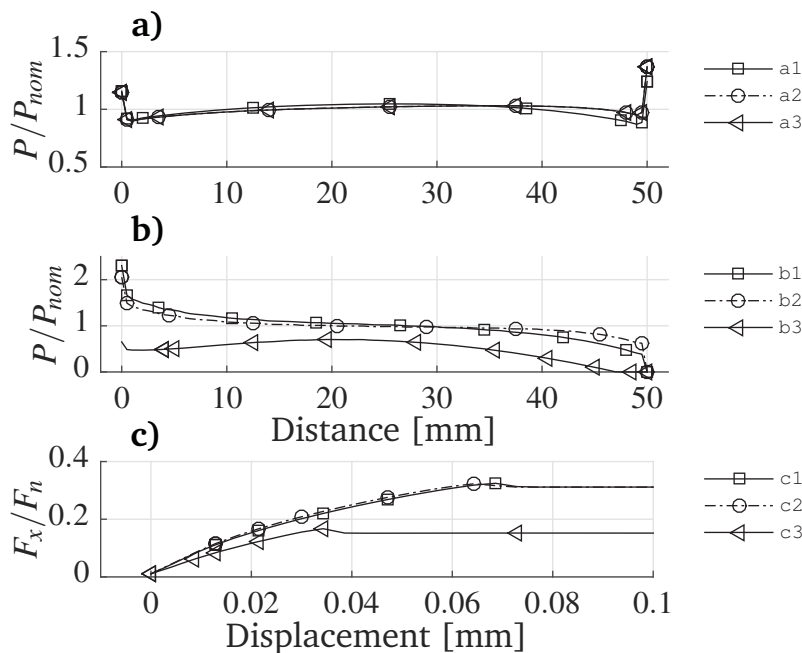

Figure D.16: Boundary conditions influence. a) After P_{nom} application. b) Before pullout. For line 1 the top line of the top fixture is constrained with $ux = 0$. For line 2 the entire top fixture is constrained with $ux = 0$. For line 3 the entire top fixture is constrained with $ux, uy = 0$. For the aluminum to FRP contact $\mu_{s1} = 0.25$, $\mu_{s2} = 0.22$, and contact area reduction is $a = 20\%$. At the grip to fixture contact $\mu_{s2} = 0.3$. The contact length is 50 mm. The grip angle is $\alpha = 10°$.

Stiffening the top fixture is achieved by further constraining the lateral faces of the top fixture with $ux = 0$. The initial pressure P/P_{nom} shows a shift towards the right end of the contact area, as shown in legend a. This remains true when, just before pullout in legend b, the pressure transfer between the right and left end of the contact area is reduced. Although there is no drop in the maximum F_x/F_n value between c1 and c2, pullout is achieved with a shorter displacement in the case of c2.

The most drastic effect is obtained when the entire top and bottom fixtures are constrained in all directions, in load-step 2. P/P_{nom} in line b3 is drastically reduced,

and results in a 51 % drop in F_x/F_n. This effect is explained by the inability of the grip to slightly rotate during pullout. This rotation increases the pressure towards the left of the contact area, improving the grip performance. This result is important, because it shows the high sensitivity to boundary conditions. It is possible that the fixture will be much stiffer when applied in a different configuration, for industrial purposes. It is due to the practicality of the experimental test rig that this special setup was chosen.

It is necessary to make sure that the grip can deliver the same performance in a different configuration, which is more likely to exist for an industrial application. Two configurations are compared. For line 1 in Fig. D.17, P_{nom} is applied to the top fixture in load-step 1. Positive x displacement is applied to the FRP tendon in load-step 2. For line 2, the fixture is completely constrained in load-step 1. At the same time, positive x displacement is applied to the grips. In the second load-step further positive x displacement is applied to the FRP tendon.

In the case where normal pressure is applied to the grip, the profile of line a1 has an almost constant value of 1. During pullout, represented by line b1, P/P_{nom} rotates. The maximal value is achieved at the left side of the contact distance.

The results are different if the grips are pulled through a fix fixture. First, the contact pressure is higher, see line a2. At pullout, P/P_{nom} is much more constant over the entire contact length, see line b2. F_x/F_n for line c2 is slightly higher than for line c1. But the biggest difference is that the displacement required for pullout did increase with 23 %. This proves that the grip can function in a variety of conditions, and opens a lot of possibilities for industrial applications.

D.7   Conclusions

The efficiency of a new double clamp design with flat faces is investigated using experimental and numerical results. The grips are v-shaped, and are contained within a fixture of the same profile. The FRP is squeezed in between the grips. The experimental results are used to measure the efficiency of the grip, which is the pullout force divided with the normal force. They provide input for a 2D finite element model, which is used to conduct a detailed parametric analysis.

Experimental results show that sandblasted grips provide a high enough coefficient of friction, so that the grips slide together with the FRP tendon. This provides an increase of the friction force, which results in a superior grip coefficient. The increase of the grip coefficient between smooth and sandblasted grips is 26 %. This is a better result, than in the case of rectangular grips [1]. Numerical results show that the grip angle necessary to achieve this can be very small, which in turn means
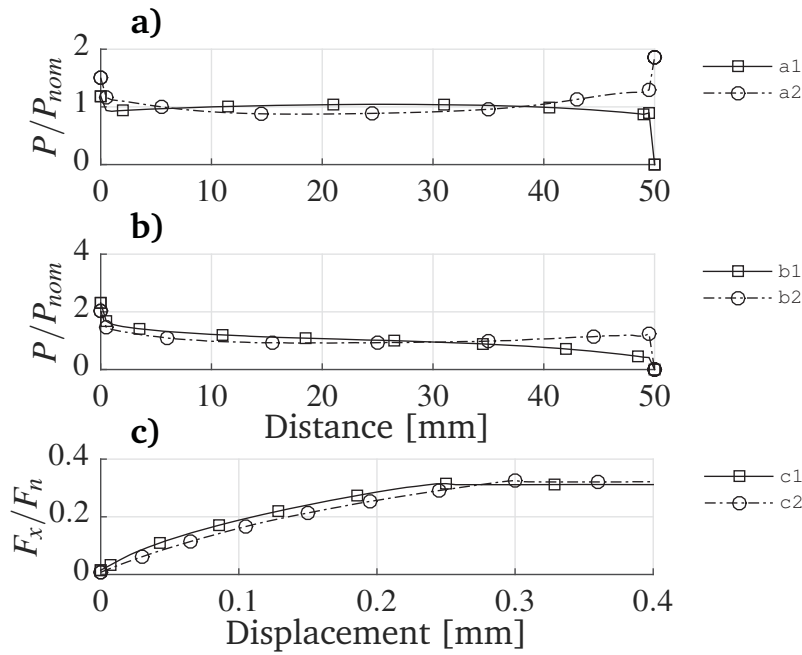
Figure D.17: Wedge pull. a) After P_{nom} application. b) Before pullout. Boundary conditions line 1: top fixture constrained with $ux = 0$ and $F_n = 4$ kN; line 2: top and bottom fixture constrained in all directions, while displacement is applied to the grips in positive x-direction. For the aluminum to FRP contact $\mu_{s1} = 0.25$, $\mu_{s2} = 0.22$, and contact area reduction is $a = 20\%$. At the grip to fixture contact $\mu_{s2} = 0.3$. The contact length is 50 mm. The grip angle is $\alpha = 15°$.

that the v-grips will be relatively small. A smaller grip angle also produces a smaller increase in contact pressure, which is good in preventing the crushing of the FRP. Both analytic and numerical solutions show that the coefficient of friction at the contact between the grips and the fixture has to be high. This prevents the grips from sliding back from the fixture. It also causes some pre-tension in the FRP, and does not result in a higher grip coefficient.

The system is shown to work in a variety of configurations and boundary conditions. The grip coefficient is the same,. This versatility makes it easy for the grip to be used in a variety of applications. This, combined with the high efficiency, makes this grip system an ideal solution for transferring loads through friction.

Acknowledgements

Bibliography

[1] A. Costache, K. Glejbøl, I. M. Sivebæk, and C. Berggreen. "Friction Joint Between Basalt-Reinforced Composite and Aluminum". *Tribology Letters* 59.2 (June 2015), p. 30.

[2] A. Costache, K. Glejbøl, I. M. Sivebæk, and C. Berggreen. "Numerical Investigation of Friction Joint between Basalt Reinforced Composite and Aluminum". *Submitted to Proceedings of the IMechE, Part J: Journal of Engineering Tribology* (2015).

[3] A. Costache, K. Glejbøl, I. M. Sivebæk, and C. Berggreen. "Stress Analysis of a Friction Joint between Basalt Reinforced Composite and Aluminum". *To be submitted* (2015).

[4] A. Costache, K. Glejbøl, I. M. Sivebæk, and C. Berggreen. "Improved friction joint with v-shaped grips". *Submitted to International Journal of Mechanical Sciences* (2015).

[5] A. Costache, K. Anyfantis, and C. Berggreen. *On the Analysis of a Contact Friction Composite-to-Metal Joint*. Montreal, 2013.

[6] A. Costache, K. Glejbøl, I. M. Sivebæk, and C. Berggreen. *Experimental Investigation of a Basalt Fiber reinforced Composite to Metal Joint*. Madrid, 2015.

[7] "Fossils fuel the future". *Petroleum Economist* 78.5 (2011).

[8] United States Energy Infromation Administration. *International Energy Outlook 2013*. Tech. rep. 2013.

[9] K. Mohaddes. "Econometric Modelling of World Oil Supplies: Terminal Price and the Time to Depletion" (2012), pp. 162–193.

[10] A. Regalado. "Tapping a Deep, 'Pre-Salt' Bounty." *Science* 330.6009 (2010).

[11] J. Redden. "Pre-salt to propel Brazil toward the top". *World Oil* 233.8 (2012).

[12] EMA and IMS. *Floating Production Systems*. Tech. rep. July. Energy Maritime Associates Pte Ltd, 2013.

[13] G. Estrella. "Pre-salt production development in Brazil". *First Magazine* (2011).

[14] J. Clevelario, F. Pires, C. Barros, and T. Sheldrake. "Flexible Pipe Systems Configurations for the Pre-Salt Area". *29th International Conference on Ocean, Offshore and Arctic Engineering: Volume 5, Parts A and B*. Vol. 5. ASME, 2010, pp. 457–464.

[15]   R. F. Solano, F. B. De Azevedo, and E. Oazen. "Design Challenges of Gas Export Pipelines for Pre-Salt Area Offshore Brazil". *Volume 4A: Pipeline and Riser Technology*. Vol. 4. ASME, June 2013, V04AT04A009.

[16]   American Petroleum Institute. *American Petroleum Institute - API Specification 17J*. 2014.

[17]   N. J. R. Nielsen, K. Glejbøl, and V. Kulakov. "Innovative un-bonded flexible pipe design with hybrid CFRP / metal armour ." *Technology* (2001), pp. 1–10.

[18]   J. Rytter, G. Portnov, and V. Kulakov. "Anchoring and a Load Transfer Technique in Uniaxial Tension of Unidirectional High-Strength Composites". *Mechanics of Composite Materials* 41.3 (May 2005), pp. 217–228.

[19]   J. W. Schmidt, A. Bennitz, B. Täljsten, P. Goltermann, and H. Pedersen. "Mechanical anchorage of FRP tendons – A literature review". *Construction and Building Materials* 32 (July 2012), pp. 110–121.

[20]   C. Burgoyne. "Structural use of parafil ropes". *Construction and Building Materials* 1.1 (Mar. 1987), pp. 3–13.

[21]   E. Y. Sayed-Ahmed and N. G. Shrive. "A new steel anchorage system for post-tensioning applications using carbon fibre reinforced plastic tendons". *Canadian Journal of Civil Engineering* 25.1 (1998), pp. 113–127.

[22]   A. Al-Mayah, K. A. Soudki, and A. Plumtree. "Experimental and Analytical Investigation of a Stainless Steel Anchorage for CFRP Prestressing Tendons". *PCI Journal* 46.2 (Mar. 2001), pp. 88–100.

[23]   E. Y. Sayed-Ahmed. "Single- and multi-strand steel anchorage systems for CFRP tendons / stays". *Proceedings, Annual Conference - Canadian Society for Civil Engineering* 2002 (2002), pp. 1381–1390.

[24]   A. Al-Mayah, K. Soudki, and A. Plumtree. "Development and Assessment of a New CFRP Rod–Anchor System for Prestressed Concrete". *Applied Composite Materials* 13.5 (Aug. 2006), pp. 321–334.

[25]   G. G. Portnov, V. L. Kulakov, and A. K. Arnautov. "A refined stress-strain analysis in the load transfer zone of flat specimens of high-strength unidirectional composites in uniaxial tension 1. Theoretical analysis". *Mechanics of Composite Materials* 42.6 (Nov. 2006), pp. 547–554.

[26]   G. G. Portnov, V. L. Kulakov, and A. K. Arnautov. "A refined stress-strain analysis in the load transfer zone of flat specimens of high-strength unidirectional composites in uniaxial tension 2. Finite-element parametric analysis". *Mechanics of Composite Materials* 43.1 (Jan. 2007), pp. 29–40.

[27]   S. L. Burtscher. "Wedge Anchorage for CFRP Strips". *Journal of Composites for Construction* 12.4 (Aug. 2008), pp. 446–453.

[28]   J. Schön. "Coefficient of friction for aluminum in contact with a carbon fiber epoxy composite". *Tribology International* 37.5 (May 2004), pp. 395–404.

[29]   V. L. Popov. *Contact mechanics and friction : physical principles and applications*. Springer, 2010.

[30]   ASM. *ASM handbook*. ASM International, 1990.

[31]   F. Bowden. *The friction and lubrication of solids*. Clarendon, 2001.

[32]   B. Bhushan. *Introduction to tribology*. Wiley, 2013.

[33]   C. M. Pooley and D. Tabor. "FRICTION AND MOLECULAR STRUCTURE - BEHAVIOR OF SOME THERMOPLASTICS". *Proceedings of the Royal Society of London Series A-mathematical and Physical Sciences* 329.1578 (1972).

[34]   J. F. Archard. "Elastic Deformation and the Laws of Friction". *Proceedings of the Royal Society A: Mathematical, Physical and Engineering Sciences* 243.1233 (Dec. 1957), pp. 190–205.

[35]   R. Bowers. "Coefficient of Friction of High Polymers as a Function of Pressure". *Journal of Applied Physics* 42.12 (1971).

[36]   GOM. *Aramis*.

[37]   O. Ben-David and J. Fineberg. "Static friction coefficient is not a material constant". *Physical Review Letters* 106.June (2011), pp. 1–4.

[38]   M. Comninou. "Stress Singularity at a Sharp Edge in Contact Problems with Friction". *Zeitschrift für angewandte Mathematik und Physik ZAMP* 27.4 (1976), pp. 493–499.

[39]   J. Dundurs and M. S. Lee. "Stress concentration at a sharp edge in contact problems". *Journal of Elasticity* 2.2 (June 1972), pp. 109–112.

[40]   H. Nordin. *Strengthening structures with externally prestressed tendons Strengthening structures with Literature review*. Tech. rep. Lulea University of Technology, 2005.

[41]   R. Mitchell. "High-strength end fittings for FRP rod and rope". *Journal of the Engineering Mechanics Division* 100.NEM4 (1974), pp. 687–706.

[42]   F. S. Rostasy and B. Kepp. *Verhalten dynamisch beanspruchter GFK-Spannglieder: Abschlussbericht zum Forschungsvorhaben ; Untersuchung im Auftr. der DFG (Az.: Ro 288/18-1)*. Institut für Baustoffe, Massivbau und Brandschutz, 1986.

[43]   F. Rostásy. "Draft Guidelines for the Acceptance Testing of FRP Posttensioning Tendons". *Journal of Composites for Construction* 2.1 (Feb. 1998), pp. 2–6.

[44] F. S. Rostasy. "New approach in the already published recommendations for anchorage assembly". *Proceedings of the Congress of the Federation Internationale De La Precontrainte* (1982), pp. 95–98.

[45] M. Taha. "New concrete anchors for carbon fiber-reinforced polymer post-tensioning tendons - Part 1: State-of-the-art review/design". *ACI Structural Journal* 100.1 (2003), pp. 86–95.

[46] M. Taha. "New concrete anchors for carbon fiber-reinforced polymer post-tensioning tendons - part 2: Development/experimental investigation". *ACI Structural Journal* 100.1 (2003), pp. 96–104.

[47] E. Sayed-Ahmed. "A new steel anchorage system for post-tensioning applications using carbon fibre reinforced plastic tendons". *Canadian Journal of Civil Engineering* 25.1 (1998), pp. 113–127.

[48] A. Al-Mayah, K. Soudki, and A. Plumtree. "Effect of Sleeve Material on Interfacial Contact Behavior of CFRP-Metal Couples". *Journal of Materials in Civil Engineering* 18.6 (Dec. 2006), pp. 825–830.

[49] A. Al-Mayah, K. Soudki, and A. Plumtree. "Effect of rod profile and strength on the contact behavior of CFRP–metal couples". *Composite Structures* 82.1 (Jan. 2008), pp. 19–27.

[50] J. Schön. "Coefficient of friction of composite delamination surfaces". *Wear* 237.1 (Jan. 2000), pp. 77–89.

[51] A. Al-Mayah. "Effect of sandblasting on interfacial contact behavior of carbon-fiber-reinforced polymer-metal couples". *Journal of Composites for Construction* 9.4 (2005), pp. 289–295.

[52] J. Rytter. "A Novel Compression Armour Concept for Unbonded Flexible Pipes". *Proceedings of the Annual Offshore Technology Conference* (2002), pp. 573–577.

[53] M. Bryant. "Nonmetallic unbonded flexible pipes for deep water". *Society of Petroleum Engineers - 2nd International Oil Conference and Exhibition in Mexico 2007* (2007), pp. 104–108.

[54] A. Al-Mayah, K. Soudki, and A. Plumtree. "Novel Anchor System for CFRP Rod: Finite-Element and Mathematical Models". *Journal of Composites for Construction* 11.5 (Oct. 2007), pp. 469–476.

[55] G. G. Portnov, V. L. Kulakov, and A. K. Arnautov. "Grips for the transmission of tensile loads to a FRP strip". *Mechanics of Composite Materials* 49.5 (Nov. 2013), pp. 457–474.

[56] B. Persson. *Physics of sliding friction : Physical principles and applications*. Springer, 1998.

[57]   T. Ruby, T. J. Herslund, and I. M. Sivebæk. "New Tribotester For Polymeric Materials". *Proceedings of the 12th Nordic Symposium on Tribology* (2006).

[58]   M. Kumosa, Y. Han, and L. Kumosa. "Analyses of composite insulators with crimped end-fittings: Part I—non linear finite element computations". *Composites Science and Technology* 62.9 (July 2002), pp. 1191–1207.

[59]   V. L. Kulakov, Y. M. Tarnopol'skii, A. K. Arnautov, and J. Rytter. "Stress-Strain State in the Zone of Load Transfer in a Composite Specimen under Uniaxial Tension". *Mechanics of Composite Materials* 40.2 (Mar. 2004), pp. 91–100.

[60]   ISO. "ISO 4287: Geometriske produktspecifikationer (GPS). Overfladebeskaffenhed. Profilmetode. Termer, definitioner og overfladebeskaffenhedsparametre" (1998).